Interactions in Anisotropic Nanomaterial Dispersions

by

Matthew Mohammad Noor

A dissertation submitted to the Graduate Faculty of
Auburn University
in partial fulfillment of the
requirements for the Degree of
Doctor of Philosophy

Auburn, Alabama
December 14, 2019

Keywords: single-walled carbon nanotubes, covalent functionalization, antibacterial materials, cholesteric liquid crystals, phase behavior, macroscopic assembly

Approved by

Virginia A. Davis, Chair, Professor of Chemical Engineering

Bryan Beckingham, Associate Professor of Chemical Engineering

Elizabeth Lipke, Mary and John H. Sanders Associate Professor of Chemical Engineering

Edward Davis, Assistant Professor of Mechanical Engineering

Mark R. Liles, Professor of Biological Sciences

Abstract

The overall objectives of this research were to advance understanding of interactions between carbon nanotubes and biological systems, and self-assembly of anisotropic nanomaterials. Specifically, this research presents results in two main areas: (1) the interactions of single-walled carbon nanotube (SWNT) dispersions with biomolecules and bacteriological systems, and (2) cholesteric liquid crystal flow and relaxation dynamics. In the first thrust of this research, the objective was to investigate the conflicting results in the literature regarding the antibacterial activity of carbon nanotubes. A comparison was made of the differences in antibacterial activity of covalent and non-covalent SWNT dispersed with an antibacterial enzyme, lysozyme (LSZ). The initial rates of antibacterial activity were shown to be affected by covalent versus noncovalent interaction and strong films were made from both dispersions. Additional antibacterial testing protocols developed in collaboration with Dr. Mark Liles group at Auburn University found that SWNT are not intrinsically antibacterial. However, their presence in a dispersion may hasten cell death in bacteria under significant cell wall stresses. This finding is significant because it clarifies that the conflicting results in the literature are due to stressful environments for bacterial cell walls, which skew results towards antibacterial activity. While SWNT were not found to be the root cause of this activity, they do exhibit a synergistic effect under the conditions of extreme cell wall stress.

In the second research thrust, the flow and relaxation dynamics of cholesteric liquid crystal dispersions were explored. Cellulose nanocrystal (CNC) dispersions were explored using rheological, rheo-small-angle neutron scattering (rheoSANS) and rheo-optical methods. The

results from rheoSANS experiments exhibited three-region behavior, which has been elusive for CNC dispersions, in viscosity versus shear rate curves but it was discovered that there was also three-region behavior in the order parameter. This behavior exhibited more defined transitions than that obtained from rheology measurements of biphasic CNC dispersions. Computational modeling, developed by Dr. Micah Green research group from Texas A&M University, and a series of rheological and rheo-optical experiments, performed at Auburn University, yielded a Landau-de Gennes formulation in a 3-D dynamic finite element simulation in which ellipsoid maps were created to predict alignment and helix orientation as a function of gap height and chiral strength during post-shear relaxation. This model was extended to include mass transfer and predict the orientation of CNC during film drying. Prediction of film microstructure is especially useful for the fabrication of controlled optical property films. These models were developed alongside extensive experimentation to verify their validity and accuracy to physical systems. Together, these research thrusts highlighted the importance of collaborative research involving multiple research methods to gain an in-depth understanding of interactions in anisotropic nanomaterial dispersions.

Acknowledgements

Pursuing my Ph.D. has been quite a journey and an amazing experience at Auburn University. First, I thank the department of Chemical Engineering at Auburn University for all the amazing opportunities it has afforded me. Second, I would like to acknowledge all the help, guidance, and support given by my advisor, Dr. Virginia A. Davis without whom this journey would not have been possible. I thank Dr. Mark R. Liles, Dr. Edward W. Davis, Dr. Bryan S. Beckingham, and Dr. Elizabeth A. Lipke for their support as my dissertation committee members. I thank Dr. Kyle D. Schulze for his review of this dissertation and for serving as university reader. I am grateful to all my group members, past and present, for their support and making this journey enjoyable. My collaborators, Dr. Katie Weigandt, Dr. Micah Green, Dr. Martin Pospisil, and Alinne Lima R. S. Pereira for many long conversations and insights.

I would like to acknowledge my father Mr. Masud Noor, my mother Mrs. Cynthia Noor, my girlfriend Ms. Andrea Sokel, and all the great friends I have made here at Auburn University for their constant love, support, and encouragement to make this journey possible.

Table of Contents

Table of Figures

List of Tables

Chapter 1: Introduction

The overall objectives of this research were to advance understanding of self-assembly of nanomaterials and interactions between carbon nanotubes and biological systems. Specifically, this research explored the covalent functionalization of single-walled carbon nanotubes (SWNT) with lysozyme (LSZ), whether carbon nanotubes have intrinsic antimicrobial properties, and the self-assembly of aqueous dispersions of cellulose nanocrystals (CNC) as well as dispersions of SWNT with double-stranded DNA. SWNT are omniphobic hollow nanocylinders made of single layers of rolled graphene sheets. One of the major obstacles to SWNT applications is the dispersion of individual and small bundles of SWNT, but noncovalent or covalent surface chemistry modification can be used to achieve this at low concentration. Cellulose nanocrystals are the crystalline regions of the naturally abundant polymer, cellulose. Cellulose is found in trees and plants as well as some species of algae, bacteria and tunicates. The sulfuric acid hydrolysis process used to extract CNC from the plant and wood biomass leaves the surface of the CNC with sulfate half-ester groups that repel other CNC resulting in stable aqueous dispersions that can form liquid crystalline phases.

Initial research focused on comparing the dispersion stability and activity of covalent SWNT-LSZ functionalization with previous research on noncovalently functionalized SWNT-LSZ dispersions and films. Lysozyme, an antibacterial enzyme, was attached with EDC (*N*-ethyl-*N*-(3-dimethylamino-propyl) carbodiimide hydrochloride) and NHS (*N*-hydroxysuccinimide) chemistry to oxidized SWNT. The activities of both covalent and noncovalent LSZ-SWNT activity were evaluated with a standard assay and compared to literature. The native LSZ activity retention of noncovalent LSZ-SWNT over the measurement period were consistent with literature values.

However, covalent LSZ-SWNT exhibited improved dispersion stability and longer duration of activity but had lower overall activity. Incorporation of these dispersions with poly(vinyl alcohol) into films showed increased strength of films while maintaining antibacterial activity, with only the noncovalent film showing improved hydrolytic stability.

More recent research in collaboration with the Dr. Mark Liles group in the Biological Sciences department at Auburn University focused on developing test methods to assess whether carbon nanotubes have intrinsic antimicrobial properties. There is a great need for the development of new antibacterial materials to combat the rise of antibiotic resistant pathogenic bacteria, particularly prevalent in healthcare environments. These types of infections cause an estimated 700,000 deaths worldwide per year according to the United Nations, predicted to rise to 10 million by 2050.[1] Differing results in the literature surrounding SWNT antibacterial activity have likely risen from the multidisciplinary nature of antibacterial testing methods and nanomaterial dispersion. As such, two assays were selected and developed which were simple and minimally influenced by the presence of nanomaterial dispersions. SWNT dispersing agents were also selected with a range of intrinsic antibacterial activities. These experiments found that antimicrobial activity is not an intrinsic property of SWNT, but instead a synergistic interaction between the nanotubes and sensitizing factors such as dispersant and experimental conditions.

Research on self-assembly and phase behavior of dsDNA/SWNT and CNC dispersions and the processing of these dispersions into films with controlled optical properties. Flow and relaxation dynamics of both CNC and dsDNA/SWNT were investigated with rheology combined with small-angle neutron scattering (rheoSANS). Optical microscopy was used to optically investigate the relaxation of CNC and these data was used to develop a model for the relaxation dynamics of cholesteric liquid crystal systems. The model was extended to include drying and surface anchoring effects on the microstructure for photonic films and compared to those made experimentally from CNC dispersions. The computational portion of the research was done by the Dr. Micah Green group at Texas A&M University.

Chapter 2 of this dissertation provides background on SWNT, LSZ, covalent attachment of LSZ to SWNT, liquid crystals, dsDNA dispersion of SWNT, and CNC. Chapter 3 outlines the experimental procedures used in this research. Chapter 4 contains the research effort on covalent and noncovalent LSZ-SWNT attachment and testing of films made with poly(vinyl alcohol). It also contains development of antibacterial testing assays used for testing against a range of SWNT dispersions. Chapter 5 investigates interactions, flow and relaxation dynamics of CNC dispersions probed by rheoSANS. This chapter also includes an investigation of phase behavior and aggregation issues arising from high concentrations of dsDNA/SWNT dispersions. Experiments on CNC dispersions used to guide modelling of relaxation and film drying behavior of cholesteric systems are also described in Chapter 5. Chapter 6 provides an overall summary of conclusions drawn from this research.

Chapter 2: Background

2.1 Single-Walled Carbon Nanotube Structure and Properties

Ever since the discovery of multi-walled carbon nanotubes (MWNT) by Iijima in 1991 and identification of single-walled carbon nanotubes (SWNT) two years later by Bethune et al, there has been tremendous interest in carbon nanotube research.[2-3] This research is motivated by carbon nanotubes outstanding properties. The theoretical Young's modulus of individual SWNT is 0.64 TPa,[4] and experimental evaluation of individual SWNT using atomic force microscopy resulted in a Young's modulus of 1.25 TPa.[5] Experimental values for SWNT bundles are in the range of 0.32 to 1.47 TPa.[6] An individual SWNT tensile strength is approximately 45 GPa.[7] Normalized for density, the Young's modulus of SWNT is 19 times higher than steel and 2.4 times higher than that of silicon carbide nanorods, and SWNT tensile strength is 56 times higher than steel and 1.7 times higher than silicon carbide nanorods.[8]

In addition to outstanding mechanical properties, SWNT possess outstanding electrical and thermal properties. SWNT can be either metallic or semiconducting. The thermal conductivity of SWNT has been reported to be 2700 W m^{-1} K^{1} in SWNT. Diamond, the current benchmark, has a thermal conductivity of 2500 W m^{-1} K^{-1}.[9] Thermal stability has been reported to be as high as 2800 ^{o}C in an inert atmosphere and 750 ^{o}C in air.[10]

All carbon nanotubes consist of coaxial sheets of rolled graphene. They are called single-walled (SWNT), double-walled (DWNT), few-walled (FWNT), or multi-walled (MWNT) depending on the number of layers. Most commercial nanotubes are on the order of one micron in length, diameters are approximately 1 nm for SWNT and tens of nanometers for MWNT. The major SWNT synthesis methods, electric arc discharge, laser ablation, gas-phase catalytic growth from carbon monoxide and chemical vapor deposition (CVD) each give SWNT with different diameters, lengths and chiralities.[11]

The chirality of SWNT is defined by the way the graphene sheet rolls upon itself to form a tube. It is described by the chiral indices (n, m) which define the direction of the circumferential chiral vector, $\overrightarrow{\mathrm{C_h}}$, corresponding to the vector $\overrightarrow{\mathrm{OA}}$ which is orthogonal to the translation vector $\vec{\mathrm{T}}$ in Figure 2.1. The chiral indices (n, m) are the respective number of steps along the hexagonal unit vectors $\overrightarrow{\mathrm{a_1}}$ and $\overrightarrow{\mathrm{a_2}}$ upon which the graphene sheet is rolled to form the SWNT, as in Figure 2.1. the relationship between $\overrightarrow{\mathrm{C_h}}$, (n, m) and $\overrightarrow{\mathrm{a_i}}$ is described by.

$$\overrightarrow{\mathrm{C_h}} = \mathrm{n}\overrightarrow{\mathrm{a_1}} + \mathrm{m}\overrightarrow{\mathrm{a_2}} \tag{2.1}$$

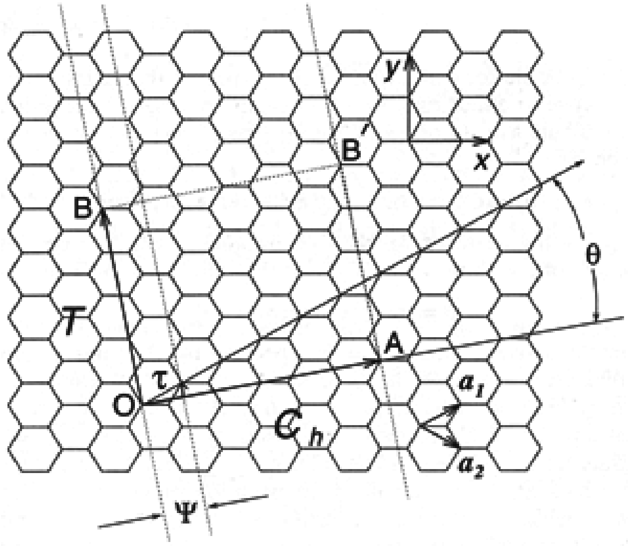

Figure 2.1: $\overrightarrow{C_h}$ is defined on the graphene lattice by unit vectors $\overrightarrow{a_1}$ and $\overrightarrow{a_2}$and the chiral angle θ, the angle from the zigzag axis. Reproduced from Dresselhaus et al.[12]

The magnitude of the unit vectors $\overrightarrow{a_i}$ are determined geometrically utilizing the carbon-carbon bond length, $L_{C\text{-}C}$, which is 0.142 nm for graphene.[13] Each hexagon can be geometrically split into six equilateral triangles, each unit vector will bisect two of these with a length of $\sqrt{3}\, L_{C-C}$, which corresponds to a value, called the lattice constant, of 0.246 nm. Therefore, a relation can be made between the chiral indices, unit vector s$\overrightarrow{a_i}$, the vector $\overrightarrow{C_h}$ and diameter, d, of the tube:

$$d = \frac{\sqrt{3}L_{C\text{-}C}(m^2+mn+n^2)^{\frac{1}{2}}}{\pi} = \frac{\left|\overrightarrow{C_h}\right|}{\pi} \qquad (2.2)$$

SWNT may be either semiconducting or metallic, depending on their chirality, as shown in

Figure 2.2. When n = m, the SWNT is metallic with a band gap of zero. However, when n-m is not equal to zero and divisible by three, it is semimetallic with a band gap on the order of meV. In all other cases, the nanotube is semiconducting with band gaps in the range of 0.5 to 1.0 eV.[11] Achiral SWNT are named for the shape of carbon structure around the circumference of the nanotube. Specifically, SWNT with chiral indices of $(0, m)$ or $(n, 0)$ are referred to as zigzag and SWNT with chiral indices of n = m are referred to as armchair, both are achiral categories. All other combinations of chiral indices are referred to as chiral. Examples of various SWNT chiralities can be found in Figure 2.3. Electronic transport in armchair SWNT is ballistic in the axial direction, because of the one-dimensional nature of the structure.[14] Superconduction has been observed for SWNT at extremely low temperatures.[15]

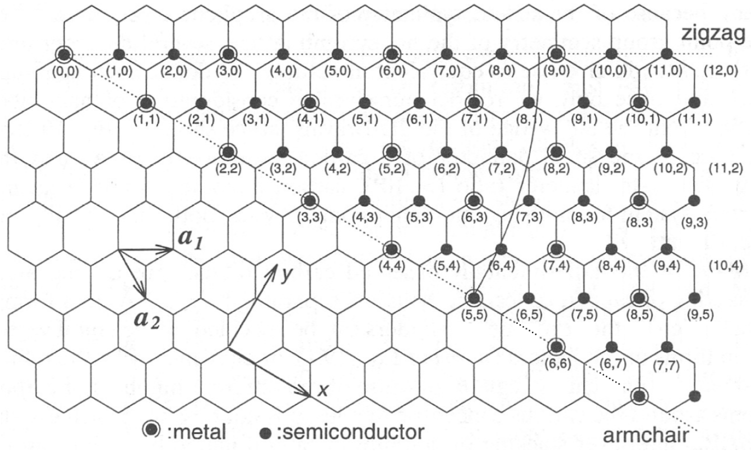

Figure 2.2: A map of chiral vectors corresponding to chiral indices (n, m) and electronic structure. Reproduced from Dresselhaus et al.[12]

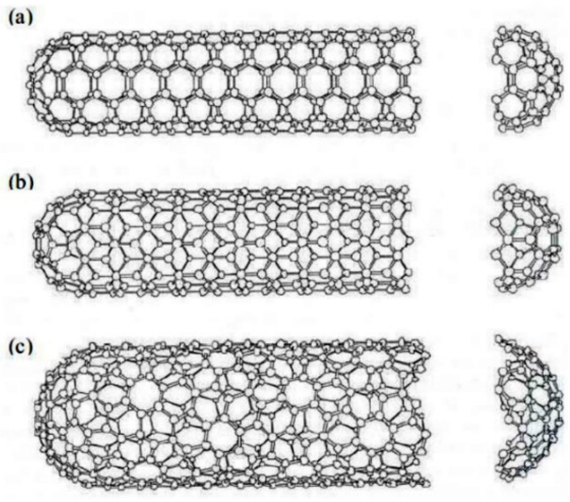

Figure 2.3: Types of SWNT: (a) armchair where the chiral indices are equal n=m and the chiral angle $\theta=30^{o}$, (b) zigzag with chiral indices of $(0, m)$ or $(n, 0)$ and chiral angle of $\theta=0^{o}$ and (c) chiral SWNT. Reproduced from Dresselhaus et al.[12]

The challenge associated with individualized SWNT dispersion is that SWNT have very strong van der Waals attraction to one another of 20-40 k_bT/nm[16-17] or on the order of 10^4 k_bT for a 1 μm SWNT. SWNT dispersion methods of often rely on organic solvents or surfactants and the use of sonication and centrifugation to achieve individual and small bundles of SWNT in dispersions. The only known thermodynamic solvent for SWNT is chlorosulfonic acid; other superacids can disperse SWNT up to 8 vol% with the aid of mechanical mixing.[18]

The optical properties of SWNT are largely due to their electronic structures and one-dimensional confinement of electronic and phonon states. This confinement results in what is known as the van Hove singularity in the SWNT density of states. van Hove singularities correspond to peaks in absorbance of individualized SWNT. Therefore ultraviolet-visible (UV-vis) spectroscopy is typically as evidence of individual SWNT dispersion state. In addition to absorption, Raman scattering can be used to obtain information about the vibrational states of the SWNT. Raman scattering refers to the inelastic scattering of light. In Raman spectroscopy on SWNT, when the energy of an incident photon is matched with a van Hove singularity in the electronic joint density of states, there is an enhancement of the Raman scattering, leading to information about the vibrational states of the SWNT, including tangential, and radial vibrations.[19] The distinguishing features that can be obtained from Raman spectroscopy are the radial breathing mode (RBM), the tangential vibration (G-band) and the disorder-induced vibration (D-band) peaks, shown in Figure 2.4. The tangential vibration is related to the sp^2 hybridized carbon, and the disorder-induced vibration is related to the sp^3 hybridized carbon in the SWNT structure. The sp^3 hybridized carbons arise from defects in the SWNT ends or walls. Therefore, Raman spectroscopy can be used in this research to determine the relative amounts of sp^3 and sp^2 hybridized carbons.

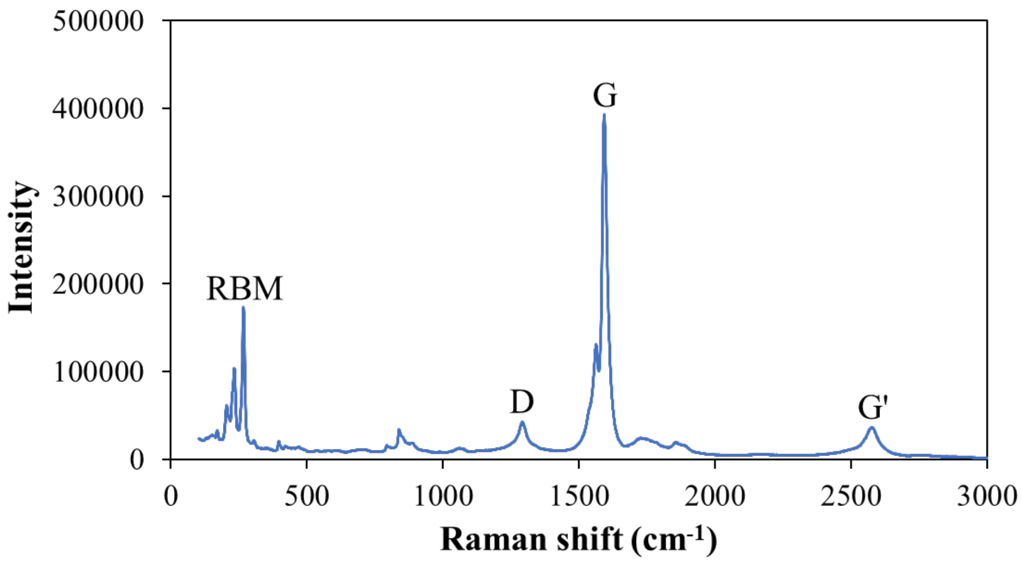

Figure 2.4: A typical Raman scattering pattern of NanoIntegris Super Purified SWNT with peak labels for: radial breathing mode (RBM), D, G and G′ peaks.

2.2 Lysozyme and Noncovalent Dispersion of Single-Walled Carbon Nanotubes

Lysozyme (LSZ) is an enzyme found in vertebrates, invertebrates, plants and microbes. In animals, it is found in saliva, mucus, tears and blood.[20] LSZ that exhibits antibacterial activity against Gram-positive bacteria such as *Staphylococcus aureus*. Applications of LSZ include coatings in cheese production[21] and serving as an antibacterial agent in commercial toothpaste[22] and mouthwash[23] products. LSZ functions by catalyzing the hydrolysis of 1,4-β-glycosidic linkages between N-acetylmuramic acid (NAM) and N-acetylglucosamine (NAG) which are components of peptidoglycan found in the cell wall of Gram-positive bacteria.[24-25] Gram-positive bacteria have a cell membrane with a peptidoglycan layer, while Gram-negative bacteria have an outer cell membrane and lipopolysaccharide layers in addition, shown in Figure 2.5.

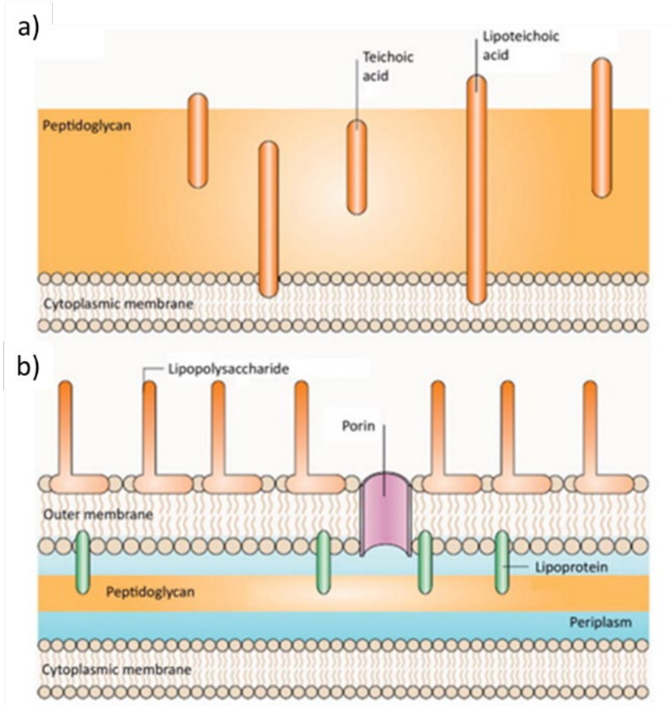

Figure 2.5: The bacterial cell wall structure of (a) gram-positive bacteria and (b) gram-negative bacteria.[26]

LSZ is polyampholytic meaning it contains many hydrophobic and hydrophilic region. In its native conformation, shown in Figure 2.6, the exposed LSZ surface is primarily hydrophilic. The surface hydrophilicity allows for stabilization and solubility in water. However, LSZ has the ability to retain its activity even in a partially-denatured state.[27] Disulfide bridges help to maintain the globular structure of the enzyme,[28] helping to preserve activity over a wide pH range, with an isoelectric point of 11, and temperature range, with denaturation at 76 ºC.[29]

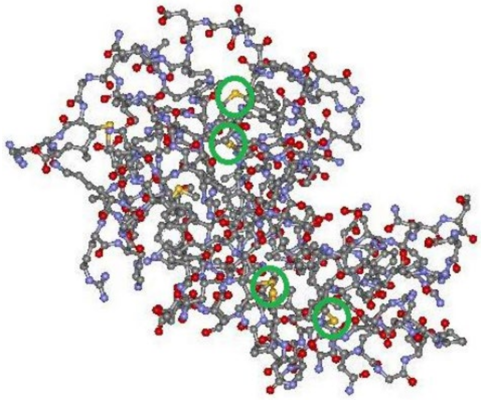

Figure 2.6: Ball-and-stick representation of LSZ structure highlighting the disulfide bridges at the core. All protein atoms are shown as balls, and bonds between atoms are shown as a stick. Carbon, nitrogen, oxygen and sulfur atoms are colored grey, blue, red and yellow, respectively. Adapted from Szymanska et al.[30]

LSZ disperses SWNT by hydrophobic π-π stacking interactions between SWNT and the tryptophans in the LSZ structure, as was proven by independent experimental and computational research.[31-32] Dispersion of SWNT in a tryptophan solution has been attempted previously in our group, however this did not yield dispersion. This may be due to tryptophan being very small relative to the SWNT structure. Non-covalent dispersion of SWNT-LSZ is achieved though partial-denaturation and fraying of SWNT bundles, which are achieved simultaneously through sonication, as in Figure 2.7.[33] The partially denatured LSZ is then allowed to interact directly with the SWNT wall through π-π stacking interactions. This results in relatively stable individual dispersion of SWNT by LSZ. Antibacterial activity retention has been shown for aqueous SWNT-LSZ dispersions,[31] layer by layer assembled thin films,[34] and composite films and fibers.[35-36]

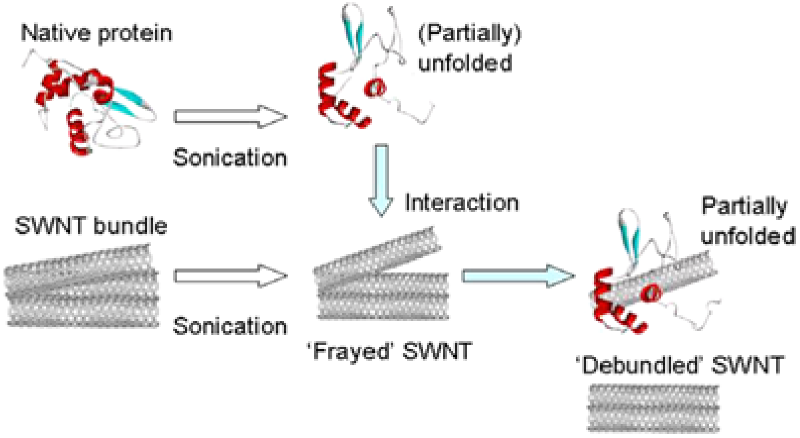

Figure 2.7: Noncovalent protein interaction with SWNT achieved through partial-denaturation of the protein and fraying of SWNT bundles to achieve individually dispersed noncovalently bound SWNT-protein. Adapted from Matsuura et al.[33]

2.3 Covalent Attachment of Lysozyme to Single-Walled Carbon Nanotubes

Covalent immobilization of enzymes onto oxidized carbon nanotubes is well documented, usually employing one of two common methods.[28, 37-40] Linker molecules are commonly used to covalently bind proteins and enzymes to carbonyl carbons on acid-oxidized SWNT, which contain both carboxyl and hydroxyl groups on the surface.[39-40] The first method uses APTES (3-aminopropyltriethoxy silane) and GA (glutaraldehyde) linking molecules.[39] The second method employs EDC [N-ethyl-N-(3-(dimethylamino)propyl) carbodiimide hydrochloride] and NHS [*N*-hydroxysuccinimide] chemistry for protein immobilization on acid-oxidized SWNT. This NHS molecule is a good leaving group, susceptible to reaction with an amide from an enzyme to a from a covalent bond between the SWNT and enzyme as shown in Figure 2.8.[40]

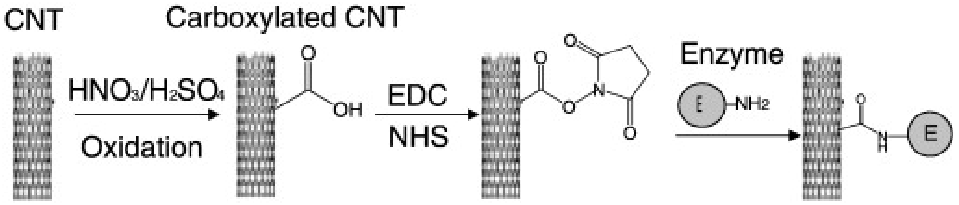

Figure 2.8: A schematic of EDC/NHS chemistry used to attach an enzyme to a SWNT surface. Adapted from Feng et al.[40]

2.4 Liquid Crystals

Liquid crystals (LCs) were discovered in 1888 by Austrian botanist Friedrich Reinitzer in collaboration with German physicist Otto Lehmann. Since then, there has been a wide variety of research done in the field.[41-42] LCs are highly ordered liquids that exhibit the order of a crystal and the fluidity of a liquid. Typically, LCs are categorized as thermotropic or lyotropic. The difference between these two are thermotropic LCs exhibit phase transitions with changes in temperature and lyotropic LCs exhibit phase transitions with changes in concentration. Common applications of LCs include liquid crystal displays (LCDs), optics, composites, biotechnology and biomedical devices.[43-44]

Thermotropic LCs are composed of semiflexible polymers, usually consisting of rigid aromatic ring cores and terminating in flexible, often aliphatic, chain structures. Thermotropic LCs typically undergo phase changes as a function of temperature and do not require the use of solvent molecules for LC phase transition. Thermotropic LCs are commonly used in displays due to their ability to be easily “switched,” but rather than with temperature changes, this is achieved in LCDs with localized electric field changes which reorient molecules at each pixel.[45] Lyotropic LCs can be formed in dispersions of rod-like (or “worm-like”) micelles (e.g. SDS, CTAB), or rigid rod-like anisotropic macromolecules and particles such as inorganic discs and rods (e.g. metal nanorods, discotic clay nanoparticles), biomolecules (e.g. Tobacco Mosaic Virus, DNA), or macromolecules (e.g. SWNT, CNC, p-poly (phenylene terephthalamide)).[43]

The classic Friedelian classes of LCs comprised of rod-like molecules are nematic, cholesteric, and smectic.[42] The rod-like molecules of nematic LCs are aligned in the direction of the vector called the director, **n**. Nematic LCs have long-range orientational order but only short-range positional order. In cholesteric LCs, also referred to as chiral nematic LCs, there is local nematic alignment in the direction of the director but follow a helical rotation around an axis normal to the director. Smectic LCs have both long range orientational and positional order. The two types of LCs most relevant to this research are nematic and cholesteric. An illustration comparing their microstructure is shown in Figure 2.9. Cholesteric helices can be further categorized by the orientation of the helical axis. Using two surfaces as reference points, these orientations are illustrated in Figure 2.10. The figure also conveniently illustrates the pitch length, P, which is the distance between a full rotation of rods along the helical axis.

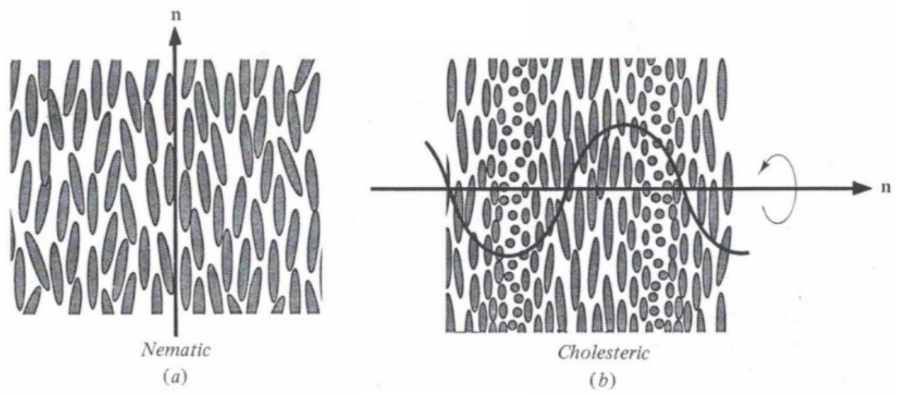

Figure 2.9: A comparison of nematic and cholesteric Friedelian classes of rod-like liquid crystalline alignment. Adapted from Donald and Windle.[42]

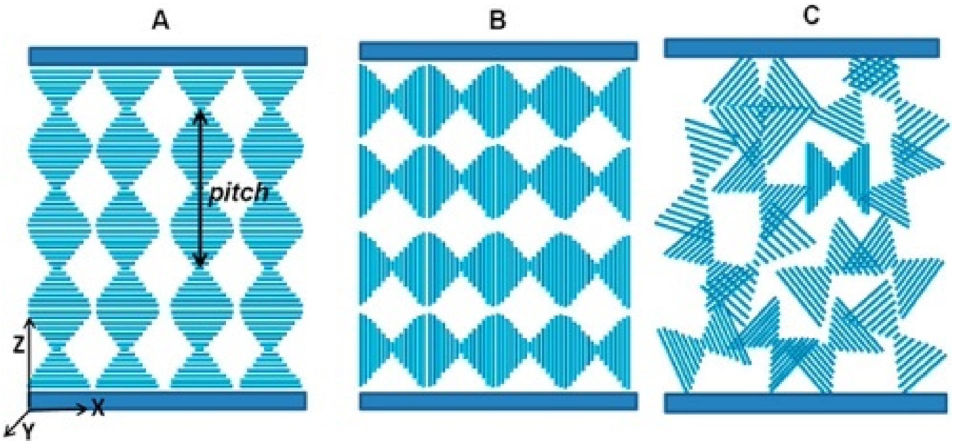

Figure 2.10: Illustrations of a) planar, b) homeotropic, and c) focal conic helical orientations. Reproduced from Saha and Davis.[46]

Changes in local rigid rod orientation during lyotropic phase transitions were described by Doi and Edwards, known as Doi-Edwards theory (Figure 2.11).[47-48] At low concentration, the dilute phase, rod-like molecules can freely translate and rotate. Increasing concentration into the semi-dilute phase limits rotation of the rods. In the isotropic concentrated phase, the rods have both limited translation and rotation and may only vibrate in a straw-like volume. At the critical isotropic to biphasic concentration, ϕ_I, the rods enter the biphasic regime. In the biphasic regime, both disordered, isotropic concentrated phases and ordered, anisotropic phases exist in equilibrium. Increasing concentration increases the relative amount of anisotropic phase present until the sample is fully anisotropic. This occur above ϕ_{LC}, the critical concentration for the onset of a single liquid crystalline phase. The liquid crystalline phase may be polydomain, meaning that the system is made up of many liquid crystalline domains, each with their own local director orientation. The formation of the anisotropic phase from the isotropic concentrated phase can be explained by the loss rotational entropy offset by the gain in translational entropy.

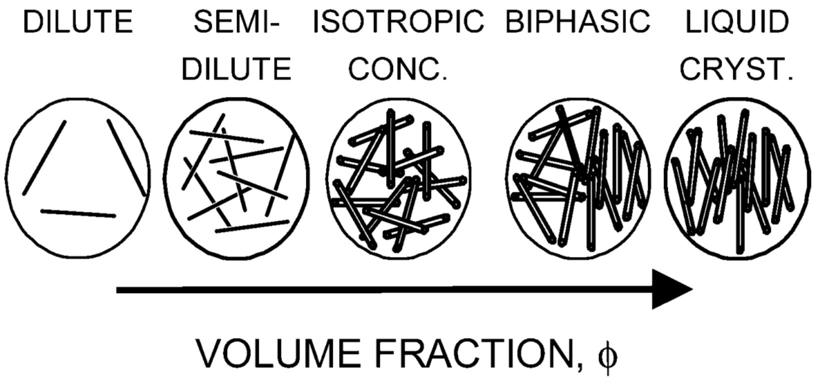

Figure 2.11: Doi-Edwards theory for the lyotropic phase behavior of Brownian rigid rods.[47, 49]

Onsager in 1949 developed a theory to describe the conditions for LC phase formation when transitioning from isotropic to anisotropic liquid crystalline phases.[50] This model assumes an ideal solution of long, rigid rods with length, L, and diameter, D, that are monodisperse. The final orientation at equilibrium is a direct result of the competition between orientational and translational entropy of the system. The limitation of Onsager theory is, because of truncation of the second virial coefficient, the solution is treated as ideal and thus only truly applicable for low concentration. However, this theory applies well for large aspect ratio rigid rod systems where L>>D. The critical concentrations from this theory are:

$$\phi_{\mathrm{I}}=3.34(\mathrm{D}/\mathrm{L}) \tag{2.3}$$

$$\phi_{LC}=4.49(\mathrm{D}/\mathrm{L}) \tag{2.4}$$

The order parameter is defined as the average orientation of all rods with respect to the direction of the director **n** given by:

$$S = \frac{3}{2}\langle cos^2\theta\rangle - \frac{1}{2} \qquad (2.5)$$

Where S is the order parameter, θ is the angle between the rod and the director and the brackets signify an average over all rods. For example, a completely isotropic system (i.e. random orientation) would have an order parameter of 0 and the order parameter for a perfectly aligned system would be 1. Because bulk LCs are often polydomain, with each LC region having its own unique local director, the order parameter can be low unless an external field (e.g. shear, electric, magnetic, etc.) is applied to align with a global orientation in the direction of the field influence. Order parameter in LC phases, will always be less than 1 due to slight imperfections arising from its LC nature (liquid crystalline and thus not a perfect crystal).

Flory, in 1956, developed what is known as the Flory lattice model.[51] The Flory lattice model confines the rod-like molecules to a lattice with constrained volume. This model predicts the nematic phase transition for rod-like particles and well known for modeling rod-like polymers such as PPTA in H_2SO_4 (DuPont Kevlar®), even at high concentrations. Critical concentrations from this theory are:

$$\phi_I = \frac{8}{L/D}\left(1 - \frac{2}{L/D}\right) \qquad (2.6)$$

$$\phi_{LC} = \frac{12}{L/D} \qquad (2.7)$$

Both Onsager and Flory theories laid the foundation for modern LC science. Adaptations of Onsager theory have been made to include attractive interactions and polydispersity, so that it will apply to a broader range of systems.[52-53] While Onsager theory has been less popular for semiflexible polymer LCs, it follows a hard-rod model which does not constrain the rods to a predetermined lattice and thus is more popular to describe high aspect ratio rigid inorganic lyotropic nanocylinder systems. Flory theory is popular for applications in lower aspect ratio semiflexible polymers.[54]

Optical birefringence is a fundamental property of LCs, and crystals in general, meaning that the way light propagates through the material depends on the orientation of the incident light relative to the material.[42] Essentially, the material exhibits two refractive indices, one parallel to the length of the chains, and one perpendicular. Polarized light is split along the slow, long axis, and fast, short axis, into extraordinary and ordinary rays, respectively. The extraordinary and ordinary rays have their associated refractive indices, n_e and n_o, respectively. These rays may then experience constructive or destructive interference due to phase differences arising from retardation of the light. The nature of this interference produces colors from the birefringence (Δn) which depend on ordering, retardation, and thickness of the sample, described by the Michel-Lévy chart in Figure 2.12. The effect of sample thickness is shown in Figure 2.13 for a shear aligned biphasic CNC dispersion.

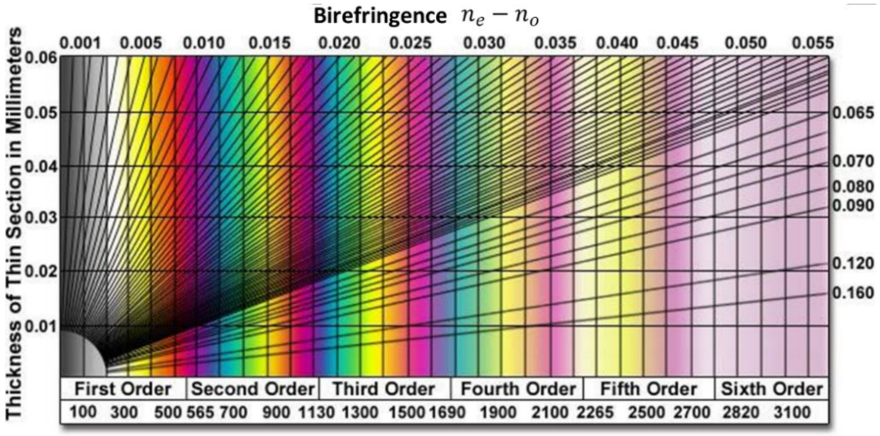

Figure 2.12: Michel-Lévy chart showing the relationship between film thickness, birefringence, and interference order.

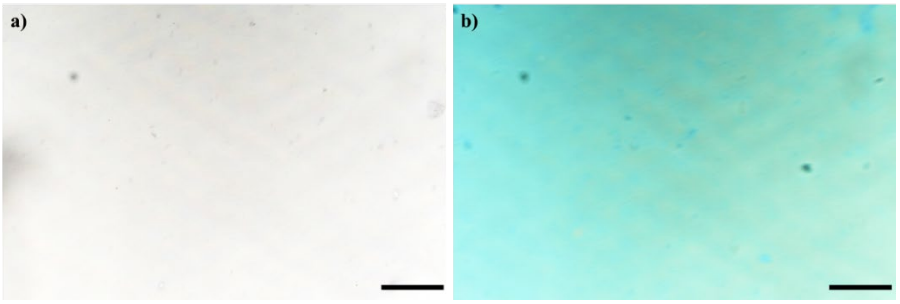

Figure 2.13: A comparison of sample thickness effects on birefringence color of a shear aligned 4.23 vol% CNC dispersion at a) 50 μm and b) 500 μm thickness. Scale bars are 100 μm.

The birefringence of the LC is described by $\Delta n = n_e - n_o$.[55] For the simple case of polarized monochromatic light through a perfectly aligned nematic sample of thickness, d, where the angle of the polarized light relative to the sample is $0° < \theta < 90°$ relative to the director, the phase difference, δ, experienced by the transmitted light is given by:[56]

$$\delta = \frac{2\pi d \Delta n \sin\theta}{\lambda} \tag{2.8}$$

By rotating the sample between crossed polarizers, anisotropic materials can be differentiated from isotropic materials. This method is employed in optical microscopy by rotating the sample stage relative to the crossed polarizers. The isotropic materials will remain extinct while the anisotropic materials will experience birefringence.

Measuring the rheological behavior of lyotropic LCs can give insight into microstructural properties and may be used to predict changes in microstructure due to processing conditions such as shear, temperature, and concentration. The distinct rheological features of lyotropic LCs include a maximum in the low-shear viscosity versus concentration curve, three-region viscosity vs shear rate, sign change in first normal stress difference vs shear rate, long oscillatory transients during startup of steady shear, and disobedience of the Cox-Merz rule.[57-59]

A local maximum in the low-shear viscosity vs concentration curve is usually followed by a local minimum, as in the system shown in Figure 2.14. Initial increases of low-shear viscosity are due to increasing limitation of the movement, translational and rotational. In the isotropic concentrated phase, the motion of the rods is limited and anisotropic phases begin to form. This change is somewhat retards the rate of viscosity increase until a local maximum is reached. At this point, the viscosity rapidly decreases as more anisotropic phases are formed. The decrease in viscosity with increasing anisotropic phases can be explained by the gain in translational entropy, allowing rods to slide past one another relatively easily. Then finally to a fully anisotropic phase which allows locally optimized translational motion of the rod-like molecules, evidenced by the local minimum in the liquid crystalline phase. Not all systems exhibit all of the signatures of a LC. For example, the aqueous sulfated CNC dispersions do not show the nonmonotonic viscosity versus concentration behavior, which has been attributed to electroviscous effects. [60-61]

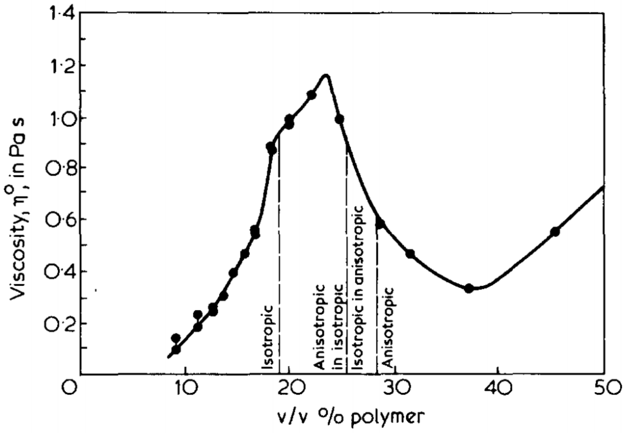

Figure 2.14: Low-shear viscosity versus shear rate of copolymer poly (50% n-hexyl and 50% n-propyl isocyanate) with MW=41000 in toluene at 25 °C.[62]

Three-region viscosity versus shear rate behavior has been observed for many lyotropic LCs. The behavior was identified by Onogi and Asada (Figure 2.15).[63] Essentially, Regions I and III show shear-thinning behavior and Region II shows a Newtonian plateau. This behavior has been confirmed for many LC systems.[59, 63-64] A few different mechanisms for shear thinning in Region I have been proposed for nematic LCs relating to plastic deformation of LC domains,[65] molecular orientation effects at the boundary versus the bulk,[65-66] and a combination of phase separation and shear history.[64, 67] Region II behavior is most well-understood for thermotropic and nematic rigid rod-like polymer LC systems. For thermotropic rod-like polymers, log rolling, tumbling, wagging or kayaking of the local director have been observed.[68-70] A narrow Newtonian plateau attributed to Region II has also been observed for nanocylinder systems including inorganic nanorods and SWNT.[49] For cholesteric LCs, Region II becomes more complex, as this is the region where chiral structure has been found to "unwind."[60, 71] Finally, there is general agreement that shear thinning in Region III consists mainly of director alignment with the flow direction.[64]

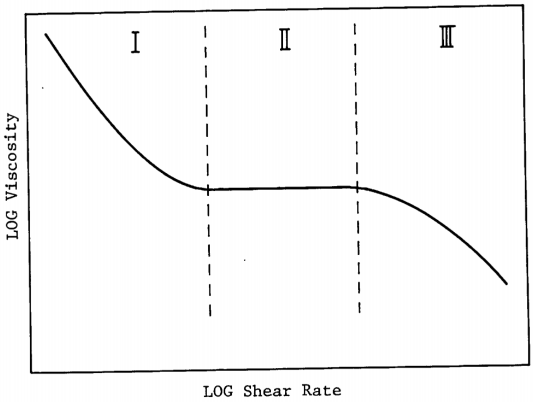

Figure 2.15: Three-region viscosity versus shear rate behavior for polymer LCs. Reproduced from Onogi and Asada.[63]

Long oscillatory transients during startup of steady shear are another signature of LC rheology. For isotropic suspensions and polymer solutions, steady state may be reached relatively quickly. However, for LCs, these transients usually require greater than 100 shear units ($t\dot{\gamma}$) before a steady state is achieved.[72] Typically, both shear stress and first normal stress difference, N1, exhibits a broad peak followed by dampened oscillations eventually arriving at a steady state.[57, 73-74] Davis et al. showed this for SWNT in 102% sulfuric acid, Figure 2.16.[49]

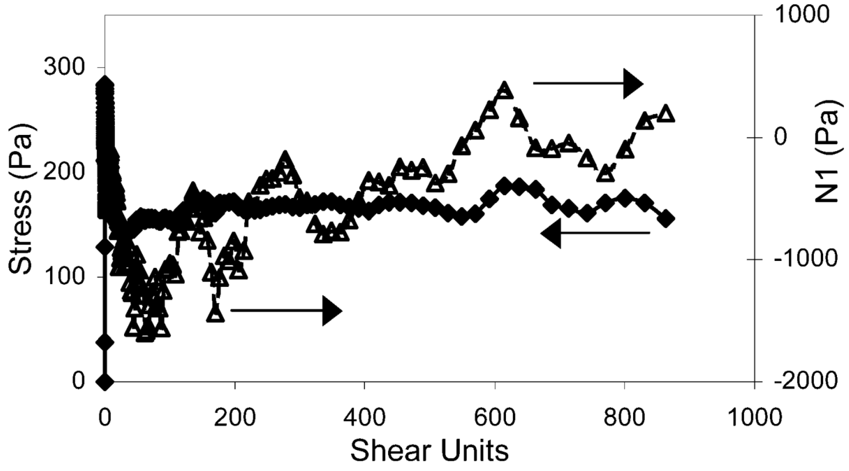

Figure 2.16: Oscillatory transients of shear stress and N1 for 7.6 vol% SWNT in 102% sulfuric acid. Reproduced from Davis et al.[49] Open triangles correspond to N1 and closed diamonds correspond to shear stress.

The Cox-Merz rule states that, the complex viscosity, a linear viscoelastic material property, is equivalent to steady shear viscosity at equal values of angular frequency and shear rate.[74-76] While this rule generally holds for ordinary polymers, LCs have a common characteristic of not obeying the empirical Cox-Merz rule due to the complex microstructural deformation dynamics of LCs.[73-74] For nanocylinder lyotropic LCs, an exemplary case is that of Davis et al., which consisted of SWNT in 102% sulfuric acid, Figure 2.17.[49]

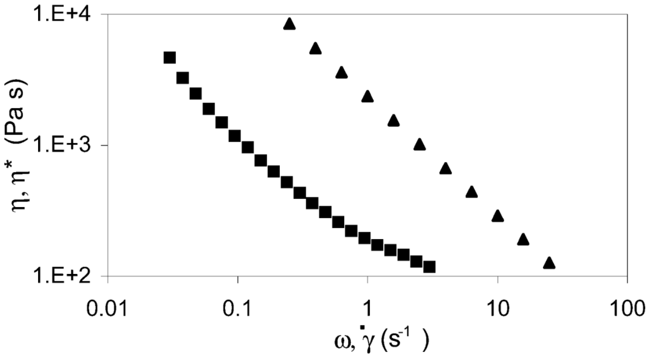

Figure 2.17: Cox-Merz rule not obeyed for 7.6 vol% SWNT in 102% sulfuric acid. Reproduced from Davis et al.[49]

2.5 Deoxyribonucleic Acid (DNA)

Deoxyribonucleic acid (DNA) is a genetic biomolecule made up of nucleic acids and a sugar-phosphate backbone. Double-stranded DNA (dsDNA), naturally occurring in cells, has two sugar-phosphate backbones with nucleic acid base pairs of A-T (Adenine-Thymine) and G-C (Guanine-Cytosine) that are held together due to the hydrogen bonding interactions between the complimentary base pairs (Figure 2.18). The helical structure arises from electrostatic repulsion of the phosphate groups in the backbone. Spacing between the backbones in the helix has two forms, a major and minor groove, the major being 50% larger than the minor.

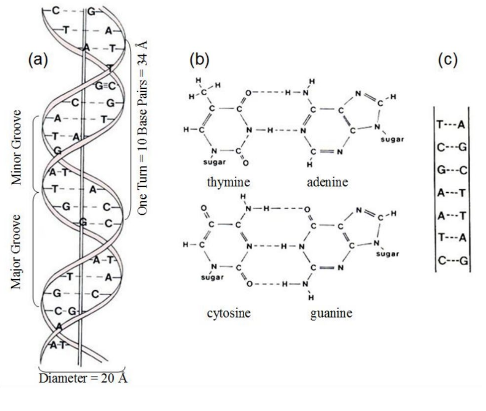

Figure 2.18: The Watson-Crick model of DNA structure and base pair interactions.[77]

dsDNA by itself forms is a lyotropic LC in water, forming a cholesteric LC at high concentration.[78] Due to the charged phosphate backbone of DNA, the self-assembly of DNA relies upon a reduction of the repulsive forces to allow the closely packed ordering required to achieve liquid crystallinity. The self-assembly of dsDNA into a cholesteric structure has been found to rely on salt concentration with higher salt concentration generally providing tighter ordering corresponding to a smaller pitch, Figure 2.19.[79]

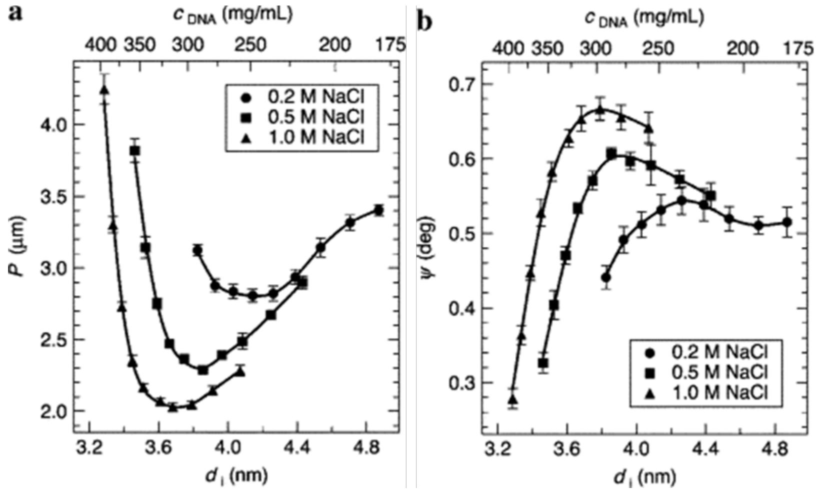

Figure 2.19: a) Pitch and b) twist angle, ψ, as a function of interaxial spacing, d_i, and concentration of DNA with various salt concentrations. Reproduced from Stanley et al.[79]

2.6 Cellulose Nanocrystals

Cellulose nanocrystals (CNC) are rigid, anisotropic nanomaterials extracted from the naturally abundant polymer cellulose, the main component making up plant cell walls.[80] Cellulose can also be made by a variety of bacteria, algae, fungi and tunicates.[80] Cellulose nanocrystals have also have excellent mechanical properties, with high elastic modulus measuring in the range of 110-200 GPa. Cellulose nanocrystals are three-dimensional nanoscale parallelepipeds with varying aspect ratio depending on both cellulose source and processing conditions. The natural abundance, renewability and strength of cellulose make CNC an attractive nanomaterial with many emerging applications.

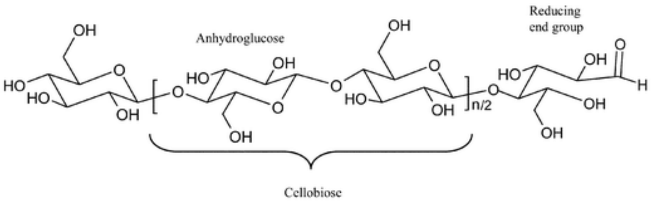

Figure 2.20: The structure of cellulose, showing the repeating anhydroglucose dimer cellobiose.[81]

Cellulose is comprised of repeating (1→4)-β-glucopyranose, or anhydro-D-glucose units. The dimer of anhydro-D-glucose bound by β (1→4) glycosidic linkages is referred to as cellobiose and is the repeating unit of cellulose.[80] The supramolecular structure of cellulose has been identified and categorized by four polymorphs: cellulose I, II, III, IV. Cellulose I is the naturally occurring polymorph, with the highest rigidity. Cellulose II or re-crystallized cellulose has been used to make cellophane and synthetic textile fibers such as Rayon.[82]

In 1951, Rånby found that the structure of cellulose contains both ordered, or crystalline, regions and disordered, or amorphous regions.[83] This occurs due to hydrogen bonding and van der Waals forces between cellulose chains, causing parallel alignment and stacking of cellulose molecules. Cellulose I is further separated into two characteristic crystalline structures: triclinic cellulose Iα, found in bacterial and algal cellulose, and monoclinic cellulose Iβ, found in most plants and tunicates. The distinguishing features between cellulose Iα and Iβ are the differences in intra- and inter-chain arrangement of cellulose along the $(110)_t$ and $(200)_m$ crystal planes due to hydrogen bonding, where the subscripts t and m refer to triclinic and monoclinic structures (Figure 2.21).[80]

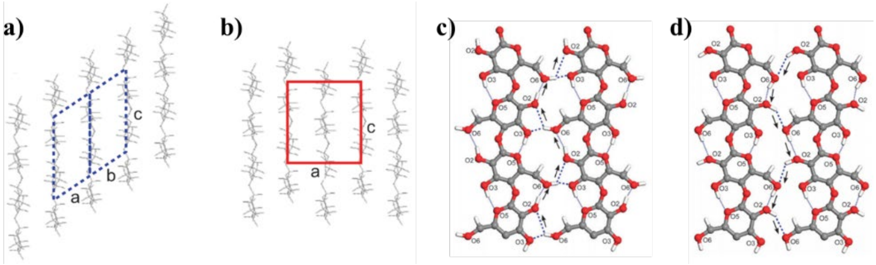

Figure 2.21: Comparison between chain arrangement of cellulose Iα (a) and Iβ (b) respectively and two inter-chain hydrogen bonding schemes, (c) and (d), proposed in the literature, all shown along the $(110)_t$ and $(200)_m$ planes.[80, 84]

The process of CNC preparation from woody or plant biomass begins with purification of cellulose source material to remove matrix materials such as hemicellulose and lignin and homogenization of the remaining wood and plant fibers. Subsequent processing is required to further break down these materials into microfibrillar and/or crystalline components. This is done by several methods including mechanical processing such as homogenization, grinding, ultrasonic processing. Essentially, these methods hope to achieve sufficiently high shear forces along the longitudinal axis of the cellulose fibrils to extract long strands of microfibrillated cellulose (MFC).[80]

Acid hydrolysis techniques are often used in sequence with mechanical processing to achieve a more uniform and stable dispersed crystalline products made from wood and plant fibers. Acid hydrolysis achieves this by hydrolysis of amorphous regions in the MFC, leaving behind the crystalline regions of the cellulose, CNC, as shown in Figure 2.22. Depending on the desired surface chemistry, sulfuric,[85] hydrochloric,[86] maleic acid,[87] or other acids are used in the literature for this purpose. Sulfuric acid hydrolysis is most commonly used due to the negative surface charge, stabilizing dispersions of these particles.[85] After reacting the acid is quenched with water, then separated and washed several times and redispersed by ultrasonic processing.[80]

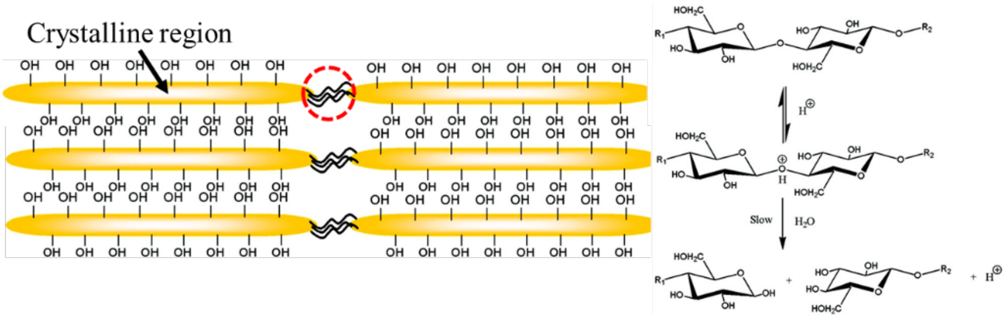

Figure 2.22: An illustration of a crystalline cellulose region with an amorphous region encircled in red and a simple acid hydrolysis reaction scheme.[85, 88]

The acid hydrolysis reaction scheme by itself leaves the CNC with no surface charge, as with hydrochloric or phosphoric acid hydrolysis.[80] This presents many challenges with dispersion due to the lack of surface charges which aid in repulsion of neighboring CNC and leads to aggregation of dispersions.[89-90] Sulfuric acid hydrolysis is often used to provide the CNC surface with sulfate esters by a nucleophilic substitution mechanism, shown in Figure 2.23. These sulfate esters are negatively charged, therefore providing some repulsive forces and leading to a much more stable aqueous dispersion. A major limitation of sulfonated CNC is accelerated thermal degradation due to introduction of sulfate ester groups which has consequences for applications in nanocomposites. Other common techniques for CNC surface modification are TEMPO-mediated oxidation,[91-92] acetyl esterification,[88, 93] hydrobromic acid hydrolysis,[85, 94] and silylation.[95-98]

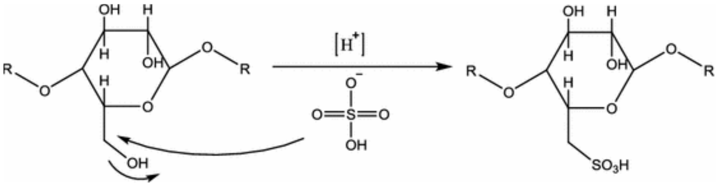

Figure 2.23: Nucleophilic substitution of a cellulose surface hydroxyl group.[99]

CNC have varying dimensions, depending on the cellulose source. Cotton and wood cellulose sources yield CNC with lengths in the range of 100 to 200 nm, where higher aspect ratios can be achieved with bacterial, or tunicate cellulose, which can have lengths in the ranges of 100-1000 nm and 100-3000 nm, respectively.[85] Processing, especially high energy processing, such as sonication can also have detrimental effects to the length of CNC.[80] Along with high aspect ratios, CNC have a high degree of rigidity, making them excellent LC mesogens. However, this requires dispersion at sufficiently high concentrations. Only sulfated CNC have been shown to form a LC in water. Others have shown LC formation of CNC with other surface chemistries in organic solvents.[93, 100-101]

The effective shape of CNC can be affected by the concentration of the counterion, commonly sodium (Na^+), which reduces the range of electrostatic double layer interactions, as shown in the transition from Figure 2.24a to Figure 2.24b. Araki et al. found that adding NaCl to bacterial CNC induced a transition from nematic to cholesteric ordering. The formation of a cholesteric LC, rather than a nematic, is due to the helical twisting structure of the CNC rod itself, as shown in Figure 2.24c. The characteristic cholesteric fingerprint texture of a biphasic CNC dispersion is shown in Figure 2.25.

Figure 2.24: An illustration of the twisted structure of CNC with surrounding effective ionic envelope a) before and b) after NaCl addition, and c) labeled schematic of the effective ionic envelope and the ordering behavior of a twisted rigid rod.[102-103]

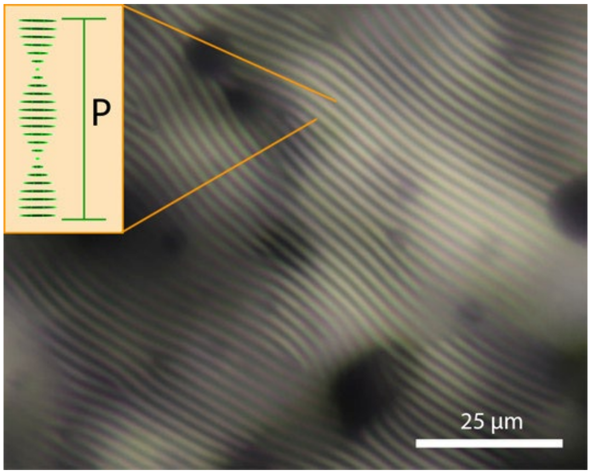

Figure 2.25: Cross polarized optical image of cholesteric fingerprint texture in 5.14 vol% a CNC dispersion with an illustration of the pitch length, P. Reproduced from Pospisil et al.[104]

Saha and Davis demonstrated the ability to induce different helix orientations in dried CNC films depending on the drying conditions and interactions of the CNC with surfaces.[46] This work showed that there were controllable differences in helical orientation allowing a planar cholesteric orientation to be maintained in the dried film, Figure 2.26. This required very slow drying, orbital shear, and provision of an anchoring surface. In this case, drying was slowed by increasing the humidity of the drying environment, and the anchoring surface was provided by a coverslip placed atop the dispersion. These films showed selective reflection of certain wavelengths of light, shown in Figure 2.27, which has many applications discussed later in this dissertation.

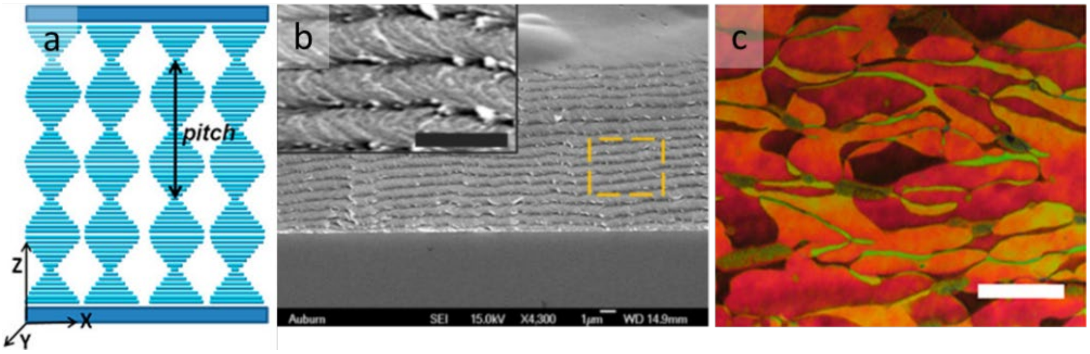

Figure 2.26: a) an illustration of planar helical orientation between the two surfaces, b) SEM image of cross section of a planar CNC film, and c) a polarized optical microscope image of red planar regions in the planar film with 50 μm scale bar. Adapted from Saha et al.[46]

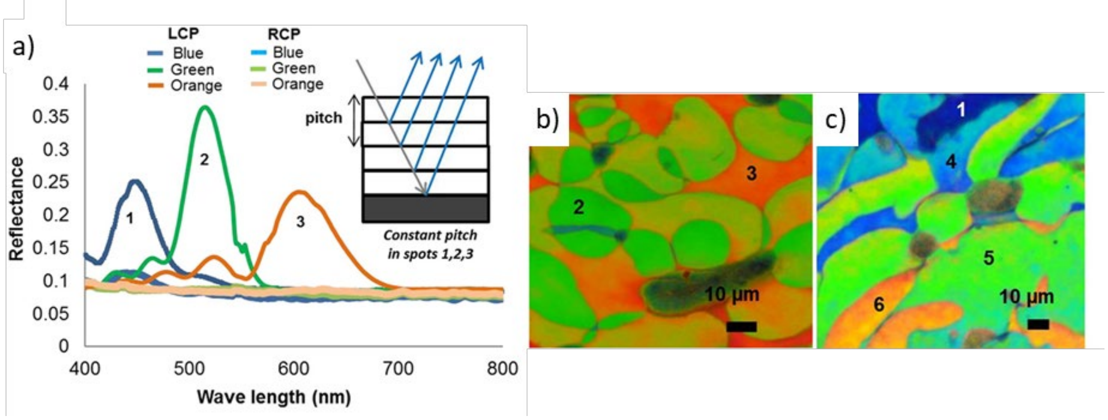

Figure 2.27: (a) Selective reflectance spectra using circularly polarized light showing single-peak reflectance, (b, c) Cross-polarized reflected micrographs showing selected planar domains. Adapted from Saha et al.[46]

Chapter 3: Experimental Details

3.1 Materials

SWNT was purchased from a range of manufacturers: CG200 (lots 14 and 17), CG300 (lots 32 and 35) were purchased from Chasm Inc., HiPCO (lot P1001) from Continental Carbon Nanotechnologies Inc., eDIPS EC1.5-P (lot 7202003) and EC1.5 (lot 6600903) were purchased from Meijo Nano Carbon Co. Ltd., and NanoIntegris purified (batch HP32-076) and Super-purity (batch HS32-067) SWNT were purchased from NanoIntegris Technologies, Inc.

CNC was purchased from the U.S. Forest Products Laboratory (FPL) and supplied by University of Maine Process Development Center (UM PDC) (Batches 2015-FPL-077 and 2018-FPL-CNC-126) as a ~12 wt% slurry in water. CNC rheoSANS measurements required CNC dispersed in D_2O. Therefore, freeze-dried CNC produced from woody biomass by sulfuric acid hydrolysis purchased from the US FPL and supplied by UM PDC (Batch 2012-FPL-CNC-051).

Lysozyme from hen egg white, double-stranded DNA sodium salt from salmon testes, and Pluronic F108 were purchased from Sigma-Aldrich. Sodium dodecyl sulfate was purchased from Fisher Scientific. Finally, BD Bacto tryptic soy broth (TSB) mixture was purchased form the manufacturer and prepared according to vendor instructions.

3.2 SWNT and CNC Dispersion Preparation

SWNT dispersions were tip sonicated according to the procedures described in Table 3.1 in an ice bath at a volume of 30 mL. Covalent SWNT-LSZ dispersions were prepared by the same sonication procedure as the noncovalent SWNT-LSZ, but at a concentration of 0.1 wt% of the covalent SWNT-LSZ. Also, it was found that the dispersion state of SWNT in TSB and LSZ dispersions decreased dramatically if the ice bath was not maintained with fresh ice in the ice bath. Therefore, the ice bath was replaced after every 10 minute of sonication time. The resulting dispersion mixtures were centrifuged for 3 hours at 17000 x g to remove SWNT aggregates, and the supernatants collected for experiments. For the dispersions which were tested against pathogenic bacteria, the dispersions were sonicated inside a biosafety cabinet to maintain sterility of the dispersions and prevent cross-contamination.

Table 3.1: Sonication procedures for all SWNT dispersions used in this work.

DISPERSANTS	DISPERSANT CONCENTRATION (WT %)	SWNT CONCENTRATION (WT %)	SONICATION PROCEDURE		
			Time (min)	**Amplitude (%)**	**Pulse (5 s on, 2 s off)**
SDS	1	0.2	60	60	no
Pluronic	2	0.2	60	60	no
TSB	N/A	0.1	30	60	yes
Lysozyme	0.5	0.1	30	60	yes
DNA	0.75	0.1	30	50	no

For CNC dispersions from the slurry, the slurry was diluted with DI water to the desired concentration, vortex mixed and allowed to slowly mix on a bottle roller overnight. The resulting dispersions were allowed to rest for at least 30 minutes before use. For SANS dispersions, Freeze-dried CNC were dispersed in D_2O. Deuterium oxide (D_2O) (99.8 atom %) was obtained from Acros Organics. A vortex mixer was used to mix approximately 12 g of CNC and 88 g of D_2O. The mixture was then placed in an ice bath and sonicated using a Sonics VC750 ultrasonic processor at 60% amplitude for a total of 35 minutes in 5 cycles of 7 minutes on and 2 minutes off. This produced a 12 wt% CNC dispersion in D_2O.

3.3 LSZ-SWNT Covalent attachment

Covalent attachment of lysozyme onto SWNT was carried on acid oxidized SWNT by carbodiimide activation of the carboxylic group in presence of EDC (*N*-ethyl-*N*-(3-dimethylamino-propyl) carbodiimide hydrochloride) and NHS (*N*-hydroxysuccinimide), both purchased from Sigma-Aldrich, following the procedure described by Asuri et al.[28] 50 mg SWNT were oxidized in 60 mL 3:1 sulfuric to nitric acid mixture for 6 hours, then quenched with 250 mL DI water and stirred overnight. The mixture was then further quenched with 600 mL of DI water, filtered and washed until neutral pH, then freeze-dried leaving a black powder of oxidized SWNT (SWNT-ox). At this point, the SWNT-ox was added to 400 mM NHS in 50 mM MES buffer and tip sonicated for 30 minutes. EDC was then added and the mixture was stirred for 30 minutes at 200 rpm, initiating the coupling of NHS to -COOH groups on the SWNT-ox. The mixture was then filtered and washed 3 times with MES buffer before adding 1 wt% LSZ in 10mM phosphate buffer and tip sonicated for 1 minute. The mixture was then placed on an orbital shaker at 200 rpm and allowed to react overnight. The mixture was then filtered, washed three times with water and once with 1% (v/v) Tween-20 solution to remove any nonspecifically bound LSZ and freeze dried to obtain the final product.

3.4 Spectroscopy

UV-Vis spectroscopy was performed with a Thermo Scientific NanoDrop 2000c UV-Vis spectrometer. This was principally done to obtain information about the concentration of SWNT dispersions using the Beer-Lambert Law $A = \varepsilon\, l\, c$ where ε is the extinction coefficient, A is the absorbance at a specified wavelength, l is the path length, and c is the concentration of the dispersion. The specified wavelength was kept consistent at 660 nm across all sample because this was the location of a strong van Hove singularity peak. The extinction coefficient was obtained by taking the slope of absorbance at 660 nm of dispersions serially diluted with DI water plotted against SWNT concentration.

Raman spectroscopy was performed as a basic characterization technique for the SWNT used in this work. Raman spectra were obtained using both 514 nm and 785 nm lasers on a Renishaw inVia Raman microscope equipped with a Leica 50X (0.75 NA) objective. The spectra were obtained from an accumulation of 10 runs with exposure time of 10 s for each run.

Circular dichroism spectroscopy was performed with JASCO J-810 Spectropolarimeter was used for circular dichroism (CD) measurements. Scans were taken at room temperature with a working spectral window of 180 to 320 nm with a scan rate of 10 nm/min and a resolution of 0.1 nm in a 1mm path length cuvette.

Fourier-Transform Infrared Spectroscopy (FTIR) was performed with Thermo Scientific Nicolet iS10 FTIR instrument using attenuated total reflectance (ATR) with a germanium crystal measuring 64 scans from 500 to 4000 cm^{-1}. Samples were used in their dried or powdered states.

3.5 Microscopy

Optical microscopy was performed with a Nikon (Melville, NY) Eclipse 80i microscope equipped with a Nikon DS-Ri2 camera to capture all of the cross-polarized optical micrographs using Plan Fluor LU 10×/0.30 and Plan Fluor LU 20×/0.45 objectives as well as a Plan Apo VC 60x/1.4 NA oil immersion objective. For Rheo-optical experiments, the microscope stage was replaced with a Linkam CSS450 optical shear cell and used with a L Plan SLWD 20x/0.35NA objective. The Linkam Linksys software was used to set the gap and rotation speed. Time-lapse images were taken over the following hour immediately following shear cessation.

Atomic force microscopy was performed with a Pacific Nanotechnologies Nano-R SPM. The scan rate was 0.2 lines/s and the resolution was set to 1024. SWNT and CNC AFM samples were prepared by diluting with DI water to SWNT or CNC concentration of 50 ppm or 0.005 wt% and adding 20 μL to the surface, allowing to rest for five minutes then drying with compressed air. Two substrates were used for AFM: freshly cleaved mica and plasma-cleaned silicon wafers with a 300 nm wet thermal oxide layer. For CNC samples, the mica surface was treated with 20 μL polycationic 0.01 vol% poly-L-lysine for 3 minutes before adding sample, as done by Honorato-Rio et al., to enhance CNC adhesion to the surface.[105] Samples were placed under vacuum for at least 1 hour before performing AFM.

3.6 Thermogravimetric Analysis

Thermogravimetric analysis (TGA) was done with TA Instruments Q50 and Q5000IR instruments and was used to obtain the thermal stability, relative amounts of components and concentration of some dispersions. Determining thermal stability was performed in both air and argon atmospheres. The standard TGA profile began with a 10 °C/min ramp from ambient to 120 °C followed by an isothermal hold for 20 minutes to drive off moisture from the sample. The temperature was then ramped at 10 °C/min to 800 °C and held isothermal for 45 minutes. For concentration determination of CNC, an argon atmosphere was used and temperature was ramped at 10 °C/min to 120 °C and held for one hour or until mass was no longer changing.

Chapter 4: Antibacterial Properties of SWNT

There is a need for research into novel antibacterial materials for a wide variety of applications in the biomedical, water and air purification, food production, cosmetics and clothing industries, as well as use in numerous household products.[106] Recently, there have been concerns about infections and spread of antibiotic resistant bacteria, which have been becoming increasingly more prevalent in healthcare settings. On September 21, 2016, the United Nations declared antibiotic resistance "the greatest and most urgent global risk."[107] According to the CDC in 2014, there are 2 million infections and 23,000 deaths per year due to antibiotic-resistant bacterial infections.[95] Antibiotic resistance motivates research and development of novel antibacterial materials in order to combat the spread of these drug-resistant pathogens.

There is significant conflict and controversy in the literature over whether SWNT are antibacterial and the method of action of potential antibacterial activity. There are conflicting results in experiments involving cytotoxic effects due to factors such as purity and functionalization,[108-110] cell culture media,[111] and cell type.[112] The method of action of SWNT cytotoxicity is also very difficult to determine, as there are many factors that can be affected by a material at the nanoscale. Hypothesized methods of action in the literature include metabolic disruption or inhibition,[113] oxidative stresses,[113-115] and physical piercing damage to the cell membrane.[114, 116-117] It is important to understand this particular property of SWNT to provide a foundation for possible future applications of this material.

4.1 Comparison of Covalent and Noncovalent LSZ-SWNT Attachment

Research on the combination of carbon nanomaterials with proteins and enzymes has been driven by both the desire for aqueous dispersion and the desire to combine the electrical, mechanical, thermal or optical properties of carbon nanomaterials with those inherent in biological materials.[28, 32, 118-122] LSZ-carbon nanomaterial adducts have attracted particular interest due to the enzyme abundance, inherent antimicrobial activity, and stability. In addition, both experimental and computational investigations have shown that lysozyme tryptophan residue has favorable interactions with sp^2 hybridized carbon nanomaterials which enables dispersion of single-walled carbon nanotubes (SWNT),[31-32, 34] multi-walled carbon nanotubes (MWNT),[123] graphene oxide,[124] and fullerenes such as C_{60}[125-126] at higher concentrations than can be achieved with many other biological or synthetic dispersion aids. As a result, LSZ-carbon nanotube dispersions have been used to produce antimicrobial carbon nanotube films and fibers,[35-36] and sort nanotubes by size.[127]

While much of the research has focused on noncovalent interactions between carbon nanomaterials and LSZ, this approach does have some disadvantages. Most notably for SWNT, efforts to increase the concentration of LSZ-SWNT dispersions resulted in depletion attraction and nanotube aggregation above a 2.1:1 LSZ:SWNT volume ratio.[35] Therefore, achieving the higher concentrations more suitable for film or fiber production requires a different approach. Horn et al. used a combination of an additional surfactant and polymer to produce antimicrobial fibers with toughness greater than spider silk.[35] Similarly, Nyankima et al. used a polymer solution to produce transparent antimicrobial films.[36] In contrast, Merli et al. demonstrated covalent attachment of LSZ to multiwalled carbon nanotubes (MWNT) using standard EDC-NHS chemistry and that this approach resulted in greater antimicrobial activity than native lysozyme.[38]

Differences between covalent and noncovalently functionalized LSZ-SWNT were evaluated in terms of relative dispersion concentrations, supernatant antibacterial activity, as well as the antimicrobial activity and mechanical properties of LSZ-SWNT-PVA films. Covalent attachment was performed using EDC-NHS chemistry following the method developed by Merli et al. for LSZ functionalization of MWNT.[38] The SWNT and LSZ concentrations for noncovalent dispersions were chosen for consistency with previous work. The concentration of the covalent functionalized LSZ-SWNT was chosen to be consistent with SWNT concentration in noncovalent LSZ-SWNT dispersions (e.g. 1mg/mL covalent LSZ-SWNT).

Since covalent functionalization results in conversion sp^2 to sp^3 hybridized carbon, the ratio of the maximum peak intensity of the Raman spectroscopy D band located at 1356 cm^{-1} which is due to tangential stretching of sp^3 hybridized carbon to the G band located at 1592 cm^{-1} was used to verify covalent functionalization.[19] Figure 4.1a shows the Raman spectra for the pristine SWNT, noncovalently functionalized LSZ-SWNT and covalently functionalized LSZ-SWNT using a 514 nm laser. The D:G ratio for the pristine and noncovalently functionalized SWNT were within experimental error with average values of 0.11 and 0.08 respectively. For the covalent LSZ-SWNT, the relative intensity of the D peak increased resulting in a ratio of 0.22 on the 514 nm laser. Increased in the covalent LSZ-SWNT samples D:G ratio is indicative of successful covalent functionalization. Raman data obtained with a 785 nm laser, Figure 4.1b, shows similar results with ratios of 0.10, 0.16, and 0.32 for SWNT, noncovalent and covalent functionalized LSZ-SWNT, respectively.

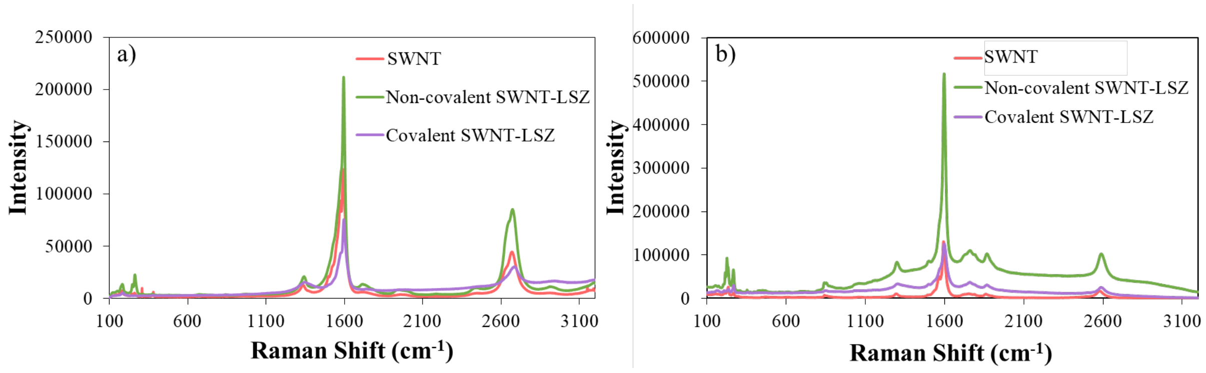

Figure 4.1: Spectroscopic characterization. Raman Spectra performed on LSZ-SWNT samples with a) 514 nm and b) 785 lasers.

FTIR was used to explore the effects of SWNT attachment on LSZ, shown in Figure 4.2. Comparing the position, relative intensity and shape of a protein amide I and amide II bands is one of the key methods for identifying protein-nanomaterial interactions and protein conformational changes.[31] The amide I band is primarily due to C=O stretching of the peptide while the amide II peak is primarily due to C-N stretching as well as N-H bending. Figure 4.2 shows FTIR spectra of the two LSZ-SWNT supernatants and LSZ prepared by an equivalent method without the addition of SWNT. For the pure LSZ dispersion, the amide I band which was symmetric centered at 1651 cm^{-1} and had approximately double the intensity of the symmetric amide II band centered at 1533 cm^{-1}. In the case of noncovalent SWNT functionalization, the amide I band was similar to that for pure LSZ, centered at 1650 cm^{-1}. This indicates that interaction with the SWNT had little effect on the backbone secondary structure.[128] However, the amide I band for the noncovalently functionalized LSZ-SWNT had nearly four times the intensity of the amide II band which was significantly downshifted was significantly to 1526 cm^{-1}. Furthermore, the increased intensity of the amide III bands (1200 – 1350 cm^{-1}) indicate significant changes to the secondary and tertiary structure.

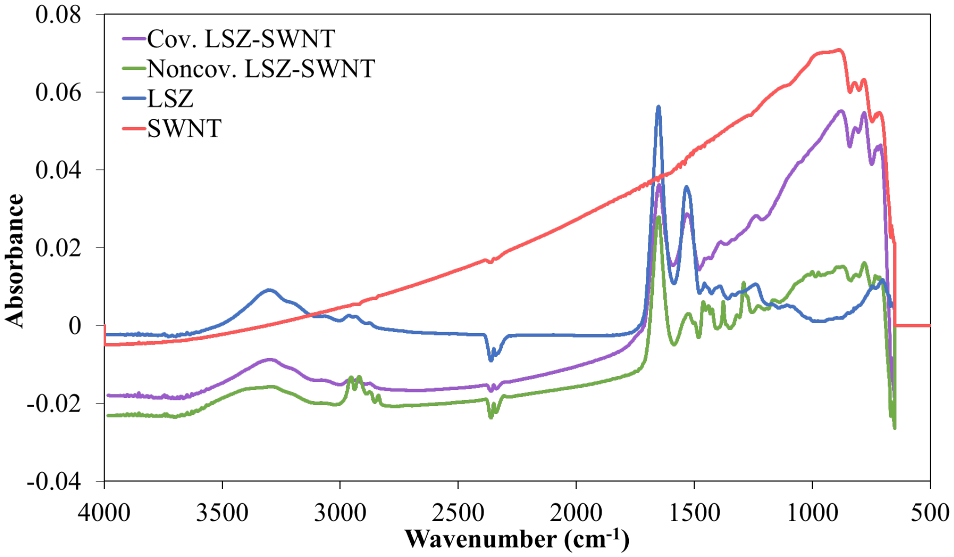

Figure 4.2: FTIR comparison of SWNT, LSZ, and LSZ-SWNT samples.

Sonication of LSZ-SWNT dispersions results in the simultaneous debundling of SWNT and partial unfolding of LSZ which exposes the tryptophan residue which then experiences π–π stacking interactions with the SWNT.[31-32, 118, 123] Cessation of sonication results in refolding of LSZ, but the presence of the SWNT inhibits restoration of the original confirmation. In contrast, covalent functionalization through EDC-NHS chemistry, resulted in similar amide I to amide II intensity ratio and amide III peaks as the pure LSZ. However, the covalent functionalization resulted in a greater downshift in the amide I band to 1648 cm^{-1} suggesting more changes to the LSZ backbone, but less shift in the amide II band which was centered at 1531 cm^{-1}.

CD spectroscopy is often used to make comparisons between the secondary structures of proteins to confirm that proteins are in their native conformations.[129] In this research, CD spectroscopy was used to compare the secondary protein structures of the native LSZ with the covalent and noncovalent LSZ-SWNT adducts. The spectra in Figure 4.3 show a significant decrease in α-helix structure in the covalent-LSZ-SWNT. The noncovalent LSZ-SWNT, on the other hand, has some loss of α-helix structure due to partial denaturation from sonication and SWNT interaction but largely maintains the native LSZ conformation. The loss of enzyme structure can have consequences when it comes to enzyme function and native activity retention.

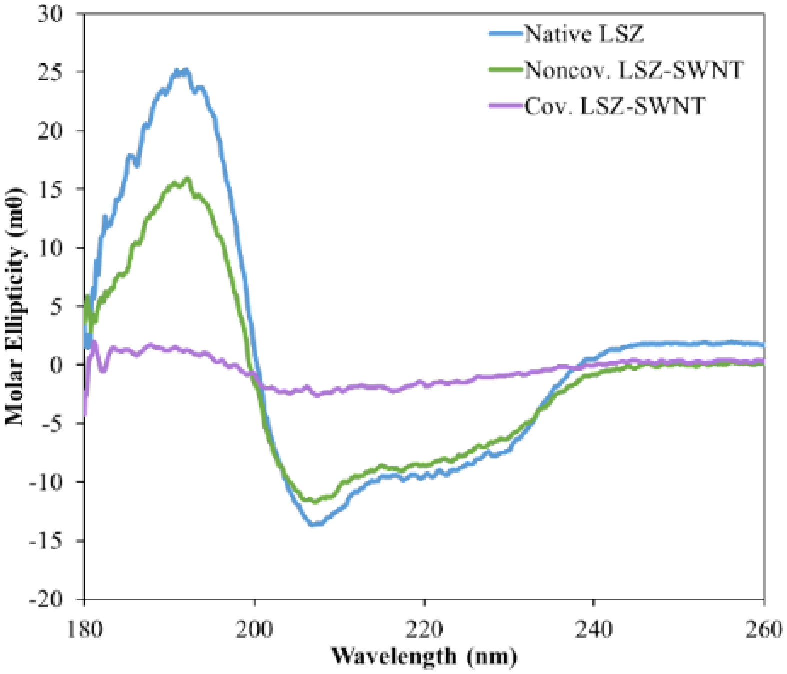

Figure 4.3: Comparison of CD spectra of native LSZ with the covalent and noncovalent LSZ-SWNT.

The concentrations in the supernatants and amount of bound LSZ was determined using a combination of UV-Vis spectroscopy and thermal gravimetric analysis (TGA), based on previously reported methods.[31, 35-36] Table 4.1 shows the amounts of LSZ and SWNT determined by TGA in addition to ratios of LSZ:SWNT for covalent and noncovalent dispersions. Interestingly, while the initial LSZ:SWNT ratio (by mass) was higher for the noncovalent dispersion, slightly fewer LSZ molecules were found to be bound per SWNT, than for the covalent functionalization. This suggests that the binding efficiency is not greatly affected by functionalization type.

Table 4.1: Relative amounts of LSZ and SWNT in mixtures and supernatants of noncovalently and covalently functionalized LSZ-SWNT.

	Non-Covalent LSZ-SWNT		Covalent LSZ-SWNT	
	Mixture	Supernatant	Mixture	Supernatant
SWNT (mg/mL)	1.0	0.69	0.21	0.14
LSZ (mg/mL)	5.0	3.84	0.79	0.25
LSZ_{Total}:SWNT	5.0	5.5	3.8	1.8
Bound LSZ (mg/mL)	0.89	0.97	0.79	0.25
Number bound LSZ /SWNT	30	57	100	60
C-atoms (SWNT) per bound LSZ	1250	655	281	469

In addition to determining the relative amounts of bound components, TGA also provided insight into the thermal stability resulting from the two functionalization methods. In an inert argon atmosphere, Figure 4.4a, the thermal stability of both covalent and noncovalent LSZ-SWNT are similar until 560 °C. After 560 °C, the difference in thermal stability is due to oxidation and subsequent covalent functionalization causing a loss in thermal stability of the SWNT. The TGA curves in the air atmosphere, Figure 4.4b, show higher thermal stability the covalent sample and lower thermal stability in the noncovalent sample compared to both the SWNT and LSZ curves. It can be inferred that covalent functionalization has some stabilization effect on the LSZ while the slight denaturation of the LSZ during sonication is most likely the cause of lowered thermal stability of the noncovalent LSZ-SWNT sample.

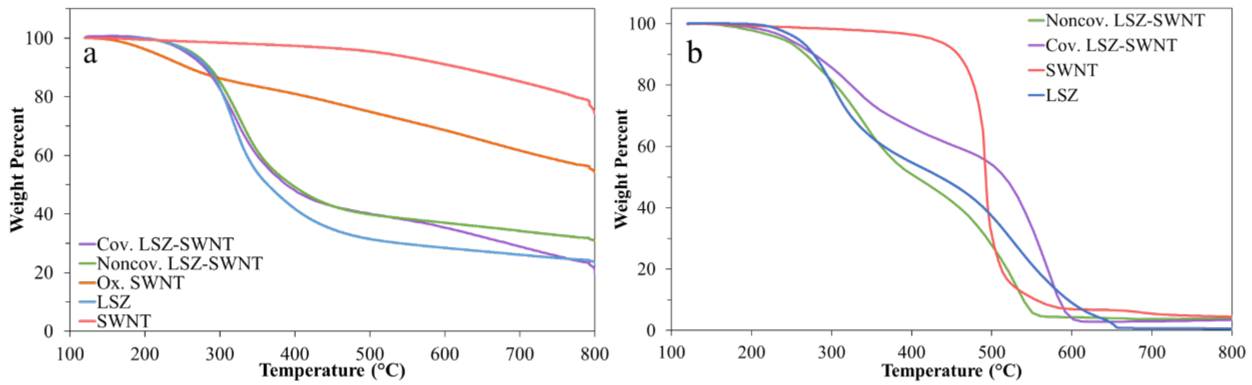

Figure 4.4: TGA of SWNT, LSZ, and LSZ-SWNT samples in a) argon and b) air atmospheres.

The assay used in this work was a simple turbidimetric assay which was recommended by the LSZ supplier, Sigma-Aldrich, which has its own developed protocol[130] based upon the method developed by Shugar[131] for measuring LSZ activity. This method has the advantages of being simple with no requirement of a sterile environment and maintaining with previous work.[31, 35-36, 132] The method is based on changes in turbidity resulting from the lysis of *Micrococcus lysodeikticus*, measured by absorbance at 450 nm and normalized by the initial absorbance, described by:

$$\text{Activity} = \frac{(\Delta \boldsymbol{Abs_{450}/t})_{\boldsymbol{test}} - (\Delta \boldsymbol{Abs_{450}/t})_{\boldsymbol{blank}}}{\mathbf{0.001}(\boldsymbol{m})_{\boldsymbol{LSZ}}} \tag{4.1}$$

where ΔAbs_{450} is the change in the 450 nm absorbance intensity, t is the test duration, m_{LSZ} is the mass of LSZ and test or blank indicates the presence of the LSZ material or blank buffer solution. The protocol for the turbidimetric assay was as follows: A 0.015 % w/v *M. lysodeikticus* ATCC No. 4698 (lyophilized, Sigma-Aldrich) bacterial suspension was prepared in a 66 mM potassium phosphate monobasic buffer (pH 6.24 adjusted by 1M potassium hydroxide). A 10 mm path length quartz cuvette with 2.5 mL of the bacterial and 0.1 mL of sample dispersion or diluted sample was subjected to kinetic scan for 25 minutes at 450 nm. Studies on the variance of LSZ absorbance over three batches of LSZ showed an average standard deviation of 0.02, shown in Figure 4.5.

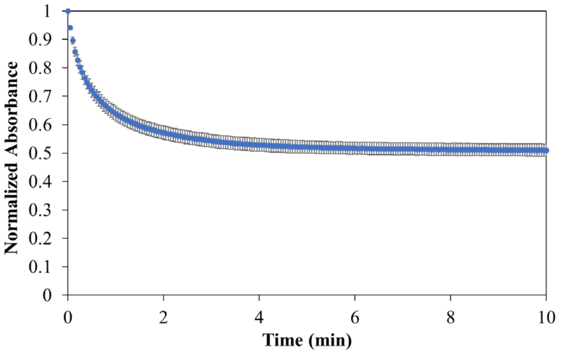

Figure 4.5: Turbidimetric assay of LSZ plotted with standard deviation.

As shown in Figure 4.6, the native LSZ showed an immediate decrease in absorbance that followed Michaelis-Menten kinetics and then plateaued after approximately 5 minutes. Similar behavior was exhibited by the noncovalent LSZ-SWNT, but the initial activity (decrease in absorbance) was more significant, and after five minutes the data became scattered due to the formation of SWNT flocs which intermittently obscured the optical path. In contrast, covalent SWNT-LSZ shows a continuous, nearly linear decrease in absorbance throughout the measurement time. The 80% maintained activity of noncovalent LSZ-SWNT is in agreement with the results of Horn et al.[31] The reported activity is the average of four runs and the standard deviation was about 300 active units/mg LSZ.

The linear cell death slopes, or initial rates of lysis activity, of the SWNT-LSZ and LSZ systems, shown in Figure 4.6, were obtained by finding the natural logarithm of the first 0.5 min in the initial linear region of the native LSZ and SWNT-LSZ dispersions and obtaining the corresponding slopes, as done by Nyankima et al.[36] The non-covalent SWNT-LSZ had a much higher rate of activity at 0.93 min^{-1} compared to the native LSZ rate of 0.57 min^{-1}. Covalently bound SWNT-LSZ had a much lower rate of 0.014 min^{-1} but retained its activity over a much longer period. This combined with the absence of flocculation over the assay period suggests stabilization of the SWNT dispersion state by covalent LSZ functionalization. However, in contrast to investigations by Merli et al. of covalent LSZ functionalization of MWNT, the data do not indicate that the presence of the SWNT increased LSZ activity.[38] This could be because Merli et al. considered living, rather than lyophilized, cells with a longer-term colony-forming unit count method and not initial kinetics, differences in LSZ confirmation due to the different nanotube diameter, or differences in nanotube surface chemistry.

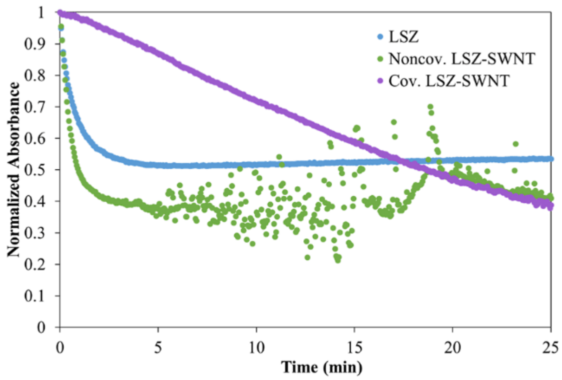

	LSZ	**Noncov. LSZ-SWNT**	**Covalent LSZ-SWNT**
Linear cell death slope	0.66	0.94	0.02
Specific activity (active units/mg LSZ)	1977	1642	1295
Native LSZ activity maintained (%)	100	83	66

Figure 4.6: Turbidimetric assay of dispersions as well as a table showing initial cell death slope, specific activity, and percentage of native LSZ activity maintained for each dispersion.

SWNT-LSZ-PVA films were prepared by adding a 5 wt% PVA solution to the dispersion to obtain 1.1 wt% PVA in each dispersion. 10 mL of SWNT-LSZ-PVA were placed in a 50 mm diameter glass dish and allowed to evaporate on an orbital shaker overnight to obtain a thin film. Assays were performed by the procedure stated above, adjusting the time to 30 min and placing a sample of film with 50 mm^2 surface area into the bacterial suspension in place of dispersion. Tensile testing was performed with a 3 mm x 15 mm film sample on an Instron model 5500 with a 100N load cell and with a crosshead speed of 1 mm/min.

Nyankima et al.[36] showed that transparent, mechanically robust antimicrobial cast films could be made from combining of LSZ-SWNT dispersions with a PVA solution. Their work demonstrated that casting films from supernatant dispersions resulted in greater transparency, antimicrobial activity and mechanical properties than casting films from the initial mixtures which contained bundles and aggregates. However, their work did not explore the effects of covalent functionalization. Figure 4.7 shows assays performed with SWNT-LSZ-PVA, as well as control LSZ-PVA and PVA films. The PVA-only film showed some slight activity, possibly due to some cellular aggregation from depletion attraction caused by the dissolution of PVA.[133] Both film and dispersion assays exhibited similar LSZ activity retention, for each functionalization type. The LSZ-PVA film showed higher activity than any of the SWNT-LSZ films. The noncovalent and covalent films both showed comparable specific activity to the dispersions, 81% and 63% for the films, respectively, versus 80% and 66% for the dispersions, respectively. However, a significant observation was made over the course of the assays that the noncovalent films were more resistant to dissolution over the assay period, remaining intact while the LSZ, PVA and covalent LSZ-SWNT films each dissolved completely.

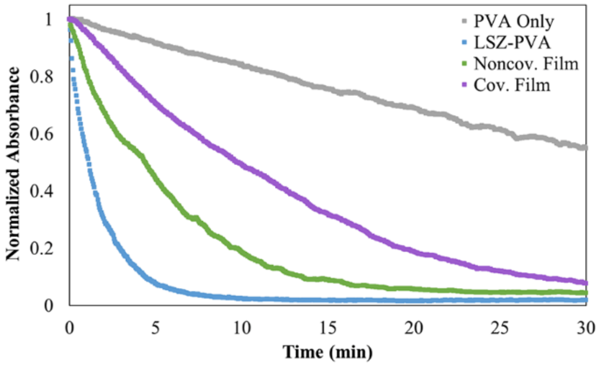

	LSZ-PVA Film	Cov. Film	Noncov. Film
Linear cell death slope	0.64	0.05	0.37
Specific activity (active units/mg LSZ)	2280	1440	1850
LSZ activity maintained (%)	100	63	81

Figure 4.7: Turbidimetric assays with films prepared with PVA as well as a table showing initial cell death slope, specific activity, and percentage of LSZ activity maintained for each film.

Finally, tensile testing results showed improved mechanical performance of LSZ-SWNT films compared to control films (Figure 4.8). Table 4.2 lists mechanical properties obtained from this data. Overall, the mechanical properties of films made with LSZ-SWNT showed higher Young’s modulus, yield stress and break point stress over PVA and LSZ-PVA films. The noncovalent LSZ-SWNT-PVA films exhibited greater yield strength and Young’s modulus. Noncovalent films had similar mechanical properties to those fabricated in Nyankima et al.[36] The covalent LSZ-SWNT-PVA films also showed higher Young’s modulus, yield strength and break point stress than PVA and LSZ-PVA films.

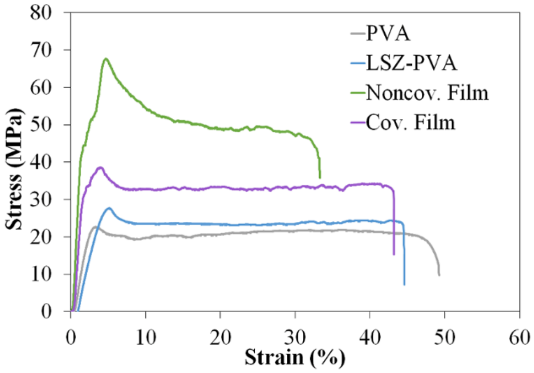

Component	Noncov. Film	Cov. Film	LSZ Film
SWNT	4 %	1 %	0 %
LSZ	25 %	2 %	24 %
PVA	71 %	97 %	76 %

Figure 4.8: Tensile testing data for films prepared with PVA as well as a table listing the composition by mass fraction of components.

Table 4.2: A summary of mechanical testing results consisting of at least 3 tests of each film type with standard deviations.

Sample	Young’s Modulus (MPa)	Yield Strength (MPa)	Yield Strain (%)	Break point stress (MPa)	Break point strain (%)	Toughness (MJ/m^3)
PVA Film	1030 ± 230	24 ± 8.8	4.72 ± 1.1	21 ± 4.2	44 ± 3.4	8.1 ± 3.1
LSZ Film	1120 ± 170	34 ± 5.2	5.04 ± 0.98	27 ± 3.5	34 ± 8.5	9.1 ± 2.6
NonCov. Film	4190 ± 360	75 ± 12	4.90 ± 0.6	48 ± 3.6	28 ± 8.9	13.4 ± 4.6
Cov. Film	2580 ± 310	39 ± 1.9	4.51 ± 0.46	33 ± 2.1	43 ± 0.5	13.0 ± 1.6

4.2 Assay Selection and Protocol Development

This work was done in collaboration with Dr. Mark Liles and graduate student Alinne Pereira in the department of Biological Sciences at Auburn University. In the antimicrobial literature, there are several methods with varying degrees of complexity which can be used to determine antibacterial activity. Selecting an assay that was suited to antibacterial testing of SWNT, meaning that SWNT would not interfere with measurements presented a challenge due to the optical properties of SWNT, including strong absorbance of visible light, and photoluminescence in infrared and near-infrared spectra. Other researchers studying the antibacterial properties of SWNT have opted for fluorescence assays in the past, however, simpler assays were chosen for this work because they are methods that are less susceptible to these small optical influences. Influences of the concentration of SWNT were investigated by normalizing the SWNT concentration to the SWNT concentration of the least concentrated dispersion. This was done by diluting with dispersant controls which had been subjected to the same sonication and centrifugation cycles as the SWNT dispersions.

Colony forming unit (CFU) counting is a powerful and straight-forward method that allows the assessment of viable cells in a given inoculum. CFU counting provides an estimate of the number of viable cells that grow when spread and incubated on an agar plate. In theory, one solitary cell gives rise to each colony, though in reality the number of cells originally in the colony is not likely a singular cell and may vary to include a small group of cells. This introduces some variance to results and necessitates multiple parallel trials and other methods for verification of antibacterial activity. Nevertheless, CFU counting is regarded as a highly accurate assay for measuring cell viability without the use of methods like cell counting, which requires expensive equipment.[134]

Optical density is an inexpensive, fast method for determining cell concentration. The advantage of this method is that the data can be measured at several time point over a long time period, allowing growth curves to be constructed. The OD growth curves are constructed by correlating the optical density to the cell population of a given suspension over time. Generally, comparisons of OD growth curves are made by comparing the lag phase and the shape of the curve relative to a neutral control. The main drawback of this method is that the SWNT treatment may interfere with the overall optical density of the suspension and slightly skew the results.[134] Though, as discussed later, this was not found to be a major factor due to the low concentration SWNT provided.

4.3 Assay Procedure

Inoculums were prepared by incubating both bacterial strains overnight in Tryptic Soy Broth (TSB) at 37 °C with shaking. The inoculums were then normalized to OD 0.5 by dilution with TSB. 360 μL of the normalized inoculums were challenged with 40 μL of each treatment which consisted of: sonicated, centrifuged dispersants (no SWNT), SWNT dispersions, normalized SWNT dispersions, and controls for a total of 17 treatments per strain. Antibiotics Vancomycin for MRSA and Chloramphenicol for *S. typhimurium* were used as a positive control and Sterile MilliQ water was used as a negative control. The challenges were incubated for 1 h at 37 °C with shaking.

An aliquot of each challenge was then inoculated at a 10^{-1} dilution in fresh TSB (100:900 μL of challenge to TSB) and transferred to a clear 96-well plate in triplicates with 200 μL per well. The plate containing all the challenges was incubated for 24 h with shaking at 37 °C in an automated plate reader and OD was measured every 30 min to build growth curves. Another aliquot of each challenge was diluted to 10^{-4}, 10^{-5} and 10^{-6} and plated into Tryptic Soy Agar plates. The plates were incubated for 24h, and the dilutions yielding roughly 30-300 colonies were picked for CFU counting. Mean, standard deviation and statistical difference of the CFU counts between treatments were conducted using non-parametric Kruskal Wallis analysis of variance and Dunn pairwise statistical tests in Rstudio.

4.4 Dispersant Selection and Dispersion Characterization

Dispersants were selected based on a range of intrinsic antibacterial activities and good SWNT dispersion capability. SDS is a surfactant that has long been used as a dispersant in the SWNT literature, but has high bacterial cytotoxicity.[135] On the other hand, Pluronic, a PEO-PPO-PEO triblock copolymer, is a polymeric surfactant which has been used to disperse SWNT at reasonably high concentrations and is regarded as being biocompatible.[135-137] DNA was chosen for convenience and biocompatibility. LSZ was chosen for convenience and activity towards Gram-positive bacteria.[31, 35, 95] Finally, TSB, a bacterial growth medium, was selected for its excellent ability to disperse SWNT.[138] Therefore, if significant antibacterial activity were found in a SWNT-TSB dispersion, it would be an important advancement towards to proving antibacterial activity of SWNT.

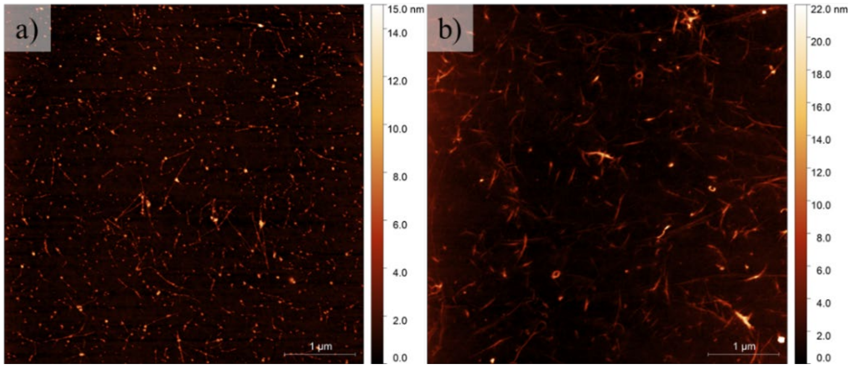

Figure 4.9: AFM scans of a) TSB-SWNT and b) DNA-SWNT.

Atomic force microscopy (AFM) was used to quantify the number of individual SWNT versus bundled SWNT (Figure 4.9 and Appendix Figure A.1). For each dispersion, a different ratio of individuals to bundles was expected, due to differing dispersive capabilities reported. Interestingly, the TSB dispersion yielded the highest ratio of individuals to bundles, at a ratio of 9.0, followed by Pluronic 6.7 and DNA at 5.7. All ratios are listed in Table 4.3. These results are significant due to theories, such as the theory of Liu et al. in the literature that the ends of individually dispersed carbon nanotube physically puncture the cell membranes of bacteria.[117] If these theories are true, then we should see increased antibacterial activity in dispersions with greater ratios of individuals to bundles with normalized SWNT concentration over the controls.

Table 4.3: SWNT concentrations, individual to bundled SWNT ratio, and average length of individual SWNT for each dispersion with standard deviation.

Sample	*Dispersion SWNT Concentration (mg/mL)*	*Individual to Bundle Ratio*	*Average Length of Individuals (nm)*
SWNT-LSZ	0.227	3.2	190 ± 49
SWNT-DNA	0.723	5.7	222 ± 52
SWNT-Pluronic	0.577	6.7	172 ± 47
SWNT-SDS	1.670	0.4	171 ± 35
SWNT-TSB	0.445	9.0	234 ± 62

UV-vis spectroscopy of each dispersion was performed to determine SWNT concentration, Figure 4.10. This was done via the Beer-Lambert law $A = \varepsilon l c$ where ε is the extinction coefficient, A is the absorbance at a specified wavelength, l is the path length, and c is the concentration of the dispersion. The specified wavelength was kept consistent at 660 nm across all sample because this was the location of a strong van Hove singularity peak, an indicator of individual SWNT dispersion. Each dispersion was diluted with ultrapure water and the absorbance at 660 nm recorded. The extinction coefficient was obtained by taking the slope of absorbance at 660 nm of dispersions serially diluted with DI water plotted against SWNT concentration.

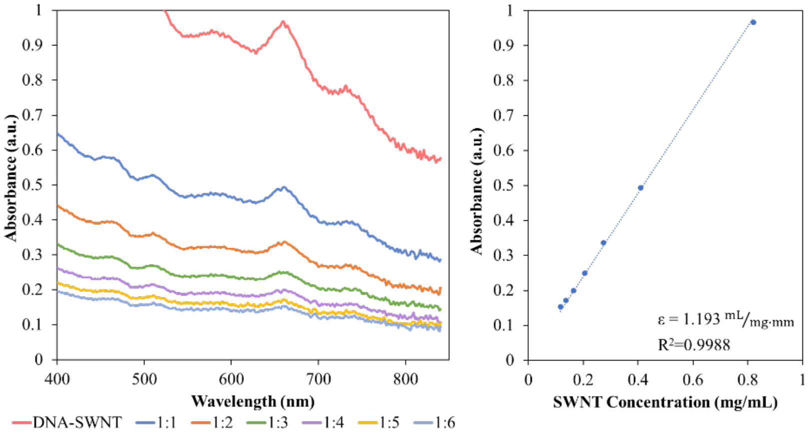

Figure 4.10: (a) UV-vis spectra of DNA-SWNT dispersions with dispersion:water dilutions and (b) Beer-Lambert plot for DNA-SWNT with extinction coefficient.

In order to differentiate dispersant and SWNT activity, the SWNT dispersions were diluted to match in SWNT concentration. In the case of this research, the LSZ-SWNT dispersions had the lowest concentration so all dispersions were diluted with their respective controls to match that concentration. The concentrations are listed in Table 4.3 for the dispersions used in this research. SDS had a much higher SWNT concentration. However, they also had a much lower individual to bundle ratio.

4.5 Colony Forming Unit Count Assays

In Figure 4.11, the decrease in cell viability after the dispersion challenges is separated by cell membrane morphology and dispersant. Table A.1 shows the CFU count data. Bacteria are divided according to their cell wall structure into gram-positives and gram-negatives. Gram-positive bacteria have a single, thick cell-wall layer comprised of peptidoglycan which provides the cell structural support. This cell wall is the primary target of the enzyme LSZ and is susceptible to damage by surfactants. Gram-negative bacteria have a more complex structure with an inner phospholipid bilayer membrane layer, followed by a thin peptidoglycan layer and an outer phospholipid bilayer membrane. Therefore, Gram-negative cells are less vulnerable to LSZ and respond more efficiently to cell wall or membrane disruption by surfactants.

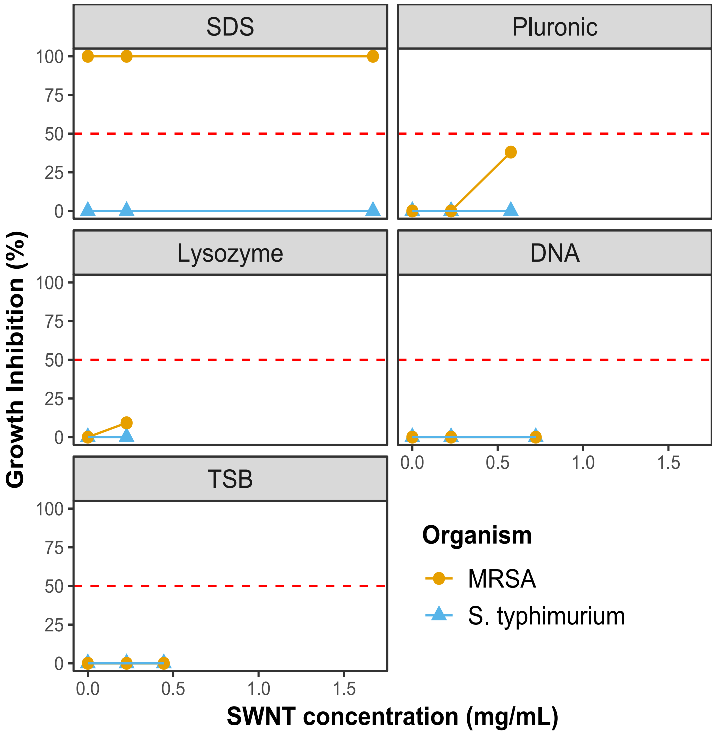

Figure 4.11: CFU count data of MRSA and *S. typhimurium* presented as growth inhibition relative to a water control and plotted against SWNT concentration of dispersions.

The Gram-negative bacterium, *S. typhimurium*, was unaffected by any of the challenges with no decrease in viability. The Gram-positive bacteria MRSA exhibited some dispersant dependence in its response. The surfactant SDS exhibited complete inhibition of the bacteria regardless of SWNT concentration. Pluronic, a mild surfactant specifically selected for its low cytotoxicity, had no effect on bacterial viability except when coupled with high concentrations of SWNT, with a similar result for LSZ. Interestingly, all of the aforementioned dispersants act directly on the cell-wall, destabilizing the peptidoglycan structure either weakening the cell-wall or causing it to burst. MRSA seemed unaffected by TSB and DNA dispersions, regardless of their SWNT concentration. TSB and DNA were chosen as biologically compatible dispersing media and exhibited no hindrance to cellular viability.[34, 138] Dispersions which had normalized SWNT concentration showed no interference in cell viability aside from SDS and LSZ, though antimicrobial activity of SDS is independent to SWNT presence.

4.6 Optical Density Assays

Growth curves determined by optical density assays are shown in Figure 4.12. *S. typhimurium* growth curves showed similar behavior to the water control, independent of SWNT or dispersant treatment. *S. aureus* inocula showed poor growth compared to the to the water control in each case except for those treated with Pluronic. As expected, based on the results from CFU count data, SDS challenges against *S. aureus* showed significant growth delay, requiring approximately eight hours for growth detection, indicating much fewer viable cells present after the treatment. A delay in exponential growth indicates reduced metabolic activity and/or a low population of viable cells in the inoculum. Unexpectedly, the *S. aureus* inoculum treated with normalized SWNT-TSB also showed a marked delay in detectable growth, despite higher SWNT concentration closely following the control. Since the error is also very high, the results could be due to an experimental error in which some of the wells of the 96-well plate dried over the measurement period.

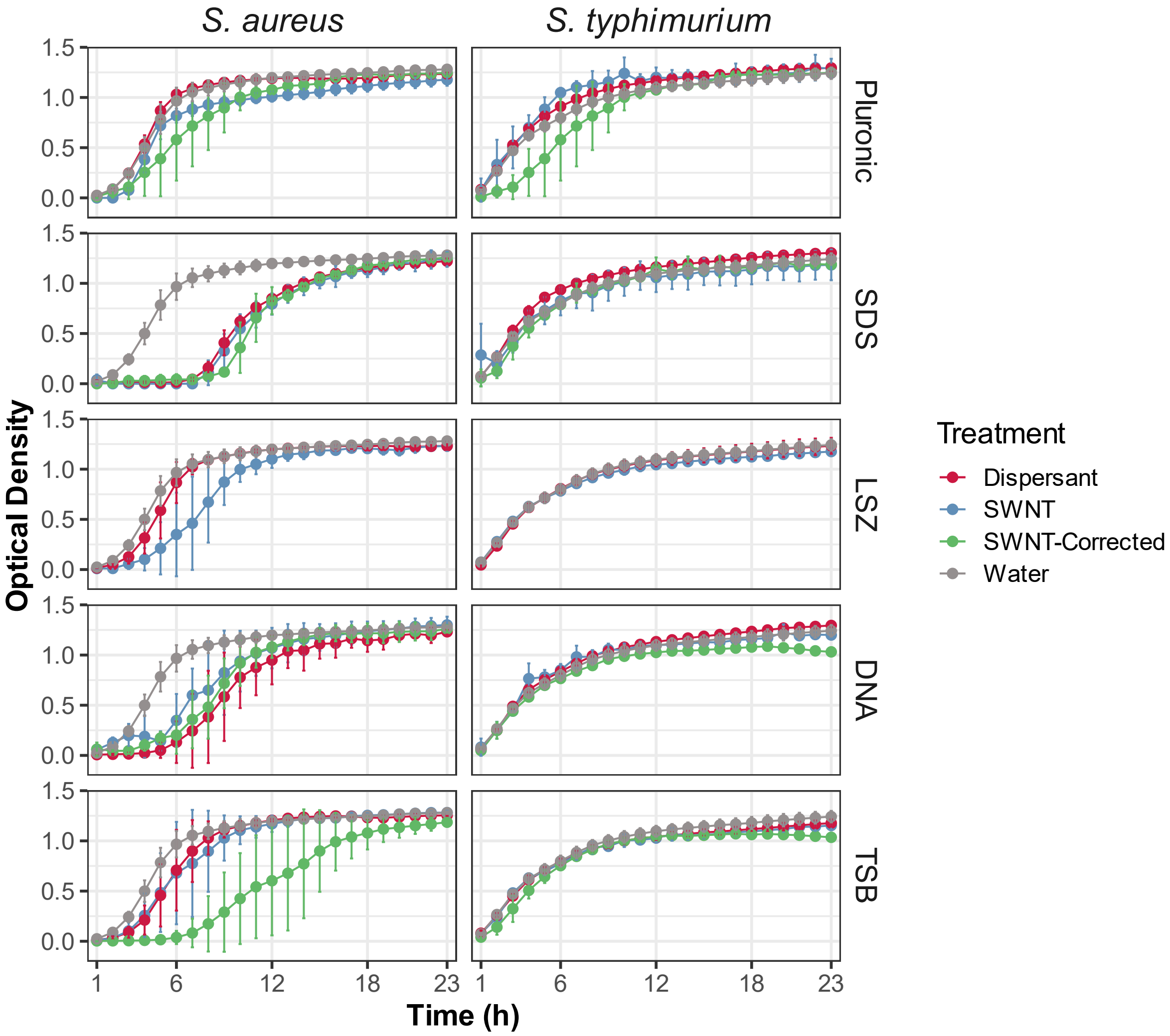

Figure 4.12: OD growth curves of bacteria challenged with the 17 treatments.

4.7 Conclusions

This project set out to resolve some of the controversy in the literature on SWNT antibacterial activity. This was achieved by investigating the effects of covalent functionalization on stability and function of SWNT-LSZ conjugates. First, investigations were done on the effects of covalent functionalization of SWNT-LSZ conjugates which demonstrated the role of SWNT in enhancing antibacterial activity of lysozyme. Additionally, the use of chemically bound LSZ-

SWNT lead to improved dispersion state and longer duration of bacterial lysis over noncovalent LSZ-SWNT. Films prepared with LSZ-SWNT dispersions maintained similar LSZ activity to their dispersions and had greater stability as well as higher yield strengths, Young's moduli, and break point stresses.

The literature surrounding SWNT as an antibacterial material has suffered from work requiring a multidisciplinary approach but largely conducted by researchers without microbiological or SWNT dispersion expertise. The results from this research indicate that antimicrobial activity is not an intrinsic property of SWNT, but instead a synergistic interaction between the nanotubes and sensitizing factors such as dispersant and experimental conditions. Therefore, SWNTs alone are not able to exert enough stress to kill healthy microbial cells. These synergistic effects are more pronounced in Gram-positive bacteria which are more vulnerable to cell-wall disruption due to their reliance on a single peptidoglycan layer. To accurately assess the intricate effects of SWNTs on microbial cells, close care should be taken to avoid introducing sensitizing factors in the experimental design as well as choosing appropriate, biologically compatible dispersing agents such as TSB or DNA.

Chapter 5: Dispersion and Self-Assembly of dsDNA/SWNT and CNC

This research utilized two self-assembling anisotropic mesogen systems, dsDNA/SWNT hybrid mesogens and CNC mesogens, to study dispersion state and self-assembly of nanocylinder systems. In recent years, there has been growing importance of developing solid cholesteric materials for decorative, anti-counterfeiting, and optical device applications. It has been demonstrated for CNC that these films can reflect circularly polarized light over a specific range of wavelengths which could be useful for many anti-counterfeiting applications. Due to the intrinsic random assembly of the cholesteric fingerprint texture, each dispersion has a different cholesteric pattern, just like a human fingerprint. Therefore, a major application for these materials is for unique identification of high value documents or products. Cholesteric films also have a high importance in development for polarizers and color filters for liquid crystal displays (LCDs). Increasing the efficiency of LCDs can be achieved by having decreased absorbance in polarizers used in these displays and "light recycling," increasing energy efficiency of LCDs dramatically.

Cholesteric lyotropic liquid crystal films may be produced for these applications by developing an understanding of how shear affects microstructure in order to control their texture and optical properties. The dsDNA/SWNT system is of particular interest to study differences in self-assembly between nematic and cholesteric systems. The DNA/SWNT work was mostly an investigation of dispersion state and stability at high concentration. The CNC work was focused on self-assembly dynamic under various shear and drying conditions in order to produce films with controlled microstructure and thus optical properties.

5.1 Small-Angle Neutron Scattering (SANS)

Discussion of the research presented herein requires some additional background on small-angle neutron scattering (SANS), the strengths and limitations of the SANS method as well as its applicability to the study of self-assembly in anisotropic nanomaterial systems. Small-angle scattering methods have long been used to study structured materials with features in the 1 to 1000 nanometer range. In small-angle scattering (SAS), highly collimated beams of either X-rays or neutron are elastically scattered by the sample in the beam path, resulting in a scattering pattern that can then be analyzed to give information about the size, shape, and orientation of the structured material, Figure 5.1.[139-140] SAS methods are particularly useful for systems which do not have long range, or a high degree of ordering, but rather have some inhomogeneity in their ordering.[139]

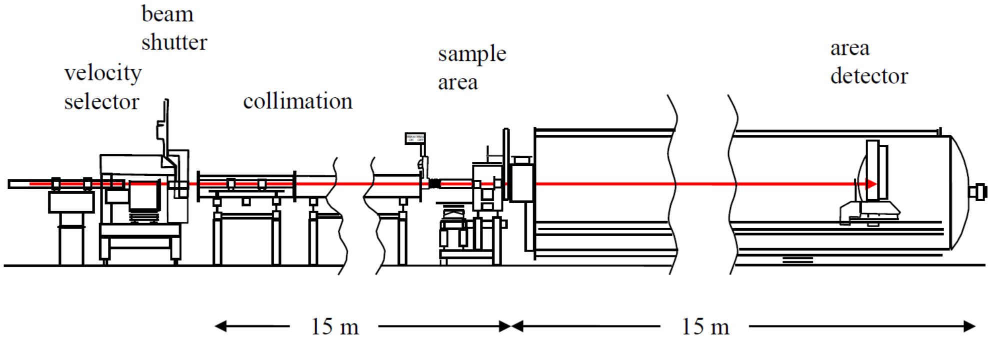

Figure 5.1: A schematic of a 30 m SANS instrument at the National Institute of Standards and Technology (NIST). Reproduced from Hammouda.[140]

The main difference between small-angle X-ray scattering (SAXS) and SANS is that X-rays scatter from the electron cloud of an atom, varying with electronic density, while neutrons scatter from the nucleus, varying with scattering length density. The primary advantage of SANS over SAXS is the deuteration method. The deuteration method takes advantage of the differing scattering length densities of hydrogen and its isotope, deuterium, to provide more contrast to the component of interest. For example, the aqueous CNC system, the difference in the scattering length density of CNC and H_2O is quite small, which causes the neutrons to scatter from the water molecules as well as the CNC. However, in the D_2O CNC system, the scattering length densities are far different and there is a stronger scattering pattern from the CNC. The behavior of D_2O is remarkably similar to H_2O, meaning that behavior of D_2O systems is largely the same as the behavior of H_2O systems. Because of the deuteration method, an additional benefit of the SANS method is different components of a material can be de-coupled from one another, allowing the measurement of composition fluctuations as well as density fluctuations in a sample. SAXS methods can measure density fluctuations only but lack an equivalent contrast method and instead rely upon heavy atom labels to achieve similar effect, which can change intra- and intermolecular interactions and thus self-ordering behavior. Another major limitation of SANS over SAXS methods is the much higher flux achieved from X-ray synchrotron sources, over either continuous or spallation cold neutron sources.

SANS measurements are taken in reciprocal (Fourier) space and plotted as scattered intensity as a function of the scattering vector, Q, given by:

$$Q = \frac{2\pi\theta}{\lambda} \tag{5.1}$$

Where λ is the neutron wavelength, and θ is the scattering angle.[140] This data is then used to analyze shape, size and orientation of the molecules or particles, discussed in more detail later.

Neutron scattering experiments in this research were conducted on the NGB 30 m and NGB 10 m small angle neutron scattering (SANS) beam lines at the NIST Center for Neutron Research in Gaithersburg, MD. For combined rheology and SANS (rheoSANS) experiments, the NGB 30 m instrument was configured with 6 Å neutron wavelength and a sample to detector distance of 8.5 m for CNC samples and 5 Å neutron wavelength and a sample to detector distance of 1m for DNA/SWNT. The sample environment was an Anton Paar MCR501 rotational rheometer with a titanium cup and hollow bob (48.0 mm bob diameter and 50.0 mm cup internal diameter for CNC, and 27.0 mm bob diameter and 28.0 mm cup internal diameter for DNA/SWNT) specifically designed for SANS measurement compatibility. CNC measurements were performed at 10 °C and DNA/SWNT at 25 °C. The scattering data were reduced to an absolute scale using the standard NIST Igor procedures. Additionally, for CNC, rectangular apertures 18 mm by 10 or 0.25 mm were used for radial and tangential measurements, respectively. Measurements were performed through both the radial and tangential directions in order to probe the microstructure in the flow-vorticity and gradient-vorticity planes, respectively. Due to the complicating effects of the curved transmission path in the tangential configuration, the tangential scattering data were scaled to match the absolute radial scattering intensity in the common (vorticity) direction.

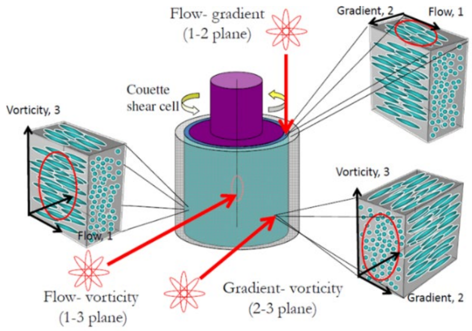

Figure 5.2: Schematic of the rheoSANS rheometer and beam path configurations.[141]

5.2 Dynamics of CNC Self-Assembly During Shear and Post-Shear Relaxation

The understanding of anisotropic nanomaterial orientation dynamic during shear and post-shear relaxation is critical to the fabrication of films with controlled anisotropic mechanical and/or optical properties. The CNC SANS work was done in collaboration with Dr. Alexander Haywood, formerly of the Davis research group, and Dr. Katie Weigandt of NIST, who performed the rheoSANS measurements. Three-region viscosity versus shear rate behavior has been observed in biphasic dispersions of CNC but was rather elusive in fully liquid crystalline samples. Though Orts et al. observed a cholesteric-to-nematic alignment transition behavior from intermediate to high shear, Ebeling et al. observed vorticity alignment behavior at intermediate shear rates for CNC.[95, 103, 142] In this work, potential three-region viscosity and CNC orientation behavior was investigated by radial and tangential rheoSANS configurations.

The phase behavior for the CNC dispersions in D_2O was investigated by polarized optical microscopy. The isotropic-to-biphasic critical concentration, ϕ_I, was determined to be 3.16 vol% CNC, where small anisotropic droplets were observed in the mostly isotropic dispersion. The relative amount of anisotropic phase increased with concentration until a fully liquid crystalline dispersion was obtained at $\phi_{LC} = 6.50$ vol%. Another important observation was made that the rheological indication of the gel phase that lies beyond the LC phase, occurred at $\phi_{gel} = 7.16$ vol% while the optical indication for gel phase occurred at 8.48 vol%.

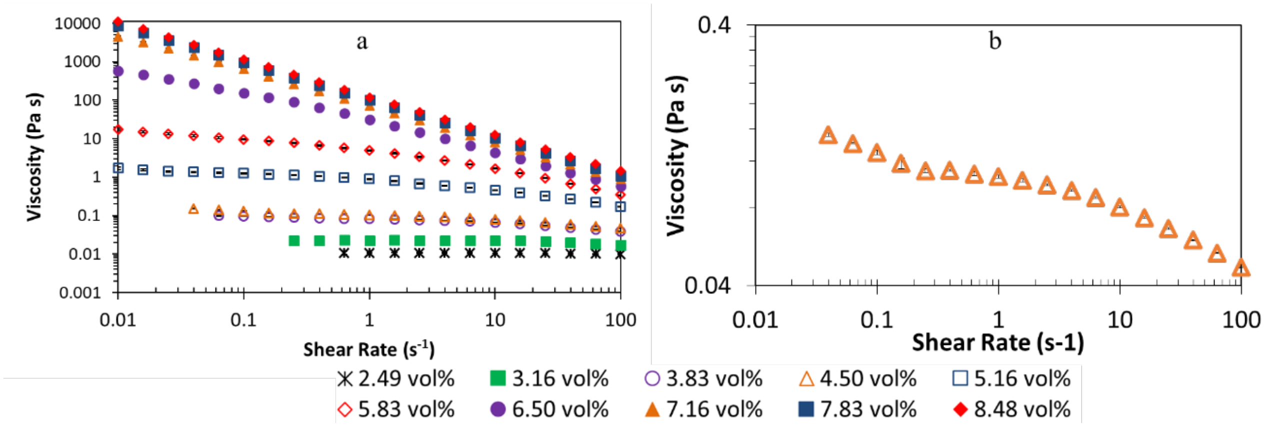

Figure 5.3: Viscosity versus shear rate data for a) all samples and b) 4.50 vol% CNC. Adapted from Haywood et al.[60]

Viscosity versus shear rate behavior was then investigated, shown in Figure 5.3. Three region behavior is clearly present for biphasic CNC dispersions, when plotted on a smaller scale, as shown by Figure 5.3b. However, for liquid crystalline samples the transitions between the three regions is much more difficult to detect from a visual inspection of the plot. Generally, shear thinning behavior, similar to Regions I and III, follows a Power Law model given by:

$$\eta = K\dot{\gamma}^{n-1} \tag{5.2}$$

Where n is the power law index and K is the consistency index. Power law fits were made at low (0.01 to 0.1 s^{-1}) and high shear rates (100 to 1000 s^{-1}) and found significant differences in power law indices between Regions I and III, shown in Table 5.1. However, attempts to locate the plateau of Region II, for LC samples and the exact onset of Regions II and III for biphasic samples proved difficult. In the hydroxypropyl cellulose (HPC) system, a cholesteric LC polymer made from cellulose, a hesitation point at intermediate shear indicated Region II rather than the idealized large plateaus seen in other model LC polymers.[143]

Table 5.1: Power law indices for CNC dispersions at low and high shear

CNC Conc. (vol %)	n (low $\dot{\gamma}$)	n (high $\dot{\gamma}$)
3.83	0.92	0.77
4.50	0.84	0.77
5.16	0.80	0.58
5.83	0.74	0.36
6.50	0.41	0.12
7.16	0.14	0.05
7.82	0.06	0.02
8.48	0.01	0.06

Reduced two-dimensional scattering data for the 2.49, 4.50, 7.16, and 8.48 vol% dispersions are shown in Figure 5.4. Over the full range of shear rates, the 2.49 vol% dispersion showed an isotropic scattering pattern. The 4.50 vol% dispersion showed some anisotropic alignment up at 1 s^{-1} with little change when increased to 10 s^{-1} then significantly more alignment when increased to 100 s^{-1}. The 7.16 and 8.48 vol% dispersions showed some initial alignment perpendicular to the flow direction, however these were attributed to loading and relaxation effects. The 7.16 and 8.48 vol% dispersions also showed strong alignment in the flow direction, even at intermediate shear rates.

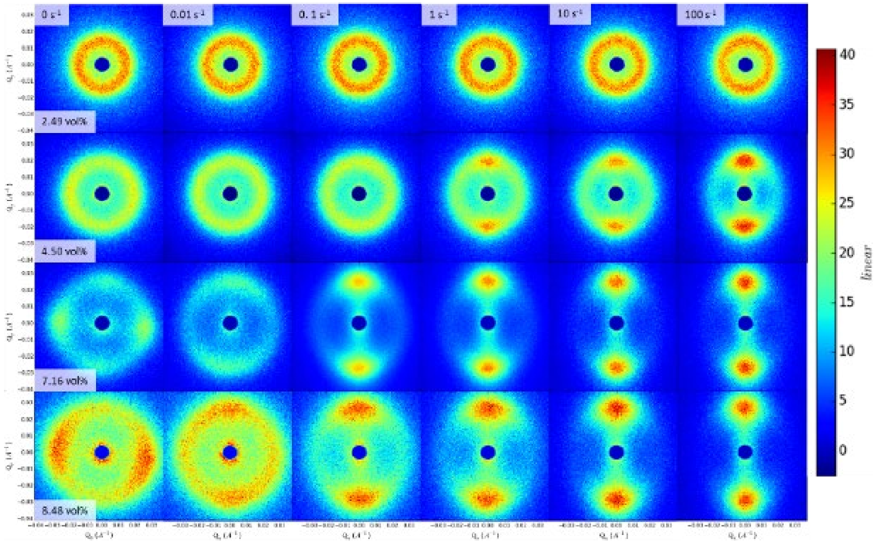

Figure 5.4: Reduced two-dimensional SANS data for the 2.49, 4.50, 7.16, and 8.48 vol% CNC dispersions. Adapted from Haywood et al.[60]

In order to quantify the anisotropic alignment in the flow direction, an annular average of the 2-D scattering data was taken over a 0.0056 Å range of the scattering vector, Q, centered about the maximum intensity scattering peak. A Legendre series expansion was then fit for the first six terms to the annular average data, using the method of Burger et al.[144] The Legendre series expansion is given by:

$$F(q,\phi) = \sum_{n=0}^{\infty} a_n P_{2n}(\cos\phi) \tag{5.3}$$

Where a_n are fitting coefficients and the functions, P_{2n}, are Legendre polynomials and ϕ is the azimuthal angle over which the data was averaged. The SANS order parameter, $\bar{P}_2$ is calculated directly from a_1 and is given by:

$$\bar{P}_2 = \frac{a_1}{5} \tag{5.4}$$

The value of $\bar{P}_2$ varies from 0 for isotropic (random) orientation and 1 for perfect nematic orientation in the flow direction. The results of the calculated order parameter were plotted versus shear rate in Figure 5.5. In the isotropic and low biphasic concentrations, 2.49 and 3.16 vol%, the order parameter is zero until very high shear where it begins to increase slightly. Especially for biphasic samples, 3.83 to 5.83 vol%, there are clear transitions from Regions I to II, a distinct Region II plateau, then a transition from Region II to III. The Region II plateaus for these samples were in the 1 to 10 s^{-1} range. Interestingly, the LC 6.50 vol% CNC dispersion exhibited a region of increasing order parameter in place of the expected plateau in Region II. The three-region behavior is apparent at the transition to the gel phase at 7.16 vol% but diminishes at higher concentrations.

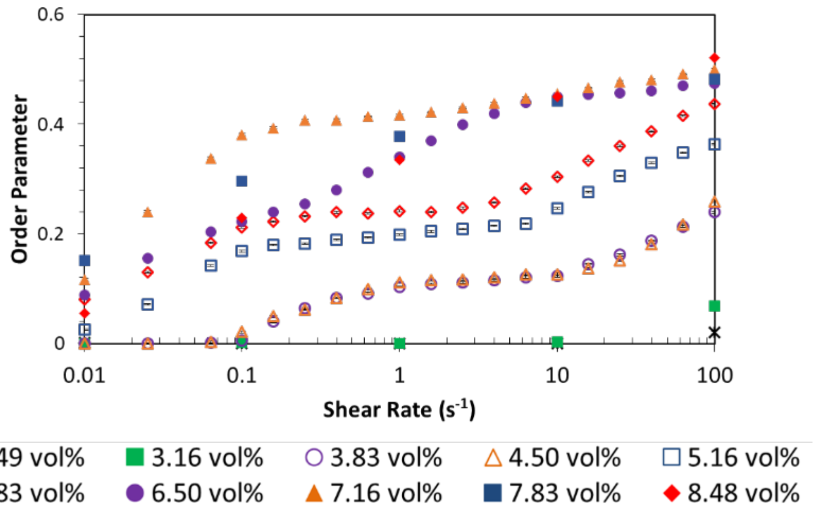

Figure 5.5: Order parameter versus shear rate for CNC samples. Adapted from Haywood et al.[60]

A direct comparison between viscosity and order parameter in biphasic CNC samples is shown in Figure 5.6. As mentioned previously, the transitions between regions and Region II plateau are not clearly discernable from the viscosity versus shear rate plots. However, order parameter versus shear rate shows more clearly defined transitions. For each biphasic concentration, order parameter increases with low shear rate, reaches a plateau at intermediate shear rates, then increases again at high shear rates. Although the three-region behavior described by Onogi and Asada is unique to LCs, these biphasic dispersions exhibit similar behavior which may mean that both the order parameter and viscosity versus shear rate behavior have similar microstructural origins.[145] The onset of region transitions determined by this method can be found in Table 5.2. These region onsets could be determined more accurately if there were more intermediate shear rates investigated, but additional shear rates were not investigated due to beamtime restrictions.

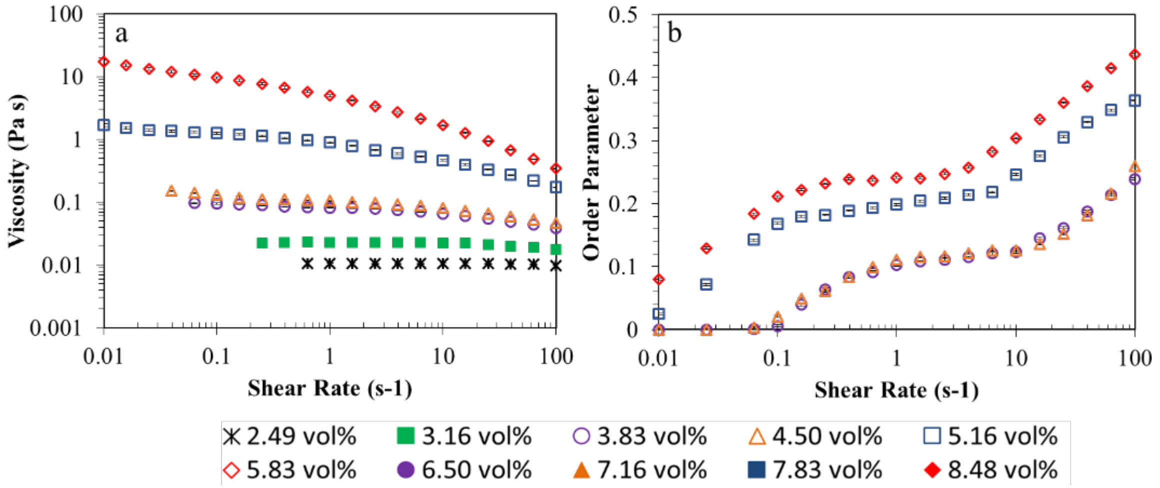

Figure 5.6: a) Viscosity and b) order parameter versus shear rate for biphasic CNC dispersions. Adapted from Haywood et al.[60]

Table 5.2: Onset of region transitions for biphasic dispersions determined from SANS.[60]

CNC conc. (vol%)	Onset of region II (s^{-1})	Onset of region III (s^{-1})
3.83	1.00	10.00
4.50	1.00	10.00
5.16	0.16	6.31
5.83	0.25	2.51

Based on these results and rheo-optical investigations, it was hypothesized that the anisotropic domains that exist in biphasic dispersions elongate in Region I and align their directors with the flow direction. This results in an increase in order parameter and a corresponding decrease in viscosity. Transitioning to Region II, the directors of liquid crystalline domains orient in the direction of shear, but the shear forces are not sufficient to align the isotropic phase CNC. This would be consistent with scattering patterns of biphasic dispersions at intermediate shear rates having both anisotropic nodes and an isotropic ring. The transition from Region II to Region III is believed to be the shear rate that results in isotropic phase alignment in the flow direction, as observed for the isotropic (2.49 vol%) and biphasic transition (3.16 vol%) CNC dispersions.

Relaxation of CNC dispersions after shear cessation was also explored over a relaxation period of one hour by SANS measurements. Order parameter was then calculated and plotted against time in

Figure 5.7. Gel and LC phase, aside from 6.50 vol% samples did not relax significantly over the measurement period. The LC 6.50 vol% CNC dispersion exhibited significant relaxation, but the relaxation was inhibited at higher LC concentrations. Biphasic samples each experienced complete relaxation to a globally random orientation. The relaxation data obtained is essential to fabrication of sheared films with controlled microstructure orientation.

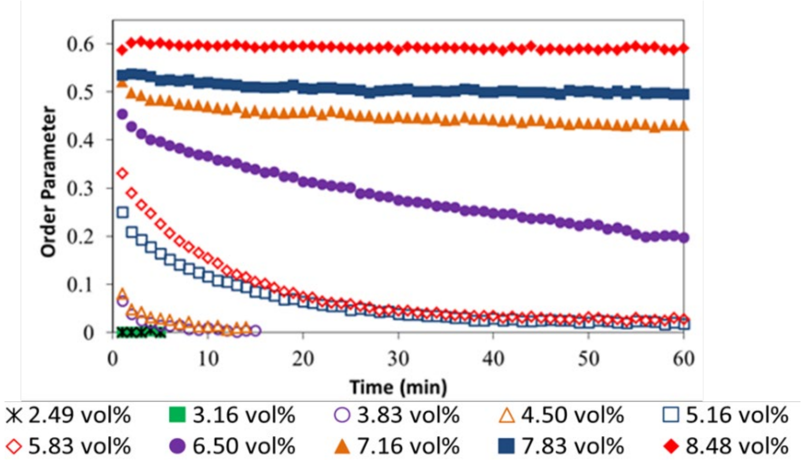

Figure 5.7: Order parameter plotted against time during relaxation after shear cessation.

5.3 dsDNA/SWNT Dispersion and Self-Assembly

Research in dispersion of SWNT with dsDNA has shown excellent dispersion of SWNT.[146-149] The majority of research on DNA-SWNT interactions has focused on ssDNA. The interactions off ssDNA and with chiralities of SWNT are well understood through experimental and computational work.[149-152] For dsDNA, the major groove was originally hypothesized by Lu et al. to be the adsorption site of SWNT.[153] However, these DNA-SWNT interactions were found computationally to be unfavorable.[154] While the exact molecular interaction between the SWNT and dsDNA are not yet known, the interaction of SWNT with dsDNA is generally agreed to be principally dependent on π-π stacking interactions with the DNA base pairs.[147, 155-159]

The efforts to understand the interactions and structure of the SWNT/DNA adduct complex have been carried out computationally and experimentally. Cathcart et al. proposed an unwinding of frayed dsDNA strands to wrap SWNT in an ordered coating, as shown in Figure 5.8.[147] Polymeric dispersants, such as poly(vinylpyrrolidone) (PVP) has a strong enough binding energy with SWNT to overcome the enthalpy decrease of wrapping, though it is not ordered.[16] Similarly, dsDNA may exhibit this behavior however there is more complexity in this interaction due to the already highly ordered double-stranded structure. For this reason, it is necessary to provide enough energy to denature or "fray" the dsDNA enough for these interactions to occur. This energy is provided by either thermal annealing of the dsDNA or providing energy via sonication.[147, 160] As previously stated, the van der Waals forces of SWNT interactions must also be overcome to produce de-bundled, individualized SWNT. Sonication provides a facile method to overcome both energy barriers simultaneously. Adsorption process of a frayed dsDNA strand is a very fast process, confirmed experimentally and computationally.[147, 151] The progression from disordered coating to partial ordering has a large entropic barrier, thus requiring a long time period, around 50 days, with a fully ordered coating taking much longer.[147] However, beyond stage 2 of Figure 5.8, no evidence has been provided for the proposed slow stage 3 and 4 processes the would lead to an ordered coating of ssDNA.

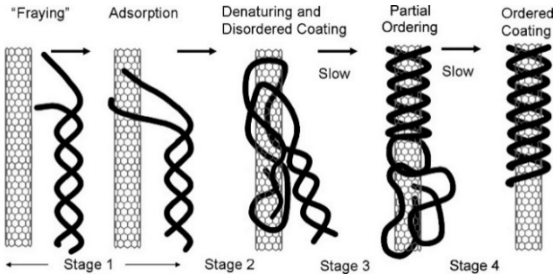

Figure 5.8: A full mechanism for the slow process of the adsorbed, frayed DNA going through a slow denaturation and wrapping process to arrive at an ordered coating on the SWNT. Reproduced from Cathcart et al.[147]

Wu et al. described a SWNT-DNA hybrid structure similar to the frayed structures of Cathcart et al. with DNA that is partially single-stranded and partially double-stranded. Rather than sonicating to fray, as reported by Cathcart et al., Wu et al. thermally annealing the dsDNA at 95 °C into a ss- and dsDNA hybrid.[147, 160] Through a combination of restriction enzyme assays and molecular dynamic simulations, it was found a hybrid dsDNA structure was maintained and stable in the long-term, disproving the slow denaturation to ssDNA process described by Cathcart et al. but confirming the favorable interactions of frayed SWNT.[147] Although there were not high-concentration phase behavior studies associated with either of these works, they provide significant insight into the structure of dsDNA-SWNT system.

Previous work from the Davis group has shown that dsDNA-SWNT dispersions can be either nematic or cholesteric.[146] Non-centrifuged dispersions of dsDNA-SWNT, after concentration, exhibited nematic liquid crystalline structures due to inhibition of dsDNA cholesterogenicity by the SWNT bundles present. Cholesterogenic dsDNA-SWNT dispersions were obtained by centrifuging the samples to remove SWNT bundles so only individually dispersed SWNT remained, then, when evaporated to increase concentration, the dsDNA helix structure drove cholesteric assembly. Rheological experiments with the cholesteric dsDNA-SWNT dispersions at increasing concentrations and low shear rate yielded a characteristic increase in viscosity in the biphasic region and a sharp decrease at the liquid crystalline phase transition, ϕ_{LC}, then increasing into the gel phase, shown in Figure 5.9.

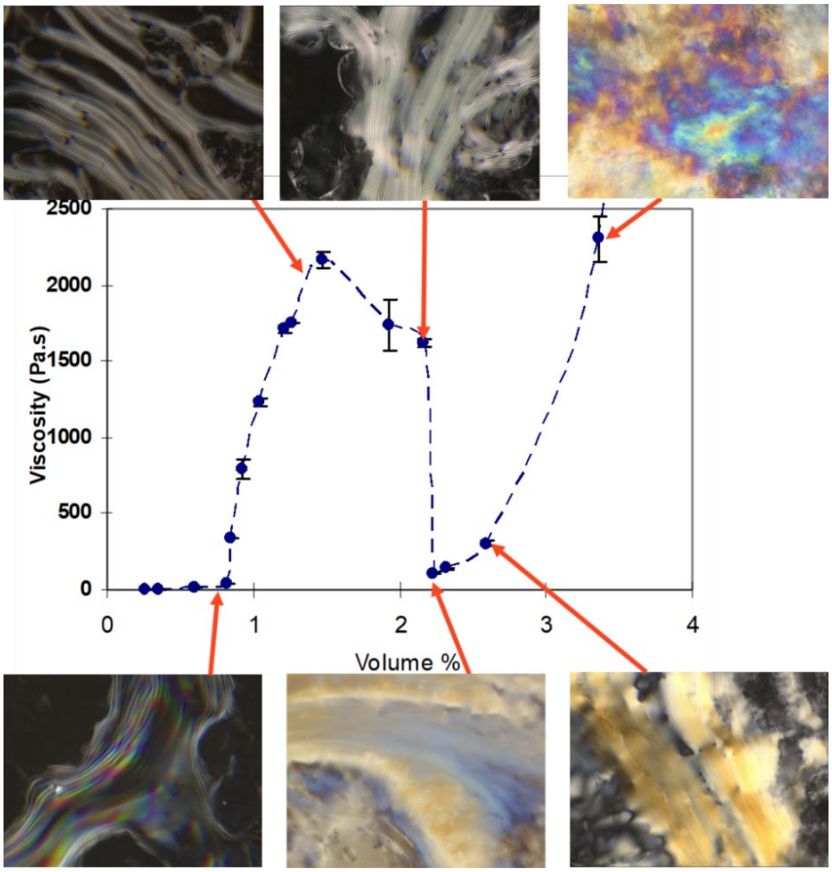

Figure 5.9: Low-shear viscosity vs. vol % SWNT for SWNT-DNA dispersion with microscopy images. Adapted from Ao et al.[146]

The cholesteric LC phase behavior of dsDNA-SWNT could arise due to dsDNA ends of the hybridized DNA interacting and causing helical stacking. The introduction of chiral mesogens or dopants to a LC phase tends to induce chirality also in the macroscopic phase.[43] Therefore, the hybridization of dsDNA to a frayed DNA structure may be vital to the development of a chiral LC phase. However, the chiral nature of dsDNA may not be sufficient to induce a chiral microstructure when larger bundles of SWNT are present, as in the case of an uncentrifuged mixture. Hence, concentrated samples made from uncentrifuged dsDNA-SWNT form nematic phases.

The original goal of this project was to investigate rheological and rheo-optical properties of cholesteric structure, and compare them with nematic structure, since both are possible with this hybrid mesogen system, and making optical films.[146] The initial research in this area focused on first obtaining similar results to Ao et al.[146] Initial experiments with concentrating the reported cholesterogenic dsDNA-SWNT mass ratio of 0.75 wt% dsDNA to 0.1 wt% SWNT yielded supernatants with some cholesteric structure, however there was a high degree of aggregation, with very large aggregates occupying the majority of the volume, shown in Figure 5.10. This result sparked a long journey with the aim of determining the reason for the aggregation and mediating it so that research in this area could progress.

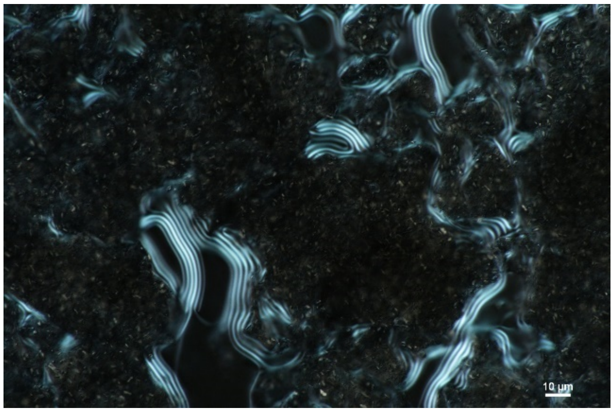

Figure 5.10: A cross-polarized optical image of a concentrated supernatant of dsDNA/SWNT. Taken with 60x objective with DIC filter and the SWNT used was HiPCO P1001.

This work used the dsDNA from the same manufacturer and source as Ao et al.[146] and for the majority of these experiments, HiPCO SWNT was used due to its similarity in electronic structure, purity and production process to the SWNT used in Ao et al. Meijo eDIPS 1.5-P SWNT was also used and has similar electronic structure and purity but differs in production process. Each experiment was done using a freshly centrifuged dispersion of dsDNA-SWNT. A summary of the variables explored in these experiments can be found in Table 5.3.

Table 5.3: Experimental variables in dsDNA-SWNT dispersion.

Variable	Variation
dsDNA concentration	± 0.5 wt% dsDNA
dsDNA salt content	± 1 wt% salt and nearly total salt removal
Pre-sonication mixing	Added high and low shear premixing methods
Sonication conditions	Ice bath and sonication vessel adjustment
SWNT	Adjusted manufacturer

The first investigation was into dsDNA concentration salt content. dsDNA concentration was varied in increments of 0.25 wt% to ± 0.5 wt% from the reported cholesterogenic dsDNA-SWNT mass ratio. In the literature, salt content has been shown to affect the self-assembly dsDNA-SWNT systems, with higher salt content decreasing repulsive interactions, and inducing more ordered condensed phases.[161] The difference in salt content of the dsDNA used in this work and that used in Ao et al. was about 1%. Therefore, 1% by weight of dsDNA was added to the dispersion, with no changes being observed in the concentrated state. It was hypothesized that the salt concentration was higher than required for the dsDNA to sufficiently repel one another and caused aggregation as the SWNT approached one another. De-salting of protein solutions is a relatively simple process, for which a stirred pressure filtration cell (Amicon stirred cell) was used to filter water and salt, leaving free DNA and dsDNA-SWNT. This also had the effect of increasing concentration of the dispersion. Each experiment used a freshly centrifuged dsDNA-SWNT dispersion and was filtered based on solvent volume in varying amounts, with different volumes of solvent, the results were unchanged. One dispersion was filtered until only 10% of its original volume, washed with DI water, then filtered again to 10% of its original volume, removing nearly all salt. However, these dispersions also yielded large aggregates when concentrated.

Further investigations largely focused on mixing conditions. Prior to sonication, the dispersions were mixed with a spatula to better disperse the SWNT powder. However, the pre-sonication mixing methods were also adjusted. This included low-shear methods such as vortex mixing and overnight bottle rolling as well as high-shear methods such as homogenization and bath sonication. There were no appreciable effects from these pre-sonication shearing methods on the self-assembly of concentrated supernatants. The high temperatures, pressures and shear forces generated by sonication were thought to have contributed to the loss of DNA structure and resulted in the disordered aggregates.[162] Sonication power was then lowered in an attempt to remedy this, to no effect. The sonication vessel was also changed from glass to a stainless steel one in an effort to increase heat transfer to the surrounding ice bath.

Despite aggregation, more cholesteric character was shown by the dispersions, especially with the Meijo SWNT, which had been homogenized prior to sonication. Concentration to the isotropic-to-biphasic critical concentration, ϕ_I, was assisted with hydrogel beads, which were shown to absorb water and leave behind the free dsDNA and dsDNA-SWNT, as done by Abkari et al. for graphene oxide.[163] The beads were determined to absorb only water and ions by concentrating a sonicated dispersion of dsDNA and measuring dsDNA concentration by UV-vis spectroscopy, finding the total mass of aqueous dsDNA to be unchanged. The use of the hydrogel beads for the purposes of concentration had no observed effect on the microstructure or self-assembly behavior. Dispersions of dsDNA- SWNT (Meijo) were made in D_2O (0.75wt% dsDNA and 0.1 wt% SWNT), centrifuged and uncentrifuged, using these methods for SANS studies.

The goal of rheoSANS experiments was to obtain information about the orientation parameter versus shear rate and possibly gain more insight into the shear effects on the microstructure of cholesteric and nematic liquid crystals. The scattering length density of dsDNA was found to be similar to D_2O while the SWNT were found to scatter weakly at all concentrations of D_2O. Therefore, purely D_2O was used in the dispersion in place of water, which had little effect on the microstructure. The results from the rheoSANS experiments are shown in Figure 5.11. The weak nature of SWNT scattering causes the plots to have more noise than the plots obtained in the CNC work. In all samples, it is clear from the scattering pattern that the anisotropy is high in the case of high shear rates (100 to 1000 s^{-1}).

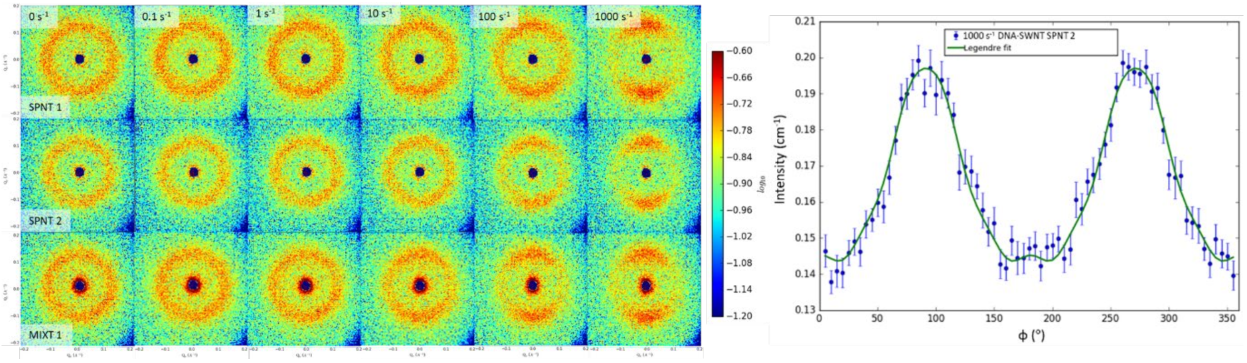

Figure 5.11: Reduced 2-D SANS data from concentrated dsDNA-SWNT dispersions at increasing shear rates as well as the Legendre fit over the annular average of the 2-D scattering data for one of the concentrated supernatant samples. Here, SPNT refers to the supernatants (centrifuged samples) and MIXT refers to the mixture sample.

From this point the annular average was taken, the Legendre fit is applied (Figure 5.11) and the orientation parameter for each sample and shear rate was obtained, yielding Figure 5.12b. There is an increase in supernatant samples, a plateau region between 1 and 10 s^{-1} shear rates followed by a further increase in order parameter. No such feature is distinguishable in the viscosity versus shear rate plot, in Figure 5.12a. However, there is a notable kink in the viscosity around 1 s^{-1}, transitioning between two shear thinning regions. The behavior of the order parameter in the mixture sample has two short plateau regions, from 1-5 s^{-1} and 20-100 s^{-1} with a dramatic increase in orientation parameter between them. Any conclusions that could be drawn from this would be purely speculative as the sample was observed to be very aggregated and disordered, which makes understanding the behavior of the system difficult to predict.

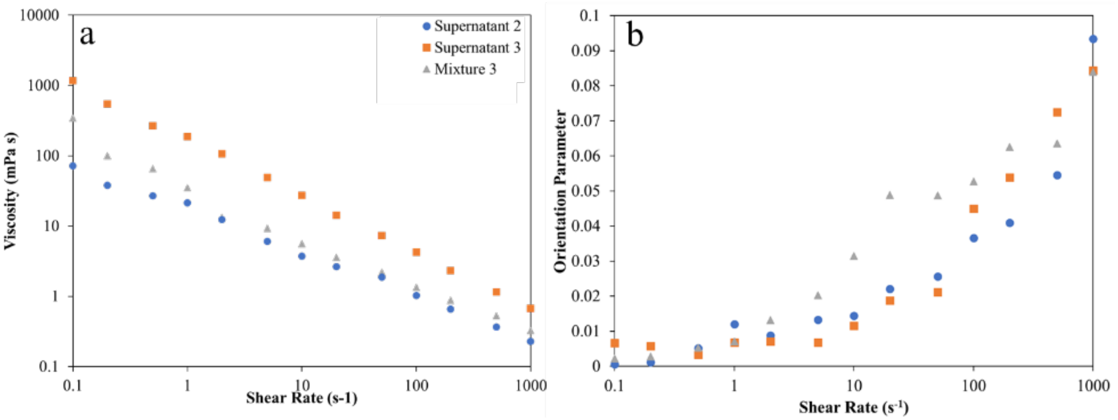

Figure 5.12: a) Steady shear viscosity and b) global orientation parameter versus shear rate for dsDNA/SWNT samples.

Recently, a new SWNT supplier was selected on the recommendation of Wu et al.[160] These SWNT, again had similar electronic structure, purity and production process to the SWNT used in Ao et al.[146] Thus, NanoIntegris Super-purity SWNT were used in the following experiments. Initial experiments yielded similar results to the ones mentioned previously. However, based on a review of Wu et al., it was possible that more thermal stress on the dsDNA would assist the "fraying" described by Cathcart et al. and subsequent adsorption of frayed ends on SWNT.[147, 160] The dispersion was made without replacing ice during the sonication procedure to add some thermal stress without completely disassociating the DNA strands. The resulting dispersion was concentrated to obtain a flocculated biphasic dispersion, shown in Figure 5.13a. The dispersion clearly exhibited cholesteric anisotropic phases but the image without crossed polarizers reveals that the dispersion still contained many flocs of dsDNA-SWNT. A very high biphasic sample was later obtained with flocs clearly visible shown in Figure 5.14.

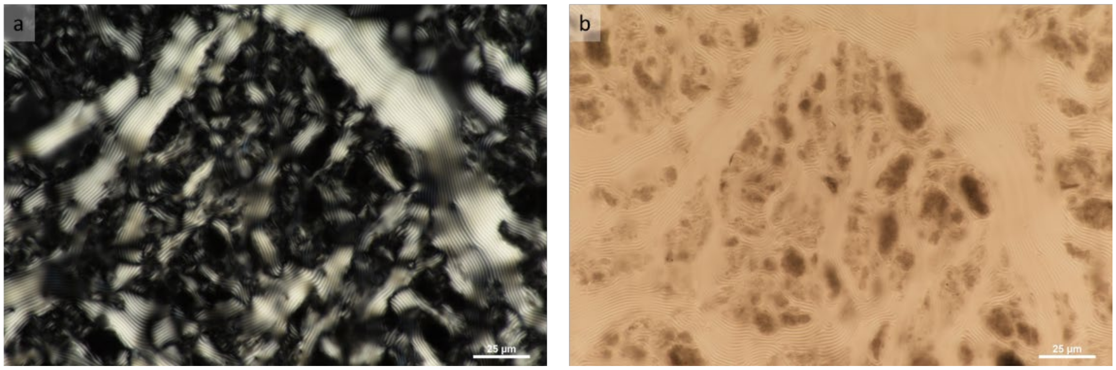

Figure 5.13: Optical microscopy images a) with and b) without crosspolarization of a flocculated biphasic dsDNA-SWNT dispersion imaged with a 60x objective.

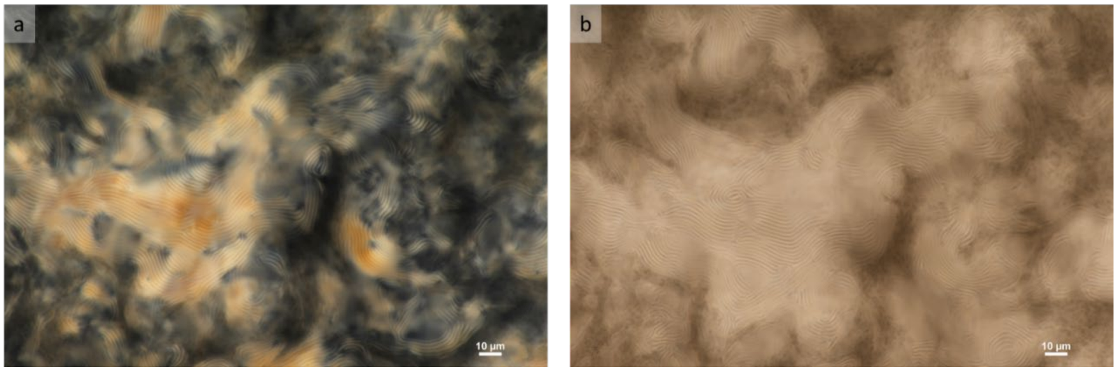

Figure 5.14: Optical microscopy images a) with and b) without crosspolarization of a highly anisotropic biphasic dsDNA-SWNT dispersion imaged with a 60x objective.

When allowed to dry completely, the concentrated supernatant samples can be resuspended in DI water by simple mixing and concentrated to form a nematic phase, as shown in Figure 5.15. Since the dsDNA is bound tightly to the SWNT, they redisperse relatively easily in water. However, there is a significant change in the microstructure. This could be due to some slight aggregation at high concentration forming bundles of SWNT. Then, when resuspended, the dispersion experiences the same behavior as the uncentrifuged mixture, forming a nematic at high concentration.

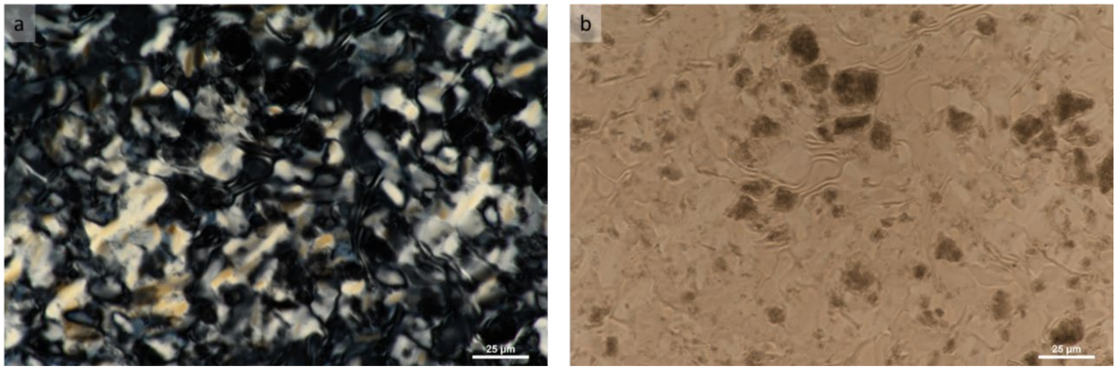

Figure 5.15: Optical microscopy images a) with and b) without crosspolarization of a nematic dsDNA-SWNT dispersion imaged with a 60x objective.

It is clear from this investigation of dsDNA-SWNT that SWNT type and purity plays an important role in the interaction and stability of dsDNA-SWNT dispersions. The sonication conditions were also found to play a role in dsDNA-SWNT dispersion. The balance of the temperature low enough to keep the dsDNA from completely disassociating to ssDNA, while providing enough energy to encourage partial disassociation (fraying) during the sonication process is key to providing frayed dsDNA for SWNT interaction.

5.4 Experimental and Computational Modeling Studies of CNC Self-Assembly in Dispersions and Films

The goal of this research was to provide a computational modeling framework for the relaxation dynamics of CNC dispersions after shear cessation which would be supported by experimental work. This work was a collaborative effort between the Davis research group at Auburn University (experimental work) and the Dr. Micah Green and former graduate student Dr. Martin Pospisil at Texas A&M University (computational modeling). Recent research on CNC films have reported robust mechanical properties as well as unique thermal properties and desirable photonic properties with optical sensing applications.[85, 90, 164-167] In these experiments, the CNC were shear aligned with a Linkam optical rheology system CSS450, a parallel plate shear cell, assembled with the Nikon microscope, shown in Figure 5.16, to obtain time-lapse micrographs after shear cessation. Dispersions were sheared at room temperature with a shear rate of 100 s^{-1} for 5 min to completely shear align rods in the flow direction. The automated time lapse consisted of taking images every 10 s for 15 min, then every 30 s for 45 min to 1.5 h.

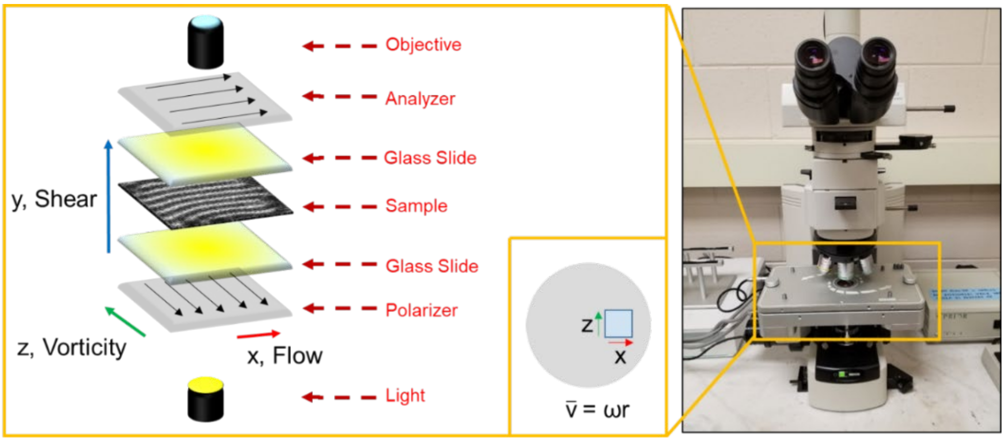

Figure 5.16: An image and schematic of the experimental setup for post-shear relaxation experiments.[104]

To compare with experiments, a finite element analysis was conducted using COMSOL Multiphysics which captured relaxation dynamics of mesogens from a shear aligned initial state. The 3D model allowed chiral microstructures to develop uninhibited throughout the entire system, in contrast to previous models that were simplified to two dimensions and restricted complex helical formations.[168] Visualization of the model was achieved using ellipsoid maps and/or simulated micrographs, shown in Figure 5.17. These ellipsoid maps, that represent local orientation of the mesogen. For each ellipsoid, the major axis is scaled by the largest eigenvalue of second order traceless tensor **Q** and lies in the direction of the corresponding eigenvector which represents the molecular director. For simulated micrographs, a similar eigenvalue–eigenvector analysis is performed on each **Q** tensor to obtain molecular directors. These directors were then used in a Jones Matrix formalism proposed by Ondris-Crawford et al. to create the simulated micrographs.[169]

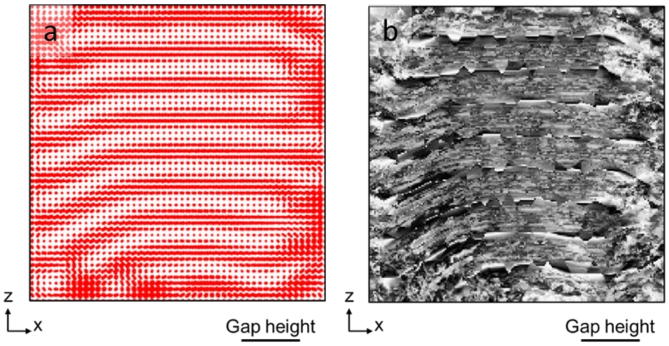

Figure 5.17: An ellipsoid map and a simulated micrograph generated from the model solution.[104]

Experimental data was vital to the development of the model to ensure that the model was accurately capturing the physical system. The model parameters are dimensionless and thus the dimensions of the system are scaled to a dimensionless gap height parameter. This work was intended to also capture the effects gap height variation had on CNC systems. However, after many experiments, it was decided that the limitations of optical microscopy prevent the capture of complex 3D structures with enough detail to properly model the behavior. At smaller gap heights, the behavior is well modeled, correctly modeling homeotropic helix orientation, shown in Figure 5.18.

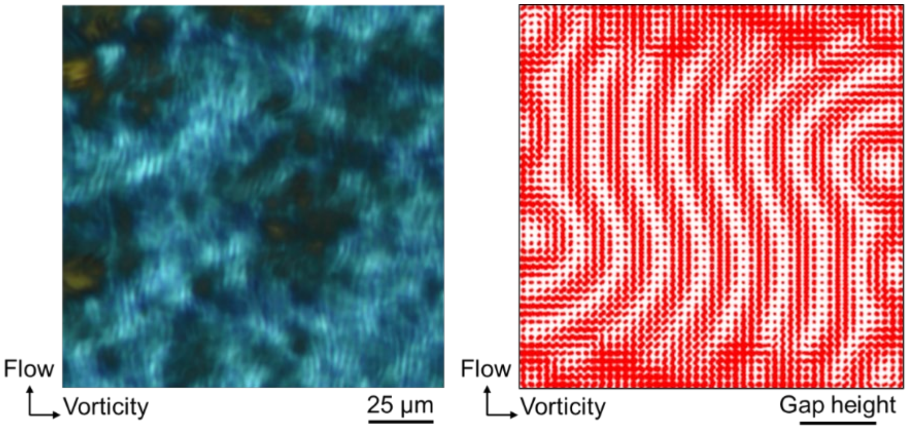

Figure 5.18: A comparison between experiment micrograph a 5.14 vol % CNC dispersion with a shear cell gap of 50 µm (left) and simulated ellipsoid map (right).[104]

In the shear cell experiment, the dispersion initially exhibited uniform birefringence as shown in Figure 5.19 (0 min). The appearance of a banded texture began at 10 min and was fully developed by 20–25 min after the cessation of shear. Here, light areas represent rod alignment in the flow direction and dark areas represent rod alignment ±45° from the flow direction. A similar texture was seen in hydroxypropyl cellulose and poly(-γ-benzylglutamate) dispersions prepared by Vermant et al.[170] This banded texture was thought to be dependent on shear rate, but our results show that mesogen alignment occurs and band formation follows upon relaxation even at sufficiently high shear rates. Experiments conducted by Lonberg et al. also verified the banded texture to be independent of shear in nematic systems.[171] Those experiments utilized a magnetic field, rather than mechanical shear, to induce rod alignment and observed a similar band formation even after its removal. In this work, the banded texture further relaxed and led to a homeotropic cholesteric texture 75 min after cessation of shear, demonstrating that the cholesteric texture can be recovered, given adequate relaxation time, even after high shear.

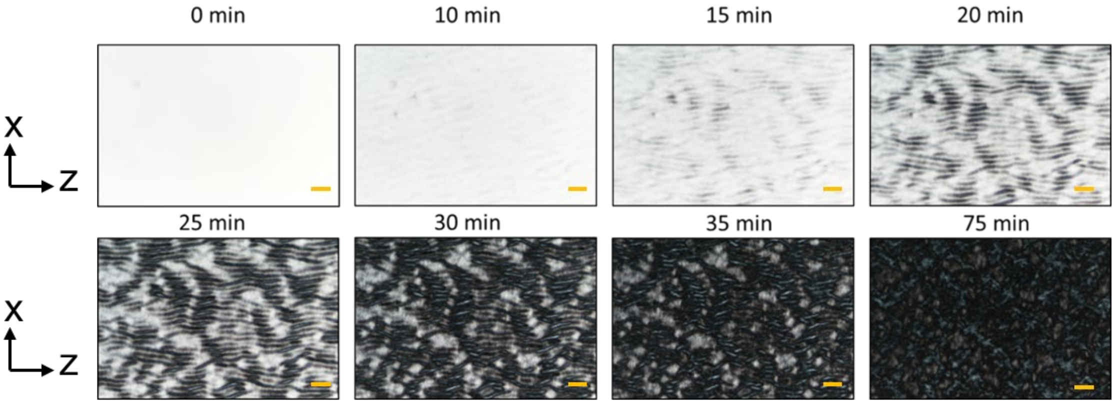

Figure 5.19: A 5.14 vol % CNC dispersion after cessation of 100 s^{-1} shear with a 50 μm gap height. Scale bar is 50 μm.[104]

The simulations started from an aligned state and allowed short- and long-range elastic effects as well as chiral forces to influence the structure formed upon relaxation. The results from the simulation are shown in Figure 5.20. Note that the axes for the flow, x, and vorticity, z, directions are reversed from experiments. The model also develops a banded texture, around $\hat{t}$ = 150. However, the banded texture runs parallel to the flow direction in the simulation rather than perpendicular, contrary to experimental results from this research and others.[170-171] Therefore, these bands from the simulation do not represent the same bands seen in experiments but rather the beginnings of helical alignment. The banded texture during relaxation seen in the experiment from the 15 to 30 min time points is not captured by the model. The model further develops into a cholesteric fingerprint texture at the end of the simulation $\hat{t}$ = 300 which agrees well with the experiments. The model was developed thus far to predict the final structure of anisotropic dispersions of CNC. Though it does not capture the intermediate banded texture, this model successfully predicts the relaxation and final structure of the dispersion which are most important to create films with controlled microstructure.

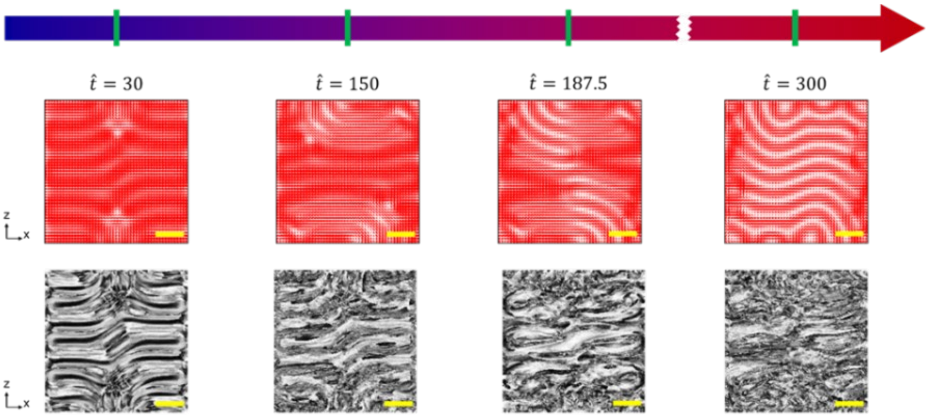

Figure 5.20: Ellipsoid maps and simulated micrographs showing banding patterns and fingerprint texture of solution at values of dimensionless time, $\hat{t}$.[104]

The modeling work was further extended to capture the behavior of drying films, which adds concentration variation with time to the model. There are many issues with producing films, caused by microstructural defect formation in the fluid phase processing of these films which has been associated with incomplete fusion of chiral domains, complex vitrification, and complicated electrostatic interactions between mesogens. To address the issues affecting film production, many parameters in the processing of thin films have been studied. Recent experimental studies have been undertaken to increase the uniformity and size the planar microstructural domains. Park et al. studied the effects of orbital shear and initial CNC concentration.[172] They concluded that anisotropic domains elongated which induced planar helical orientations to reduce the interfacial energy in the direction of the shortest axis of the resultant ellipsoid and that fully liquid crystalline dispersions generated the most uniform planar orientations.[172] Slow drying the dispersions of CNC by significantly raising the humidity of the drying environment has also been shown to generate more uniform film colors than dried under ambient conditions.[46, 173-174] In an effort to study both effects simultaneously, Saha et al. found that a combination of the orbital shear techniques of Park et al. and the use of a humidity controlled environment created the most uniform planar microstructural domains.[46]

Extension of the model included the introduction of a biphasic dispersion with threshold concentrations for isotropic and anisotropic domains and addition of a dimensionless concentration profile which was controlled based upon the concentration of the dispersion and the effective Sherwood number, given by:

$$Sh_{eff} = Sh_{ref}\frac{(1-\Phi_{min})}{(1-\Phi_{max})}, \tag{5.5}$$

where ϕ_{max} and ϕ_{min} represent the maximum and minimum values of the relative humidity used in the experiment, respectively. The Sherwood number represents the ratio of convective to diffusive mass transport. A reference Sherwood number, Sh_{ref}, was calculated using the convective mass transfer coefficient presented by Iskra et al. at a particular relative humidity.[175] The minimum value of the relative humidity is taken to be the relative humidity of an air conditioned room (~ 40%). The maximum value of relative humidity was measured in the humidified drying environment at 98%. The films were made by placing approximately 200 µL of CNC dispersion on a clean glass slide and covered with a coverslip, presheared for 5 minutes under orbital shear then dried in a closed petri dish at 98% humidity on an orbital mixer at 60 rpm.

Experiments performed were aimed at investigating surface anchoring and effects of initial shear alignment. Films were made with coverslip (double surface anchoring) and without coverslip (single surface anchoring). Since the micrographs of these dispersions were taken from above the film in reflected light mode, the microstructure of the top surface is the most visible feature. The microstructure of top surface is affected greatly by surface anchoring, evidenced by the great differences in their film texture in Figure 5.21b and d. The simulations model the final film textures well in the coverslip case, Figure 5.21a. However, in the no-coverslip case, some planar alignment can be seen in the model, Figure 5.21c. This is attributed to the bottom glass slide where nucleation occurred and promoted planar orientation and, due to the drying front, begin to tilt inward towards the edges, which are actually seen in the enlarged image, Figure 5.21e.

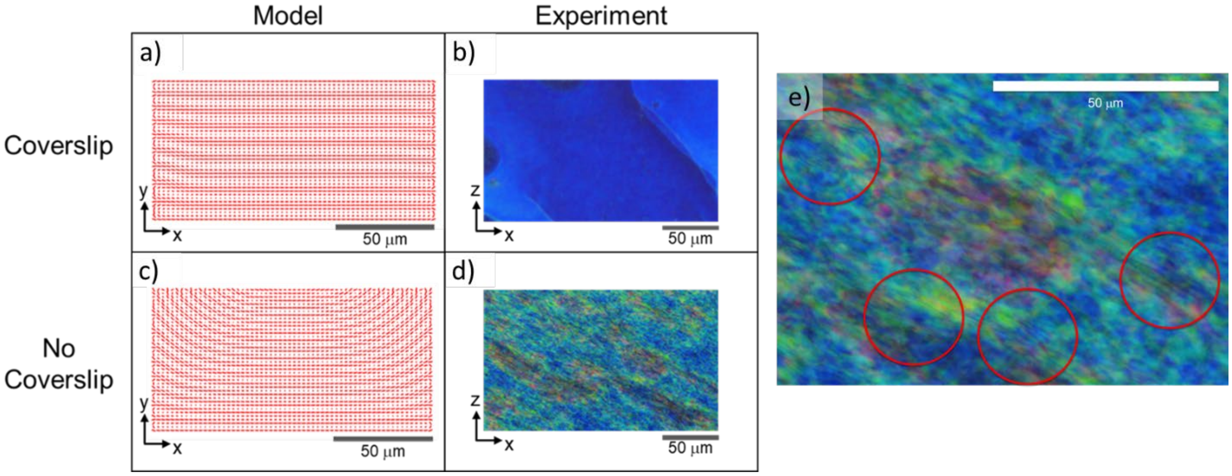

Figure 5.21: (a&c): Ellipsoid maps depicting helical microstructures of gelated films with and without a coverslip. (b&d): Reflective microscopy of films generated from an initially biphasic dispersion with and without a coverslip. (e): Enlarged image of (d). $Sh_{eff} = 3$ in both the experiments and the simulations.[176]

Initial shear alignment was modeled with a fully liquid crystalline sample so that there was certainty of complete alignment in the flow direction. The dispersion used was biphasic and was sheared onto the glass slide with a Gardco doctor blade coater, at a shear rate of approximately 1000 s^{-1} to ensure alignment and dried in a humid environment with no orbital shear. The experiment resulted in a film with a non-uniform planar texture with only very small regions of uniform color and texture. Comparison to the model showed evidence of kinetic arrest in the experiment before mesogen reorientation. Even at low Sh_{eff}, the model only showed planar orientation at the edges of the system before reaching a kinetically arrested state. Increasing the Sh_{eff} only exacerbated this effect with Sh_{eff} =300 showing complete alignment remained at the edges before mesogen reorientation could occur.

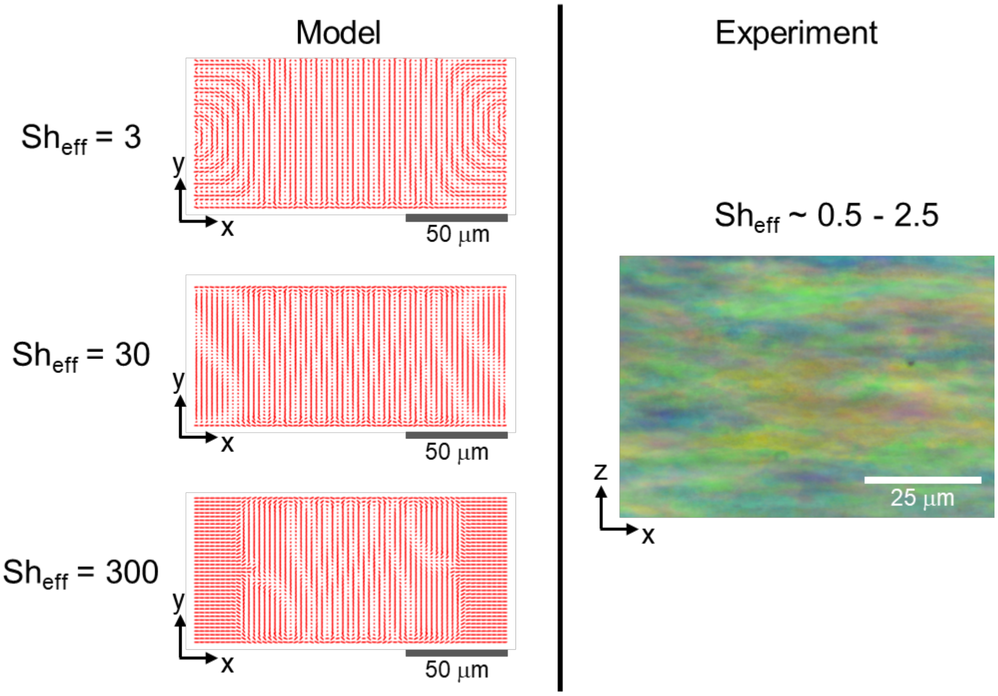

Figure 5.22: The final microstructure of an initially shear-aligned liquid crystalline dispersion and its corresponding simulation produced using double surface anchoring (coverslip) are depicted at various drying speeds.[176]

In the no-coverslip case, the experiment showed some fingerprint texture. At slow drying rates (Sh_{eff} = 3) helical microstructures appear to be uniform but tilted, similar to the no-coverslip case of Figure 5.21. Experimentally this would manifest as a fingerprint-like texture which is potentially the behavior demonstrated in Figure 5.23. As drying rate increases, a competition arises between helical reorientation and kinetic limitations and the uniformity of the system is decreased. At the fastest drying many mesogens remain flow aligned as they were unable to reorient before the onset of kinetic arrest. While the models in Figure 5.22 and Figure 5.23 start from a liquid crystalline concentration, it appears that initial mesogens alignment has a significant impact on the total amount of time needed for reorientation of the chiral microstructure.

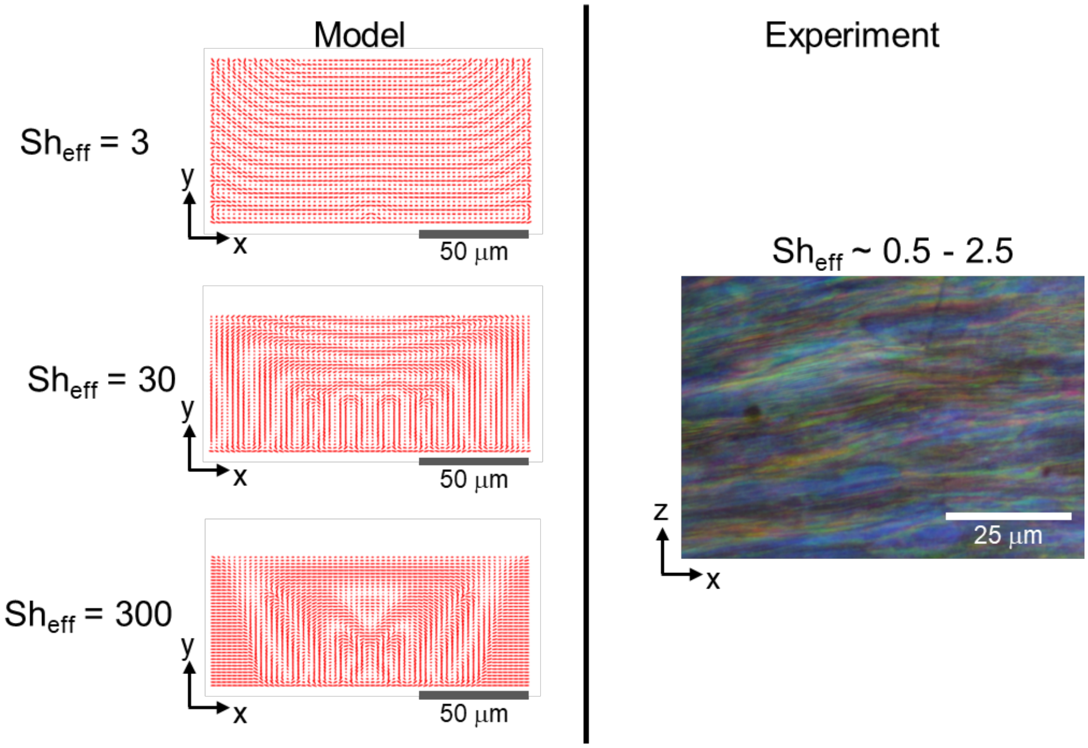

Figure 5.23: The final microstructure of an initially shear-aligned liquid crystalline dispersion and its corresponding simulation produced using single surface anchoring (no coverslip) are depicted at various drying speeds.[176]

5.5 Conclusions

Understanding LC self-assembly, alignment and orientation is vital to driving and realizing the numerous emerging applications of these extraordinary systems. In this research, it has been shown that the orientation dynamics of CNC under flow can be appropriately measured by rheoSANS. RheoSANS gives more insight and better measure of into the origins of three-region rheological behavior in LC systems in systems where this behavior is not detectable by rheology alone. Computational modeling of the experimentally observed behavior of CNC dispersions and films has given a more in-depth understanding of cholesteric helix orientation after shear cessation and during film drying, and help to explain seemingly anomalous experimental results.

Chapter 6: Conclusions

This dissertation makes key contributions to understanding interactions in anisotropic nanomaterial dispersions. Specifically, it presents the results of research in two main areas (1) the interactions of single-walled carbon nanotube (SWNT) dispersions with biomolecules and bacteriological systems, and (2) cholesteric liquid crystal flow and relaxation dynamics. The first area involved comparing covalent and noncovalent attachment of LSZ-SWNT on antibacterial activity and on film antibacterial performance and strength. These results showed that covalent functionalization affects initial rate of antibacterial activity and that robust films can be made from SWNT-LSZ dispersions. The next thrust was collaborative with microbiologists and directly challenged the controversial results in the literature. This involved the development of antibacterial protocols, dispersion procedures, and sterility measures to ensure test results were accurate and reliable. The key contribution from this research was that despite much controversy in the literature, the overall antibacterial activity is not affected appreciably by the addition of SWNT, but rather SWNT have some synergistic effects with environments under which the cell wall of a Gram-positive bacterium is stressed.

In the second area of this research, flow and relaxation dynamics of cholesteric liquid crystal dispersions were investigated with rheoSANS. CNC dispersions were studied using rheological, rheo-small-angle neutron scattering (rheoSANS) and rheo-optical methods. The orientation dynamics of CNC under flow can be appropriately measured by rheoSANS. The key contribution in this work was that RheoSANS gives more insight and a better measure of into the origins of three-region rheological behavior in biphasic CNC systems in systems where this behavior is not rheologically detectable.

A collaborative effort comprised of computational modeling and a series of rheological and rheo-optical experiments yielded a Landau-de Gennes formulation in a 3-D dynamic finite element simulation in which ellipsoid maps were created to predict alignment and helix orientation as a function of gap height and chiral strength during post-shear relaxation. This model was extended to include mass transfer and predict the orientation of CNC during film drying. This is especially useful for fabrication of controlled optical property films. The key contribution from this collaborative research was that rigorous experimentation verified and drove the model development for validity and accuracy to the physical systems.

The results of this dissertation provide an understanding of the interactions in anisotropic nanomaterial dispersions with biomolecules, biological systems, and with themselves. The antibacterial properties of SWNT were thoroughly investigated, providing significant and controversial insight that only under some underlying environmental cell stress conditions were synergistic antibacterial effects of SWNT observed. The results of self-assembly of CNC dispersions studied during flow, relaxation and drying ultimately provide a foundation for creating films with controlled microstructure and thus optical properties. A model was then developed guided by extensive experimentation to predict the final structure of a dried film under a variety of surface anchoring and initial alignment states. Together, these efforts highlight the value of using multiple approaches to understand complex nanomaterial dispersions.

Chapter 7: References

1. Willyard, C., The Drug-Resistant Bacteria That Pose the Greatest Health Threats. *Nature News* **2017,** *543* (7643), 15.

2. Iijima, S., Helical Microtubules of Graphitic Carbon. *Nature* **1991,** *354* (6348), 56-58.

3. Bethune, D.; Klang, C.; De Vries, M.; Gorman, G.; Savoy, R.; Vazquez, J.; Beyers, R., Cobalt-Catalysed Growth of Carbon Nanotubes with Single-Atomic-Layer Walls. **1993**.

4. Guanghua, G.; Tahir, Ç.; William, A. G., III, Energetics, Structure, Mechanical and Vibrational Properties of Single-Walled Carbon Nanotubes. *Nanotechnology* **1998,** *9* (3), 184.

5. Krishnan, A.; Dujardin, E.; Ebbesen, T. W.; Yianilos, P. N.; Treacy, M. M. J., Young's Modulus of Single-Walled Nanotubes. *Physical Review B* **1998,** *58* (20), 14013-14019.

6. Yu, M.-F.; Files, B. S.; Arepalli, S.; Ruoff, R. S., Tensile Loading of Ropes of Single Wall Carbon Nanotubes and Their Mechanical Properties. *Physical Review Letters* **2000,** *84* (24), 5552-5555.

7. Walters, D. A.; Ericson, L. M.; Casavant, M. J.; Liu, J.; Colbert, D. T.; Smith, K. A.; Smalley, R. E., Elastic Strain of Freely Suspended Single-Wall Carbon Nanotube Ropes. *Applied Physics Letters* **1999,** *74* (25), 3803-3805.

8. Baughman, R. H.; Zakhidov, A. A.; de Heer, W. A., Carbon Nanotubes--the Route toward Applications. *Science* **2002,** *297* (5582), 787-792.

9. Hone, J.; Whitney, M.; Piskoti, C.; Zettl, A., Thermal Conductivity of Single-Walled Carbon Nanotubes. *Physical Review B* **1999,** *59* (4), R2514-R2516.

10. Collins, P. G.; Avouris, P., Nanotubes for Electronics. *Scientific American* **2000,** *283* (6), 62.

11. Dyke, C. A.; Tour, J. M., Covalent Functionalization of Single-Walled Carbon Nanotubes for Materials Applications. *The Journal of Physical Chemistry A* **2004,** *108* (51), 11151-11159.

12. Dresselhaus, M. S.; Dresselhaus, G.; Eklund, P. C., *Science of Fullerenes and Carbon Nanotubes: Their Properties and Applications*. Academic Press: 1996.

13. Dresselhaus, M. S.; Jorio, A.; Saito, R., Characterizing Graphene, Graphite, and Carbon Nanotubes by Raman Spectroscopy. *Annual Review of Condensed Matter Physics* **2010,** *1* (1), 89-108.

14. Frank, S.; Poncharal, P.; Wang, Z. L.; Heer, W. A. d., Carbon Nanotube Quantum Resistors. *Science* **1998,** *280* (5370), 1744-1746.

15. Tang, Z. K.; Zhang, L.; Wang, N.; Zhang, X. X.; Wen, G. H.; Li, G. D.; Wang, J. N.; Chan, C. T.; Sheng, P., Superconductivity in 4 Angstrom Single-Walled Carbon Nanotubes. *Science* **2001,** *292* (5526), 2462-2465.

16. O'Connell, M. J.; Bachilo, S. M.; Huffman, C. B.; Moore, V. C.; Strano, M. S.; Haroz, E. H.; Rialon, K. L.; Boul, P. J.; Noon, W. H.; Kittrell, C.; Ma, J.; Hauge, R. H.; Weisman, R. B.; Smalley, R. E., Band Gap Fluorescence from Individual Single-Walled Carbon Nanotubes. *Science* **2002,** *297* (5581), 593-596.

17. Sun, C.-H.; Yin, L.-C.; Li, F.; Lu, G.-Q.; Cheng, H.-M., Van Der Waals Interactions between Two Parallel Infinitely Long Single-Walled Nanotubes. *Chemical Physics Letters* **2005,** *403* (4–6), 343-346.

18. Davis, V. A.; Parra-Vasquez, A. N. G.; Green, M. J.; Rai, P. K.; Behabtu, N.; Prieto, V.; Booker, R. D.; Schmidt, J.; Kesselman, E.; Zhou, W.; Fan, H.; Adams, W. W.; Hauge, R. H.; Fischer, J. E.; Cohen, Y.; Talmon, Y.; Smalley, R. E.; Pasquali, M., True Solutions of Single-Walled Carbon Nanotubes for Assembly into Macroscopic Materials. *Nat Nano* **2009,** *4* (12), 830-834.

19. Dresselhaus, M. S.; Dresselhaus, G.; Saito, R.; Jorio, A., Raman Spectroscopy of Carbon Nanotubes. *Physics Reports* **2005,** *409* (2), 47-99.

20. Saurabh, S.; Sahoo, P. K., Lysozyme: An Important Defence Molecule of Fish Innate Immune System. *Aquaculture Research* **2008,** *39* (3), 223-239.

21. Duan, J.; Park, S. I.; Daeschel, M. A.; Zhao, Y., Antimicrobial Chitosan-Lysozyme (Cl) Films and Coatings for Enhancing Microbial Safety of Mozzarella Cheese. *Journal of Food Science* **2007,** *72* (9), M355-M362.

22. Tenovuo, J., Clinical Applications of Antimicrobial Host Proteins Lactoperoxidase, Lysozyme and Lactoferrin in Xerostomia: Efficacy and Safety. *Oral Diseases* **2002,** *8* (1), 23-29.

23. Hannig, C.; Hoch, J.; Becker, K.; Hannig, M.; Attin, T., Lysozyme Activity in the Initially Formed in Situ Pellicle. *Archives of Oral Biology* **2005,** *50* (9), 821-828.

24. Sharon, N., The Chemical Structure of Lysozyme Substrates and Their Cleavage by the Enzyme. *Proceedings of the Royal Society of London. Series B, Biological Sciences* **1967,** *167* (1009), 402-415.

25. Vocadlo, D. J.; Davies, G. J.; Laine, R.; Withers, S. G., Catalysis by Hen Egg-White Lysozyme Proceeds Via a Covalent Intermediate. *Nature* **2001,** *412* (6849), 835-838.

26. Hajipour, M. J.; Fromm, K. M.; Akbar Ashkarran, A.; Jimenez de Aberasturi, D.; Larramendi, I. R. d.; Rojo, T.; Serpooshan, V.; Parak, W. J.; Mahmoudi, M., Antibacterial Properties of Nanoparticles. *Trends in Biotechnology* **2012,** *30* (10), 499-511.

27. Nepal, D.; Minus, M. L.; Kumar, S., Lysozyme Coated DNA and DNA/Swnt Fibers by Solution Spinning. *Macromolecular Bioscience* **2011,** *11* (7), 875-881.

28. Asuri, P.; Bale, S. S.; Pangule, R. C.; Shah, D. A.; Kane, R. S.; Dordick, J. S., Structure, Function, and Stability of Enzymes Covalently Attached to Single-Walled Carbon Nanotubes. *Langmuir* **2007,** *23* (24), 12318-12321.

29. da Silva, M. A.; Arêas, E. P. G., Solvent-Induced Lysozyme Gels: Rheology, Fractal Analysis, and Sol–Gel Kinetics. *Journal of Colloid and Interface Science* **2005,** *289* (2), 394-401.

30. Szymanska, A.; Hornowski, T.; Kozak, M.; Slosarek, G., The Saxs and Rheological Studies of Hewl Amyloid Formation. *Acta Physica Polonica-Series A General Physics* **2008,** *114* (2), 447.

31. Horn, D. W.; Tracy, K.; Easley, C. J.; Davis, V. A., Lysozyme Dispersed Single-Walled Carbon Nanotubes: Interaction and Activity. *The Journal of Physical Chemistry C* **2012,** *116* (18), 10341-10348.

32. Calvaresi, M.; Zerbetto, F., The Devil and Holy Water: Protein and Carbon Nanotube Hybrids. *Accounts of Chemical Research* **2013,** *46* (11), 2454-2463.

33. Matsuura, K.; Saito, T.; Okazaki, T.; Ohshima, S.; Yumura, M.; Iijima, S., Selectivity of Water-Soluble Proteins in Single-Walled Carbon Nanotube Dispersions. *Chemical Physics Letters* **2006,** *429* (4–6), 497-502.

34. Nepal, D.; Balasubramanian, S.; Simonian, A. L.; Davis, V. A., Strong Antimicrobial Coatings: Single-Walled Carbon Nanotubes Armored with Biopolymers. *Nano Letters* **2008,** *8* (7), 1896-1901.

35. Horn, D. W.; Ao, G.; Maugey, M.; Zakri, C.; Poulin, P.; Davis, V. A., Dispersion State and Fiber Toughness: Antibacterial Lysozyme-Single Walled Carbon Nanotubes. *Advanced Functional Materials* **2013**, 6082-6090

36. Nyankima, A. G.; Horn, D. W.; Davis, V. A., Free-Standing Films from Aqueous Dispersions of Lysozyme, Single-Walled Carbon Nanotubes, and Polyvinyl Alcohol. *ACS Macro Letters* **2013,** *3* (1), 77-79.

37. Borzooeian, Z.; Safavi, A.; Hossain Sheikhi, M.; Aminlari, M.; Mahdi Doroodmand, M., Preparation and Investigation on Properties of Lysozyme Chemically Bonded to Single-Walled Carbon Nanotubes. *Journal of Experimental Nanoscience* **2010,** *5* (6), 536-547.

38. Merli, D.; Ugonino, M.; Profumo, A.; Fagnoni, M.; Quartarone, E.; Mustarelli, P.; Visai, L.; Grandi, M. S.; Galinetto, P.; Canton, P., Increasing the Antibacterial Effect of Lysozyme by Immobilization on Multi-Walled Carbon Nanotubes. *Journal of Nanoscience and Nanotechnology* **2011,** *11* (4), 3100-3106.

39. Pedrosa, V. A.; Paliwal, S.; Balasubramanian, S.; Nepal, D.; Davis, V.; Wild, J.; Ramanculov, E.; Simonian, A., Enhanced Stability of Enzyme Organophosphate Hydrolase Interfaced on the Carbon Nanotubes. *Colloids and Surfaces B: Biointerfaces* **2010,** *77* (1), 69-74.

40. Feng, W.; Ji, P., Enzymes Immobilized on Carbon Nanotubes. *Biotechnology Advances* **2011,** *29* (6), 889-895.

41. Reinitzer, F., Beiträge Zur Kenntniss Des Cholesterins. *Monatshefte für Chemie/Chemical Monthly* **1888,** *9* (1), 421-441.

42. Donald, A. M.; Windle, A. H.; Hanna, S., *Liquid Crystalline Polymers*. Cambridge University Press: 2006.

43. Lagerwall, J. P. F.; Scalia, G., A New Era for Liquid Crystal Research: Applications of Liquid Crystals in Soft Matter Nano-, Bio- and Microtechnology. *Current Applied Physics* **2012,** *12* (6), 1387-1412.

44. Woltman, S. J.; Jay, G. D.; Crawford, G. P., Liquid-Crystal Materials Find a New Order in Biomedical Applications. *Nature Materials* **2007,** *6* (12), 929-938.

45. Li, J.; Wen, C.-H.; Gauza, S.; Lu, R.; Wu, S.-T., Refractive Indices of Liquid Crystals for Display Applications. *Journal of Display Technology* **2005,** *1* (1), 51.

46. Saha, P.; Davis, V. A., Photonic Properties and Applications of Cellulose Nanocrystal Films with Planar Anchoring. *ACS Applied Nano Materials* **2018,** *1* (5), 2175-2183.

47. Doi, M.; Edwards, S. F., *The Theory of Polymer Dynamics*. Oxford University Press: 1988; Vol. 73.

48. Doi, M.; Edwards, S. F., Dynamics of Concentrated Polymer Systems. Part 1.—Brownian Motion in the Equilibrium State. *Journal of the Chemical Society, Faraday Transactions 2: Molecular and Chemical Physics* **1978,** *74* (0), 1789-1801.

49. Davis, V. A.; Ericson, L. M.; Parra-Vasquez, A. N. G.; Fan, H.; Wang, Y.; Prieto, V.; Longoria, J. A.; Ramesh, S.; Saini, R. K.; Kittrell, C.; Billups, W. E.; Adams, W. W.; Hauge, R. H.; Smalley, R. E.; Pasquali, M., Phase Behavior and Rheology of Swnts in Superacids. *Macromolecules* **2004,** *37* (1), 154-160.

50. Onsager, L., The Effects of Shape on the Interaction of Colloidal Particles. *Annals of the New York Academy of Sciences* **1949,** *51* (4), 627-659.

51. Flory, P. J., Phase Equilibria in Solutions of Rod-Like Particles. *Proceedings of the Royal Society of London. Series A. Mathematical and Physical Sciences* **1956,** *234* (1196), 73-89.

52. Green, M. J.; Parra-Vasquez, A. N. G.; Behabtu, N.; Pasquali, M., Modeling the Phase Behavior of Polydisperse Rigid Rods with Attractive Interactions with Applications to Single-Walled Carbon Nanotubes in Superacids. *Journal of Chemical Physics* **2009,** *131* (8), 084901.

53. Khokhlov, A.; Semenov, A., On the Theory of Liquid-Crystalline Ordering of Polymer Chains with Limited Flexibility. *Journal of Statistical Physics* **1985,** *38* (1-2), 161-182.

54. Flory, P. J.; Ronca, G., Theory of Systems of Rodiike Particles: Ii. Thermotropic Systems with Orientation-Dependent Interactions. *Molecular Crystals and Liquid Crystals* **1979,** *54* (3-4), 311-330.

55. Hanson, E. G.; Shen, Y. R., Refractive Indices and Optical Anisotropy of Homologous Liquid Crystals. *Molecular Crystals and Liquid Crystals* **1976,** *36* (3-4), 193-207.

56. Wu, S.-T.; Efron, U.; Hess, L. D., Birefringence Measurements of Liquid Crystals. *Applied Optics* **1984,** *23* (21), 3911-3915.

57. Ciferri, A., *Liquid Crystallinity in Polymers*. VCH Publishers: New York, 1991.

58. Davis, V. A.; Ericson, L. M.; Parra-Vasquez, A. N.; Fan, H.; Wang, Y.; Prieto, V.; Longoria, J. A.; Ramesh, S.; Saini, R.; Kittrell, C.; Billups, W. E.; Adams, W. W.; Hauge, R. H.; Smalley, R. E.; Pasquali, M., Phase Behavior and Rheology of Swnts in Superacids. *Macromolecules* **2004,** *37* (1), 154-160.

59. Kiss, G., Rheology and Rheo-Optics of Concentrated Solutions of Helical Polypeptides. **1979**.

60. Haywood, A. D.; Weigandt, K. M.; Saha, P.; Noor, M.; Green, M. J.; Davis, V. A., New Insights into the Flow and Microstructural Relaxation Behavior of Biphasic Cellulose Nanocrystal Dispersions from Rheo-Sans. *Soft Matter* **2017,** *13* (45), 8451-8462.

61. Ureña-Benavides, E. E.; Ao, G.; Davis, V. A.; Kitchens, C. L., Rheology and Phase Behavior of Lyotropic Cellulose Nanocrystal Suspensions. *Macromolecules* **2011,** *44* (22), 8990-8998.

62. Aharoni, S. M., Rigid Backbone Polymers, Xvii: Solution Viscosity of Polydisperse Systems. *Polymer* **1980,** *21* (12), 1413-1422.

63. Onogi, S.; Asada, T. In *Rheology and Rheo-Optics of Polymer Liquid Crystals*, Proceedings of the Eighth International Congress on Rheology, Naples, Italy, Astarita, G.; Marrucci, G.; Nicolais, L., Eds. Plenum Press: Naples, Italy, 1980; pp 126-136.

64. Wissbrun, K. F., Rheology of Rod-Like Polymers in the Liquid-Crystalline State. *Journal of Rheology* **1981,** *25* (6), 619-662.

65. Horn, R. G.; Kleman, M. In *Observations on Shear-Induced Textures and Rheology of a Smectic-a Phase*, Annales de Physique, EDP Sciences: 1978; pp 229-234.

66. Kulichikhin, V.; Platonov, V.; Braverman, L.; Belousova, T.; Polyakov, V.; Shablygin, M.; Volokhina, A.; Malkin, A. Y.; Papkov, S., Orientational Structure Formation in Lyotropic, Liquid Crystals of Poly-P-Benzamide. *Polymer Science USSR* **1976,** *18* (12), 3031-3043.

67. Cogswell, F. N., On the Formation of a Low Viscosity State in Stiff Chain Polymers. *British Polymer Journal* **1980,** *12* (4), 170-173.

68. Mewis, J.; Mortier, M.; Vermant, J.; Moldenaers, P., Experimental Evidence for the Existence of a Wagging Regime in Polymeric Liquid Crystals. *Macromolecules* **1997,** *30* (5), 1323-1328.

69. Quijada-Garrido, I.; Siebert, H.; Becker, P.; Friedrich, C.; Schmidt, C., Transient Rheological Behavior of Tumbling Side-Chain Liquid Crystal Polymers and Determination of Their Λ Parameters. *Rheologica Acta* **1999,** *38* (6), 495-502.

70. Romo-Uribe, A.; Windle, A. H., "Log-Rolling" Alignment in Main-Chain Thermotropic Liquid Crystalline Polymer Melts under Shear: An in-Situ WAXS Study. *Macromolecules* **1996,** *29* (19), 6246-6255.

71. Echeverria, C.; Almeida, P. L.; Aguilar Gutierrez, O. F.; Rey, A. D.; Godinho, M. H., Two Negative Minima of the First Normal Stress Difference in a Cellulose-Based Cholesteric Liquid Crystal: Helix Uncoiling. *Journal of Polymer Science Part B: Polymer Physics* **2017,** *55* (10), 821-830.

72. Ao, G. Liquid Crystalline Phase Behavior and Fiber Spinning of Double-Stranded DNA Stabilized Single-Walled Carbon Nanotube Dispersions. Auburn University, Auburn 2012.

73. Grizzuti, N.; Cavella, S.; Cicarelli, P., Transient and Steady-State Rheology of a Liquid-Crystalline Hydroxypropylcellulose Solution. *Journal of Rheology* **1990,** *34* (8), 1293-1310.

74. Marrucci, G., Rheology of Nematic Polymers. In *Liquid Crystallinity in Polymers*, Ciferri, A., Ed. VCH Publishers: New York, 1991; pp 395-421.

75. Cox, W. P.; Merz, E. H., Correlation of Dynamic and Steady Flow Viscosities. *Journal of Polymer Science* **1958,** *28* (118), 619-622.

76. Marrucci, G., Dynamics of Entanglements: A Nonlinear Model Consistent with the Cox-Merz Rule. *Journal of Non-Newtonian Fluid Mechanics* **1996,** *62* (2-3), 279-289.

77. Van Oss, C. J.; Smeenk, K. J. T.; Aarden, L. A., Inhibition of Association vs. Dissociation of High-Avidity DNA/Anti-DNA Conplexes: Possible Involvement of Secondary Hydrogen Bonds. *Immunological Investigations* **1985,** *14* (3), 245-253.

78. Leforestier, A.; Livolant, F., Supramolecular Ordering of DNA in the Cholesteric Liquid Crystalline Phase: An Ultrastructural Study. *Biophysical Journal* **1993,** *65* (1), 56-72.

79. Stanley, C. B.; Hong, H.; Strey, H. H., DNA Cholesteric Pitch as a Function of Density and Ionic Strength. *Biophysical Journal* **2005,** *89* (4), 2552-2557.

80. Moon, R. J.; Martini, A.; Nairn, J.; Simonsen, J.; Youngblood, J., Cellulose Nanomaterials Review: Structure, Properties and Nanocomposites. *Chemical Society Reviews* **2011,** *40* (7), 3941-3994.

81. Kontturi, E.; Tammelin, T.; Österberg, M., Cellulose—Model Films and the Fundamental Approach. *Chemical Society Reviews* **2006,** *35* (12), 1287-1304.

82. Klemm, D.; Heublein, B.; Fink, H.-P.; Bohn, A., Cellulose: Fascinating Biopolymer and Sustainable Raw Material. *Angewandte Chemie International Edition* **2005,** *44* (22), 3358-3393.

83. Rånby, B. G., Fibrous Macromolecular Systems. Cellulose and Muscle. The Colloidal Properties of Cellulose Micelles. *Discussions of the Faraday Society* **1951,** *11*, 158-164.

84. Nishiyama, Y.; Johnson, G. P.; French, A. D.; Forsyth, V. T.; Langan, P., Neutron Crystallography, Molecular Dynamics, and Quantum Mechanics Studies of the Nature of Hydrogen Bonding in Cellulose Iβ. *Biomacromolecules* **2008,** *9* (11), 3133-3140.

85. Habibi, Y.; Lucia, L. A.; Rojas, O. J., Cellulose Nanocrystals: Chemistry, Self-Assembly, and Applications. *Chemical Reviews* **2010,** *110* (6), 3479-3500.

86. Wang, B.; Sain, M., Isolation of Nanofibers from Soybean Source and Their Reinforcing Capability on Synthetic Polymers. *Composites Science and Technology* **2007,** *67* (11), 2521-2527.

87. Filson, P. B.; Dawson-Andoh, B. E., Sono-Chemical Preparation of Cellulose Nanocrystals from Lignocellulose Derived Materials. *Bioresource Technology* **2009,** *100* (7), 2259-2264.

88. Braun, B.; Dorgan, J. R., Single-Step Method for the Isolation and Surface Functionalization of Cellulosic Nanowhiskers. *Biomacromolecules* **2009,** *10* (2), 334-341.

89. Dong, X. M.; Kimura, T.; Revol, J. F.; Gray, D. G., Effects of Ionic Strength on the Isotropic-Chiral Nematic Phase Transition of Suspensions of Cellulose Crystallites. *Langmuir* **1996,** *12* (8), 2076-2082.

90. Revol, J.-F.; Bradford, H.; Giasson, J.; Marchessault, R.; Gray, D., Helicoidal Self-Ordering of Cellulose Microfibrils in Aqueous Suspension. *International Journal of Biological Macromolecules* **1992,** *14* (3), 170-172.

91. de Nooy, A. E. J.; Besemer, A. C.; van Bekkum, H., Highly Selective Tempo Mediated Oxidation of Primary Alcohol Groups in Polysaccharides. *Recueil des Travaux Chimiques des Pays-Bas* **1994,** *113* (3), 165-166.

92. Isogai, A.; Saito, T.; Fukuzumi, H., Tempo-Oxidized Cellulose Nanofibers. *Nanoscale* **2011,** *3* (1), 71-85.

93. Jiang, M.; McMillan, M. F.; Davis, V.; Kitchens, C. L., Phase Behavior of Acetylated Cellulose Nanocrystals and Origins of the Cross-Hatch Birefringent Texture. *Biomacromolecules* **2018,** *19* (8), 3435-3444.

94. Sadeghifar, H.; Filpponen, I.; Clarke, S. P.; Brougham, D. F.; Argyropoulos, D. S., Production of Cellulose Nanocrystals Using Hydrobromic Acid and Click Reactions on Their Surface. *Journal of Materials Science* **2011,** *46* (22), 7344-7355.

95. National Strategy for Combating Antibiotic-Resistant Bacteria. The White House, Office of the Press Secretary: 2014.

96. Goussé, C.; Chanzy, H.; Excoffier, G.; Soubeyrand, L.; Fleury, E., Stable Suspensions of Partially Silylated Cellulose Whiskers Dispersed in Organic Solvents. *Polymer* **2002,** *43* (9), 2645-2651.

97. Pei, A.; Zhou, Q.; Berglund, L. A., Functionalized Cellulose Nanocrystals as Biobased Nucleation Agents in Poly (L-Lactide)(PLLA)–Crystallization and Mechanical Property Effects. *Composites Science and Technology* **2010,** *70* (5), 815-821.

98. Saini, S.; Belgacem, M. N.; Salon, M.-C. B.; Bras, J., Non Leaching Biomimetic Antimicrobial Surfaces Via Surface Functionalisation of Cellulose Nanofibers with Aminosilane. *Cellulose* **2016,** *23* (1), 795-810.

99. Kargarzadeh, H.; Mariano, M.; Gopakumar, D.; Ahmad, I.; Thomas, S.; Dufresne, A.; Huang, J.; Lin, N., Advances in Cellulose Nanomaterials. *Cellulose* **2018,** *25* (4), 2151-2189.

100. Araki, J.; Wada, M.; Kuga, S.; Okano, T., Birefringent Glassy Phase of a Cellulose Microcrystal Suspension. *Langmuir* **2000,** *16* (6), 2413-2415.

101. Habibi, Y.; Chanzy, H.; Vignon, M. R., Tempo-Mediated Surface Oxidation of Cellulose Whiskers. *Cellulose* **2006,** *13* (6), 679-687.

102. Araki, J.; Kuga, S., Effect of Trace Electrolyte on Liquid Crystal Type of Cellulose Microcrystals. *Langmuir* **2001,** *17* (15), 4493-4496.

103. Orts, W. J.; Godbout, L.; Marchessault, R. H.; Revol, J. F., Enhanced Ordering of Liquid Crystalline Suspensions of Cellulose Microfibrils: A Small Angle Neutron Scattering Study. *Macromolecules* **1998,** *31* (17), 5717-5725.

104. Pospisil, M. J.; Saha, P.; Abdulquddos, S.; Noor, M. M.; Davis, V. A.; Green, M. J., Orientation Relaxation Dynamics in Cellulose Nanocrystal Dispersions in the Chiral Liquid Crystalline Phase. *Langmuir* **2018**.

105. Honorato-Rios, C.; Lehr, C.; Schütz, C.; Sanctuary, R.; Osipov, M. A.; Baller, J.; Lagerwall, J. P. F., Fractionation of Cellulose Nanocrystals: Enhancing Liquid Crystal Ordering without Promoting Gelation. *NPG Asia Materials* **2018,** *10* (5), 455-465.

106. Marambio-Jones, C.; Hoek, E. M. V., A Review of the Antibacterial Effects of Silver Nanomaterials and Potential Implications for Human Health and the Environment. *Journal of Nanoparticle Research* **2010,** *12* (5), 1531-1551.

107. McKenna, M., How We'll Tackle Diseases That Are Becoming Untreatable. *National Geographic* 09/22/16, 2016.

108. Chen, X.; Tam, U. C.; Czlapinski, J. L.; Lee, G. S.; Rabuka, D.; Zettl, A.; Bertozzi, C. R., Interfacing Carbon Nanotubes with Living Cells. *Journal of the American Chemical Society* **2006,** *128* (19), 6292-6293.

109. Dumortier, H.; Lacotte, S.; Pastorin, G.; Marega, R.; Wu, W.; Bonifazi, D.; Briand, J.-P.; Prato, M.; Muller, S.; Bianco, A., Functionalized Carbon Nanotubes Are Non-Cytotoxic and Preserve the Functionality of Primary Immune Cells. *Nano Letters* **2006,** *6* (7), 1522-1528.

110. Wick, P.; Manser, P.; Limbach, L. K.; Dettlaff-Weglikowska, U.; Krumeich, F.; Roth, S.; Stark, W. J.; Bruinink, A., The Degree and Kind of Agglomeration Affect Carbon Nanotube Cytotoxicity. *Toxicology Letters* **2007,** *168* (2), 121-131.

111. Zhu, Y.; Li, W., Cytotoxicity of Carbon Nanotubes. *Science in China Series B: Chemistry* **2008,** *51* (11), 1021-1029.

112. Kostarelos, K.; Lacerda, L.; Pastorin, G.; Wu, W.; WieckowskiSebastien; Luangsivilay, J.; Godefroy, S.; Pantarotto, D.; Briand, J.-P.; Muller, S.; Prato, M.; Bianco, A., Cellular Uptake of Functionalized Carbon Nanotubes Is Independent of Functional Group and Cell Type. *Nature Nanotechnology* **2007,** *2* (2), 108-113.

113. Nel, A.; Xia, T.; Mädler, L.; Li, N., Toxic Potential of Materials at the Nanolevel. *Science* **2006,** *311* (5761), 622-627.

114. Kang, S.; Herzberg, M.; Rodrigues, D. F.; Elimelech, M., Antibacterial Effects of Carbon Nanotubes: Size Does Matter! *Langmuir* **2008,** *24* (13), 6409-6413.

115. Manna, S. K.; Sarkar, S.; Barr, J.; Wise, K.; Barrera, E. V.; Jejelowo, O.; Rice-Ficht, A. C.; Ramesh, G. T., Single-Walled Carbon Nanotube Induces Oxidative Stress and Activates Nuclear Transcription Factor-Kb in Human Keratinocytes. *Nano Letters* **2005,** *5* (9), 1676-1684.

116. Kang, S.; Pinault, M.; Pfefferle, L. D.; Elimelech, M., Single-Walled Carbon Nanotubes Exhibit Strong Antimicrobial Activity. *Langmuir* **2007,** *23* (17), 8670-8673.

117. Liu, S.; Wei, L.; Hao, L.; Fang, N.; Chang, M. W.; Xu, R.; Yang, Y.; Chen, Y., Sharper and Faster "Nano Darts" Kill More Bacteria: A Study of Antibacterial Activity of Individually Dispersed Pristine Single-Walled Carbon Nanotube. *ACS Nano* **2009,** *3* (12), 3891-3902.

118. Trozzi, F.; Marforio, T. D.; Bottoni, A.; Zerbetto, F.; Calvaresi, M., Engineering the Fullerene-Protein Interface by Computational Design: The Sum Is More Than Its Parts. *Israel Journal of Chemistry* **2017,** *57* (6), 547-552.

119. Vaitheeswaran, S.; Garcia, A. E., Protein Stability at a Carbon Nanotube Interface. *Journal of Chemical Physics* **2011,** *134* (12).

120. Raffaini, G.; Ganazzoli, F., Protein Adsorption on Biomaterial and Nanomaterial Surfaces: A Molecular Modeling Approach to Study Non-Covalent Interactions. *Journal of Applied Biomaterials & Biomechanics* **2010,** *8* (3), 135-145.

121. Liang, F.; Chen, B., A Review on Biomedical Applications of Single-Walled Carbon Nanotubes. *Current Medicinal Chemistry* **2010,** *17* (1), 10-24.

122. Nepal, D.; Geckeler, K. E., Proteins and Carbon Nanotubes: Close Encounter in Water. *Small* **2007,** *3* (7), 1259-1265.

123. Calvaresi, M.; Hoefinger, S.; Zerbetto, F., Probing the Structure of Lysozyme–Carbon-Nanotube Hybrids with Molecular Dynamics. *Chemistry – A European Journal* **2012,** *18* (14), 4308-4313.

124. Yang, F.; Liu, Y.; Gao, L.; Sun, J., Ph-Sensitive Highly Dispersed Reduced Graphene Oxide Solution Using Lysozyme Via an in Situ Reduction Method. *The Journal of Physical Chemistry C* **2010,** *114* (50), 22085-22091.

125. Siepi, M.; Politi, J.; Dardano, P.; Amoresano, A.; De Stefano, L.; Maria Monti, D.; Notomista, E., Modified Denatured Lysozyme Effectively Solubilizes Fullerene C60 Nanoparticles in Water. *Nanotechnology* **2017,** *28* (33), 335601.

126. Calvaresi, M.; Zerbetto, F., Baiting Proteins with C60. *ACS Nano* **2010,** *4* (4), 2283-2299.

127. Nie, H.; Wang, H.; Cao, A.; Shi, Z.; Yang, S.-T.; Yuan, Y.; Liu, Y., Diameter-Selective Dispersion of Double-Walled Carbon Nanotubes by Lysozyme. *Nanoscale* **2011,** *3* (3), 970-973.

128. Barth, A., Infrared Spectroscopy of Proteins. *Biochimica et Biophysica Acta (BBA) - Bioenergetics* **2007,** *1767* (9), 1073-1101.

129. Greenfield, N. J., Using Circular Dichroism Collected as a Function of Temperature to Determine the Thermodynamics of Protein Unfolding and Binding Interactions. *Nature Protocols* **2006,** *1* (6), 2527.

130. Aldrich, S. Enzymatic Activity of Lysozyme (Ec 3.2.1.17). http://www.sigmaaldrich.com/technical-documents/protocols/biology/enzymatic-assay-of-lysozyme.html

131. Shugar, D., The Measurement of Lysozyme Activity and the Ultra-Violet Inactivation of Lysozyme. *Biochimica et Biophysica Acta* **1952,** *8* (3), 302-9.

132. Nepal, D.; Balasubramanian, S.; Simonian, A. L.; Davis, V. A., Strong Antimicrobial Coatings: Single-Walled Carbon Nanotubes Armored with Biopolymers. *Nano Letters* **2008,** *8* (7), 1896-1901.

133. Marenduzzo, D.; Finan, K.; Cook, P. R., The Depletion Attraction: An Underappreciated Force Driving Cellular Organization. *Journal of Cell Biology* **2006,** *175* (5), 681-686.

134. Seil, J. T.; Webster, T. J., Antimicrobial Applications of Nanotechnology: Methods and Literature. *International journal of nanomedicine* **2012,** *7*, 2767-2781.

135. Moore, V. C.; Strano, M. S.; Haroz, E. H.; Hauge, R. H.; Smalley, R. E.; Schmidt, J.; Talmon, Y., Individually Suspended Single-Walled Carbon Nanotubes in Various Surfactants. *Nano Letters* **2003,** *3* (10), 1379-1382.

136. Chowdhury, I.; Duch, M. C.; Gits, C. C.; Hersam, M. C.; Walker, S. L., Impact of Synthesis Methods on the Transport of Single Walled Carbon Nanotubes in the Aquatic Environment. *Environmental Science & Technology* **2012,** *46* (21), 11752-11760.

137. Muszanska, A. K.; Busscher, H. J.; Herrmann, A.; van der Mei, H. C.; Norde, W., Pluronic–Lysozyme Conjugates as Anti-Adhesive and Antibacterial Bifunctional Polymers for Surface Coating. *Biomaterials* **2011,** *32* (26), 6333-6341.

138. Sloan, A. W.; Santana-Pereira, A. L.; Goswami, J.; Liles, M. R.; Davis, V. A., Single-Walled Carbon Nanotube Dispersion in Tryptic Soy Broth. *ACS Macro Letters* **2017,** *6* (11), 1228-1231.

139. Blazek, J.; Gilbert, E. P., Application of Small-Angle X-Ray and Neutron Scattering Techniques to the Characterisation of Starch Structure: A Review. *Carbohydrate Polymers* **2011,** *85* (2), 281-293.

140. Hammouda, B., Probing Nanoscale Structures - the Sans Toolbox. 2016. http://www.ncnr.nist.gov/staff/hammouda/the_SANS_toolbox.pdf.

141. Wagner, N.; Liberatore, M.; Nettesheim, F.; Helgeson, M.; Kalman, D.; Reichert, M.; Porcar, L.; Butler, P., Rheo-Sans. In *American Conference on Neutron Scattering*, Santa Fe, New Mexico, 2008.

142. Ebeling, T.; Paillet, M.; Borsali, R.; Diat, O.; Dufresne, A.; Cavaille, J.; Chanzy, H., Shear-Induced Orientation Phenomena in Suspensions of Cellulose Microcrystals, Revealed by Small Angle X-Ray Scattering. *Langmuir* **1999,** *15* (19), 6123-6126.

143. Grizzuti, N.; Maffettone, P. L., Quiescent and Flow-Induced Transitional Behavior of Hydroxypropylcellulose Solutions. *Journal of Chemical Physics* **2003,** *118* (11), 5195-5200.

144. Burger, C.; Hsiao, B. S.; Chu, B., Preferred Orientation in Polymer Fiber Scattering. *Journal of Macromolecular Science®, Part C: Polymer Reviews* **2010,** *50* (1), 91-111.

145. Onogi, S.; Asada, T., Rheology and Rheo-Optics of Polymer Liquid Crystals. In *Rheology*, Springer: 1980; pp 127-147.

146. Ao, G.; Nepal, D.; Aono, M.; Davis, V. A., Cholesteric and Nematic Liquid Crystalline Phase Behavior of Double-Stranded DNA Stabilized Single-Walled Carbon Nanotube Dispersions. *ACS Nano* **2011,** *5* (2), 1450-1458.

147. Cathcart, H.; Nicolosi, V.; Hughes, J. M.; Blau, W. J.; Kelly, J. M.; Quinn, S. J.; Coleman, J. N., Ordered DNA Wrapping Switches on Luminescence in Single-Walled Nanotube Dispersions. *Journal of the American Chemical Society* **2008,** *130* (38), 12734-12744.

148. Badaire, S.; Zakri, C.; Maugey, M.; Derré, A.; Barisci, J. N.; Wallace, G.; Poulin, P., Liquid Crystals of DNA-Stabilized Carbon Nanotubes. *Advanced Materials* **2005,** *17* (13), 1673-1676.

149. Zheng, M.; Jagota, A.; Semke, E. D.; Diner, B. A.; McLean, R. S.; Lustig, S. R.; Richardson, R. E.; Tassi, N. G., DNA-Assisted Dispersion and Separation of Carbon Nanotubes. *Nature Materials* **2003,** *2* (5), 338.

150. Gigliotti, B.; Sakizzie, B.; Bethune, D. S.; Shelby, R. M.; Cha, J. N., Sequence-Independent Helical Wrapping of Single-Walled Carbon Nanotubes by Long Genomic DNA. *Nano Letters* **2006,** *6* (2), 159-164.

151. Johnson, R. R.; Johnson, A. T. C.; Klein, M. L., Probing the Structure of DNA−Carbon Nanotube Hybrids with Molecular Dynamics. *Nano Letters* **2008,** *8* (1), 69-75.

152. Lustig, S. R.; Jagota, A.; Khripin, C.; Zheng, M., Theory of Structure-Based Carbon Nanotube Separations by Ion-Exchange Chromatography of DNA/CNT Hybrids. *The Journal of Physical Chemistry B* **2005,** *109* (7), 2559-2566.

153. Lu, G.; Maragakis, P.; Kaxiras, E., Carbon Nanotube Interaction with DNA. *Nano Letters* **2005,** *5* (5), 897-900.

154. Zhao; Johnson, J. K., Simulation of Adsorption of DNA on Carbon Nanotubes. *Journal of the American Chemical Society* **2007,** *129* (34), 10438-10445.

155. Fernando, A.; Mary, E. H.; Jene, A. G.; Daniel, B., Base Dependent DNA–Carbon Nanotube Interactions: Activation Enthalpies and Assembly–Disassembly Control. *Nanotechnology* **2009,** *20* (39), 395101.

156. Hughes, M. E.; Brandin, E.; Golovchenko, J. A., Optical Absorption of DNA−Carbon Nanotube Structures. *Nano Letters* **2007,** *7* (5), 1191-1194.

157. Tu, X.; Manohar, S.; Jagota, A.; Zheng, M., DNA Sequence Motifs for Structure-Specific Recognition and Separation of Carbon Nanotubes. *Nature* **2009,** *460* (7252), 250-253.

158. Chen, R. J.; Zhang, Y., Controlled Precipitation of Solubilized Carbon Nanotubes by Delamination of DNA. *The Journal of Physical Chemistry B* **2006,** *110* (1), 54-57.

159. Meng, S.; Maragakis, P.; Papaloukas, C.; Kaxiras, E., DNA Nucleoside Interaction and Identification with Carbon Nanotubes. *Nano Letters* **2007,** *7* (1), 45-50.

160. Wu, S.-J.; Schuergers, N.; Lin, K.-H.; Gillen, A. J.; Corminboeuf, C.; Boghossian, A. A., Restriction Enzyme Analysis of Double-Stranded DNA on Pristine Single-Walled Carbon Nanotubes. *ACS Applied Materials & Interfaces* **2018,** *10* (43), 37386-37395.

161. Ke, F.; Qiu, X., Nanoscale Structure and Interaction of Condensed Phases of DNA–Carbon Nanotube Hybrids. *The Journal of Physical Chemistry C* **2015,** *119* (27), 15763-15769.

162. Piyasena, P.; Mohareb, E.; McKellar, R. C., Inactivation of Microbes Using Ultrasound: A Review. *International Journal of Food Microbiology* **2003,** *87* (3), 207-216.

163. Akbari, A.; Sheath, P.; Martin, S. T.; Shinde, D. B.; Shaibani, M.; Banerjee, P. C.; Tkacz, R.; Bhattacharyya, D.; Majumder, M., Large-Area Graphene-Based Nanofiltration Membranes by Shear Alignment of Discotic Nematic Liquid Crystals of Graphene Oxide. *Nature Communications* **2016,** *7* (1), 10891.

164. Diaz, J. A.; Wu, X.; Martini, A.; Youngblood, J. P.; Moon, R. J., Thermal Expansion of Self-Organized and Shear-Oriented Cellulose Nanocrystal Films. *Biomacromolecules* **2013,** *14* (8), 2900-2908.

165. Passantino, J. M.; Haywood, A. D.; Goswami, J.; Davis, V. A., Effects of Polymer Additives and Dispersion State on the Mechanical Properties of Cellulose Nanocrystal Films. *Macromolecular Materials and Engineering* **2017**.

166. Reising, A. B.; Moon, R. J.; Youngblood, J. P., Effect of Particle Alignment on Mechanical Properties of Neat Cellulose Nanocrystal Films. *Journal of Science & Technology for Forest Products and Processes* **2012,** *2* (6), 32-41.

167. Dumanli, A. G. M.; van der Kooij, H. M.; Kamita, G.; Reisner, E.; Baumberg, J. J.; Steiner, U.; Vignolini, S., Digital Color in Cellulose Nanocrystal Films. *ACS Applied Materials & Interfaces* **2014,** *6* (15), 12302-12306.

168. Venhaus, D. G.; Conatser, K. S.; Green, M. J., Dynamics of Chiral Liquid Crystals under Applied Shear. *Liquid Crystals* **2013,** *40* (6), 846-853.

169. Ondris-Crawford, R.; Boyko, E. P.; Wagner, B. G.; Erdmann, J. H.; Žumer, S.; Doane, J. W., Microscope Textures of Nematic Droplets in Polymer Dispersed Liquid Crystals. *Journal of Applied Physics* **1991,** *69* (9), 6380-6386.

170. Vermant, J.; Moldenaers, P.; Mewis, J.; Picken, S., Band Formation Upon Cessation of Flow in Liquid-Crystalline Polymers. *Journal of Rheology* **1994,** *38* (5), 1571-1589.

171. Lonberg, F.; Fraden, S.; Hurd, A. J.; Meyer, R. E., Field-Induced Transient Periodic Structures in Nematic Liquid Crystals: The Twist-Fréedericksz Transition. *Physical Review Letters* **1984,** *52* (21), 1903.

172. Park, J. H.; Noh, J.; Schütz, C.; Salazar-Alvarez, G.; Scalia, G.; Bergström, L.; Lagerwall, J. P., Macroscopic Control of Helix Orientation in Films Dried from Cholesteric Liquid-Crystalline Cellulose Nanocrystal Suspensions. *ChemPhysChem* **2014,** *15* (7), 1477-1484.

173. Dumanli, A. G.; Kamita, G.; Landman, J.; van der Kooij, H.; Glover, B. J.; Baumberg, J. J.; Steiner, U.; Vignolini, S., Controlled, Bio-Inspired Self-Assembly of Cellulose-Based Chiral Reflectors. *Advanced Optical Materials* **2014,** *2* (7), 646-650.

174. Wilts, B. D.; Dumanli, A. G.; Middleton, R.; Vukusic, P.; Vignolini, S., Invited Article: Chiral Optics of Helicoidal Cellulose Nanocrystal Films. *APL Photonics* **2017,** *2* (4), 040801.

175. Iskra, C.; Simonson, C., Effect of Air Humidity on the Convective Mass Transfer Coefficient in a Rectangular Duct. *IEA-International Energy Agency, ECBCS-Energy Conservation in Buildings and Community Systems, Annex* **2006,** *41*.

176. Pospisil, M. J.; Noor, M. M.; Amit, S. K.; Neufield, C.; Saha, P.; Davis, V. A.; Green, M. J., Chiral Structure Formation During Casting of Cellulose Nanocrystalline Films. *Langmuir* **Submitted July 2019**.

Appendix

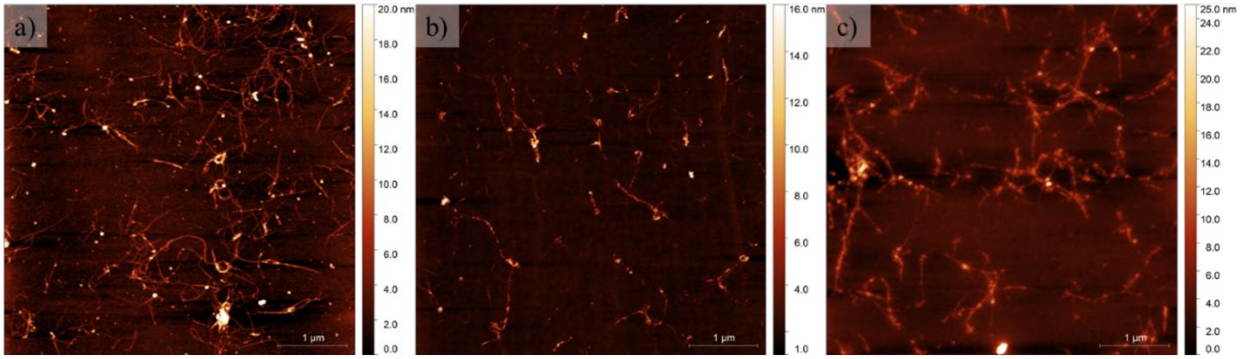

Figure A.1: AFM scans of a) LSZ-SWNT, b) Pluronic-SWNT, and c) SDS-SWNT.

Conversion from wt % to vol % for a multicomponent system

$$\phi = \frac{m_i/\rho_i}{\sum_i m_i/\rho_i} \tag{A.1}$$

Relevant densities: $\rho_{CNC} = 1.636\ g/cm^3$, $\rho_{SWNT} = 1.45\ g/cm^3$, $\rho_{dsDNA} = 1.7\ g/cm^3$.

Table A.1: CFU count data from each treatment. Treatments with the -C suffix have corrected SWNT concentration.

Organism	*Dispersant*	*Treatment*	*CFU Mean (10^6)*
S. typhimurium	SDS	SDS	8780
		SDS+SWNT	4980
		SDS+SWNT-C	7650
	Pluronic	Pluronic	4570
		Pluronic+SWNT	6500
		Pluronic+SWNT-C	8450
	Lysozyme	Lysozyme	5720
		Lysozyme+SWNT	6470
		Lysozyme+SWNT-C	9530
	DNA	DNA	5750
		DNA+SWNT	9770
		DNA+SWNT-C	8950
	TSB	TSB	7450
		TSB+SWNT	10720
		TSB+SWNT-C	8380
	Control	Antibiotic	0
		Water	3170
MRSA	SDS	SDS	0
		SDS+SWNT	0
		SDS+SWNT-C	0
	Pluronic	Pluronic	2590
		Pluronic+SWNT	660
		Pluronic+SWNT-C	1680
	Lysozyme	Lysozyme	2690
		Lysozyme+SWNT	970
		Lysozyme+SWNT-C	970
	DNA	DNA	2260
		DNA+SWNT	3300
		DNA+SWNT-C	2380
	TSB	TSB	1720
		TSB+SWNT	1180
		TSB+SWNT-C	1080
	Control	Antibiotic	1130
		Water	1070